Dielectrophoretic Manipulation of Yeast Cells Using CMOS Integrated Microfluidic

Von der Fakultät 1 - MINT - Mathematik, Informatik, Physik, Elektro- und Informationstechnik

der Brandenburgischen Technischen Universität Cottbus–Senftenberg genehmigte Dissertation zur Erlangung des akademischen Grades eines

Doktor der Ingenieurwissenschaften

(Dr. -Ing.)

vorgelegt von

Honeyeh Matbaechi Ettehad

geboren am 25.01.1986 in Mashhad

Vorsitzender: Prof. Dr. Götz Seibold
Gutachter: Prof. Dr. Christian Wenger
Gutachter: Prof. Dr. Inga Anita Fischer
Gutachter: Prof. Dr. Frank Bier

Tag der mündlichen Prüfung: 14.05.2021

Dedicated to my beloved family:

Ali, Hessam, my parents "Azita and Alireza"

and

to the spirits of my grandparents "Farangis and Gholamreza", my soulmate aunt "Fereshteh" and her newborn "Kasra" who left us unexpectedly.

Abstract

The rapid detection of infectious diseases is still an unsolved problem since their identification must be carried out either by cultivation or DNA analysis in a laboratory. The development of point-of-care (PoC) processes is a current development trend that requires further technological impulses to produce reliable and cost-effective system solutions. By miniaturizing and integrating microfluidic and electronic components, the advantages of electronic methods can be transferred to the field of PoC testing.

Microfluidics can scale down the components of analysis systems and manipulate very low volume fluids (on picoliter orders). Microfluidics offers many advantages in terms of low-cost materials, low sample consumption, high sensitivity, and quick analysis time. The benefit of such a platform broadens even further when it integrates with sensors, circuitry, and actuators to develop a so-called lab-on-a-chip (LoC) system. The microfluidic-based LoC platforms can handle complex sample analysis and diagnostic tests and can be used as a portable laboratory device that can be used at the PoC.

The emergence of the complementary metal-oxide-semiconductor (CMOS) technology and its combination with the LoC platform allowed the development of fully functional sample-to-result LoC setups, which served the portability of the device even out of the laboratory or hospitals. CMOS-based LoC device can control and manage the data from sensors, microfluidics, and actuators. Dielectrophoresis (DEP) is a non-destructive and non-invasive method promising to be used in PoC medical applications. This method revealed outstanding efficiency in an extensive range of clinical and medical applications. Utilizing MEMS technology and fabrication of microelectrodes allow DEP to be applied in biomedical applications such as manipulation, separation of specific cells from a cell mixture with high speed and sensitivity and without any labeling.

Among numerous applications, cell detection or isolating them from other cells occupy an important place in diagnostics of viral and infectious diseases such as Influenza and COVID-19. Therefore, rapid, sensitive, and automated LoC devices are urgently needed to detect such diseases. Starting from this point of view, manipulating and trapping the cells as a way to detect them by using DEP was decided as the main objective of the thesis.

This work aimed at developing a miniaturized CMOS integrated silicon microfluidic device, in line with a standard CMOS procedure, for characterization and manipulation of live and dead yeast cells (as model bio-particle organisms) using the DEP technique. Understanding the relationship between the geometry (dimension) of the microelectrode and the magnitude of DEP force, the microfluidic devices can be

designed to produce the most effective DEP implication on biological samples. In this work, interdigitated electrode arrays (IDEs) were used to manipulate the cells. This microelectrode was primarily used to detect microorganisms in a solution, based on the measurement of the variation of the dielectric constant by the concentration of the microorganisms. Therefore, finite element simulations were performed to optimize this microelectrode and adapt it to our application. Thus, the IDEs were optimized as a function of finger width and spacing between adjacent fingers.

One of the most serious matters related to DEP-based microfluidic devices is that the DEP spectra of the targeted cell should precisely be known. In this content, the DEP spectrum analysis of various cell suspensions with different medium conductivities was studied comprehensively by finite element simulation and experimentally. This study presented an optimized trapping platform for both detection and separation applications in terms of electrode dimension and electrical parameters.

Keywords: dielectrophoresis (DEP); yeast cell; bio-particle; cell characterization; cell manipulation; cell trapping; cell separation; interdigitated electrodes (IDEs); microfluidics; CMOS biosensors; lab-on-a-chip

Zusammenfassung

Die schnelle Erkennung von Infektionskrankheiten ist nach wie vor ein ungelöstes Problem, da deren Identifizierung entweder durch Kultivierung oder DNA-Analyse im Labor erfolgen muss. Die Entwicklung von Point-of-Care (PoC)-Verfahren ist ein aktueller Entwicklungstrend, der weitere technologische Impulse erfordert, um zuverlässige und kostengünstige Systemlösungen herzustellen. Durch die Miniaturisierung und Integration mikrofluidischer und elektronischer Komponenten können die Vorteile elektronischer Methoden auf den Bereich der PoC-Tests übertragen werden.

Mikrofluidik ist in der Lage, die Komponenten von Analysesystemen zu verkleinern und Flüssigkeiten mit sehr geringem Volumen zu manipulieren. Mikrofluidik bietet viele Vorteile in Bezug auf kostengünstige Materialien, geringen Probenverbrauch, hohe Empfindlichkeit und schnelle Analysezeit. Der Nutzen einer solchen Plattform erweitert sich noch, wenn sie mit Sensoren, Schaltkreisen und Aktoren zu einem so genannten Lab-on-a-Chip (LoC) System integriert wird. LoC-Plattformen auf der Basis von Mikrofluidik können komplexe Probenanalysen und diagnostische Tests durchführen und als tragbares Laborgerät am PoC eingesetzt werden.

Das Aufkommen der komplementären Metall-Oxid-Halbleiter (CMOS)-Technologie und ihre Integration in das LoC-System ermöglicht voll funktionsfähigen Sample-to-Result LoC-Geräte, was die Nutzbarkeit des Geräts auch außerhalb des Labors oder Krankenhauses unterstützt. Das in CMOS integrierte LoC-Gerät kann die Daten von Mikrofluidik, Sensoren und Aktoren verwalten. Die Elektrophorese (DEP) ist eine zerstörungsfreie und nicht-invasive Methode, die für medizinische Diagnosetests am PoC vorteilhaft ist. Diese Technik weist eine herausragende Relevanz für eine Vielzahl von medizinischen Anwendungen auf. Die Verwendung der MEMS-Technologie und die Herstellung von Mikroelektroden ermöglichen den Einsatz der DEP in biomedizinischen Anwendungen, wie z. B. die Manipulation und Trennung spezifischer Zellen aus einer Zellmischung mit hoher Geschwindigkeit und Empfindlichkeit und ohne jegliche Markierung.

Unter zahlreichen Anwendungen nimmt der Nachweis von Zellen oder deren Isolierung aus anderen Zellen einen wichtigen Platz in der Diagnostik von viralen und infektiösen Krankheiten wie Influenza und COVID-19 ein. Daher werden schnelle, empfindliche und automatisierte LoC-Geräte zum Nachweis solcher Krankheiten dringend benötigt. Ausgehend von diesem Gesichtspunkt wird die Manipulation und das Einfangen der Zellen als eine Möglichkeit, sie mittels DEP zu detektieren, als Hauptziel der Arbeit beschlossen.

Diese Arbeit zielt darauf ab, ein miniaturisiertes CMOS-integriertes, siliziumbasiertes mikrofluidisches System zu entwickeln, das mit einem Standard-CMOS-Prozess

kompatibel ist, um die Charakterisierung und Manipulation von lebenden und toten Hefezellen (als Modellorganismen für Bioteilchen) mit Hilfe der DEP-Technik zu ermöglichen. Durch das Verständnis der Beziehung zwischen der Geometrie (Dimension) der Mikroelektrode und der Größe der DEP-Kraft können die können mikrofluidische Geräte so optimiert werden, dass ihre DEP Wirkung auf biologische Proben maximiert wird. In dieser Arbeit wurden interdigitale Elektrodenarrays (IDEs) zur Manipulation der Zellen verwendet. Diese Mikroelektrode wurde in erster Linie zum Nachweis von Mikroorganismen in einer Lösung verwendet, basierend auf der Messung der Variation der Dielektrizitätskonstante durch die Konzentration der Mikroorganismen. Um die Mikroelektrode zu optimieren und um sie an unsere Anwendung anzupassen, wurden finite Elemente Simulationen durchgeführt. So wurden die IDEs als Funktion der Fingerbreite und des Abstandes zwischen benachbarten Fingern optimiert.

Einer der kritischsten Punkte im Zusammenhang mit DEP-basierten mikrofluidischen Geräten ist, dass die DEP-Spektren der Zielzellen genau bekannt sein sollten. Dafür wurde eine DEP-Spektrum-Analyse für verschiedene Zellsuspensionen unterschiedlicher Medium-Leitfähigkeit experimentell und mit Finite-Elemente Simulationen untersucht. In dieser Studie wurde eine optimierte Trapping-Plattform sowohl für Detektions- als auch für Separationsanwendungen in Bezug auf die Elektrodengröße und die elektrischen Parameter vorgestellt.

Acknowledgments

A great many people have helped me on the path to completing my doctoral thesis. So, I would like to take this opportunity and thank them all.

First of all, I would like to express my deepest gratitude to my supervisor, Prof. Dr. Christian Wenger, for introducing me to this fascinating area of science and offering me an excellent research environment. He continuously supported me with his persistent help, ideas, comments, immense knowledge, and dedication to complete this thesis work. He consistently encouraged me with my new ideas. Very special thanks for his readiness to help with a very prompt response to requests. This work would not have been possible without his guidance. It has been a great pleasure to work with you.

I would like to warmly thank my project partners, Dr. Ralph Hölzel, and his group for the valuable meetings, discussions, comments, and helps throughout this project. My sincere appreciation goes to the second Ph.D. committee member Prof. Dr. Inga Fischer, for her engagement and interest in my topic. I would also like to thank all the colleagues who helped me with the resources and facilities I required to fulfill this project; Mehmet Kaynak, Matthias Wietstruck, Mesut Inac, Rita Winkler, Beate Kuck, Eduardo Perez, Carlos Alvarado Chavarin, Subhajit Guha, Pouya Soltani Zarrin, Rahul Kumar Yadav, Elena Hardt, Thomas Natusch, Burkhard Neumann and Yvonne Mausolf. I am also really grateful to all other colleagues in IHP for their support and

help, cooperation, and guidance to fulfill this project work. I have enjoyed working alongside all of you.

I would like to thank the funder of the project, Brandenburg Ministry of Science, Research, and Cultural Affairs, for the project within the StaF program in Germany.

I am also deeply thankful to my old and new friends who endured and motivated me since I began my journey; Jördis, Viktoria, Costanza, Beate, Anne, Sebastian, Nadezhda, Elvira, Despoina, Lara, Karthik, Dariusch, Nazanin, Sasan, Fariba, Fereshteh, Nasrin, Akram, Farideh, and Hamed. I am so grateful to have you.

Finally, I would like to express my gratitude to my husband, brother, and parents for their unconditional love, motivation, and never-ending support through this journey and encouragement to pursue my interests, even when the interests went beyond land, geography, and language boundaries. This accomplishment would not have been possible without you.

Table of Contents

List of Symbols, Abbreviations, and Acronyms

LoC	Lab-on-a-chip
PoC	Point-of-care
CMOS	Complementary metal oxide semiconductor
BiCMOS	Bipolar complementary metal oxide semiconductor
DEP	Dielectrophoresis
pDEP	Positive dielectrophoresis
nDEP	Negative dielectrophoresis
AC	Alternative current
DC	Direct current
EP	Electrophoresis
EF	Electric field
EFG	Electric field gradient
2D	Two dimensional
3D	Three dimensional
***IDE*s**	Interdigitated electrode arrays
PCB	Printed circuit board
PDMS	Polydimethylsiloxane
CPW	Coplanar wave guide
PMMA	Polymethylmethacrylate
IHP	Leibniz Institute for Innovative Microelectronics

RF	Radio frequency
MUT	Material under test
BEOL	Back-end-of-line
$\boldsymbol{\varepsilon_x}$	Relative permittivity of material x
$\boldsymbol{\varepsilon_x^*}$	Complex permittivity of material x
$\boldsymbol{\varepsilon_0}$	Vacuum permittivity
$\boldsymbol{E}$	Electric field strength
$\boldsymbol{V}$	Electric potential (voltage)
$\boldsymbol{\mu, \eta}$	Fluid dynamic viscosity
$\boldsymbol{F_{DEP}}$	Dielectrophoretic force
$\boldsymbol{d}$	particle/cell diameter
$\boldsymbol{r_p}$	particle/cell radius
$\boldsymbol{CM}$	Clausius-Mossotti
$\boldsymbol{f_{CM}}$	Clausius-Mossotti factor
$\boldsymbol{\sigma_x}$	Electrical conductivity of material x
$\boldsymbol{\sigma_f}$	Electrical conductivity of the solution
$\boldsymbol{\nabla}$	Gradient
$\boldsymbol{\omega}$	Angular frequency
$\boldsymbol{\rho}$	Fluidic density
$\boldsymbol{Re}$	Real unit
$\boldsymbol{i}$	Imaginary unit
$\boldsymbol{Im}$	Imaginary part
$\boldsymbol{u_p}$	Particle velocity
$\boldsymbol{\vartheta_f}$	Fluid flow velocity
$\boldsymbol{Re}$	Reynolds number
$\boldsymbol{w}$	Channel width
$\boldsymbol{h}$	Channel height
W	Width
S	Spacing
TM	Top metal layer
AFM	Atomic force microscope
SEM	Scanning electron microscope
CMP	Chemical mechanical polishing
DIW	Deionized water
TW	Tap water
KCL	Potassium chloride
PBS	Phosphate-buffered saline
D-PBS	Diluted phosphate-buffered saline
MB	Methylene blue

Chapter I

1 Introduction

Cell manipulation and characterization are crucial when it is a question of diagnostic and clinical applications [1]. Trapping and isolation of certain cells for diseases detection [2–4], separation of live and dead cells to diagnose early-stage illnesses or diseases [5,6], purification and filtering of micro or nano-sized particles, cells, proteins, and viruses [7–10] are crucial instances in a variety of biomedical, healthcare, and biological demands. This allows early treatment and increases the chance of saving a life [58]. The evolution of lab-on-a-chip (LoC) micromachines like microfluidic platforms has facilitated complex and costly sample preparations and analyses done in the laboratories, using a single miniaturized device on the scale of a few centimeters [8–10]. This relies on the blood sample's rapid analysis or other aqueous samples and detecting the disease using a singles device [58]. This method can be replaced by the costly, labor-intense, and time-consuming traditional processes done by trained clinicians at the laboratories, taking up to several days to deliver the analysis results. This method is very quick, accurate, and requires very low sample volumes. Performing various tasks on a single device increases the precision of analysis and improves the sample preparation procedure's accuracy, reliability, and reproducibility. The advent of LoC devices, as the main building block of the Point-of-care (PoC) diagnostic technology, not only holds the potential of multiple stages of sample handling on a single device by scaling down the laboratory but also improves the robustness of device performance by limiting the contamination of laboratory

equipment and during analysis. The combination of the microfluidic-based LoC with CMOS-based integrated circuitry creates a platform for PoC diagnostics through a fully isolated setup. PoC technology development promotes the healthcare system in many ways, such as costs, practices, and result delivery, which could be highly beneficial to be used in middle or low-income countries.

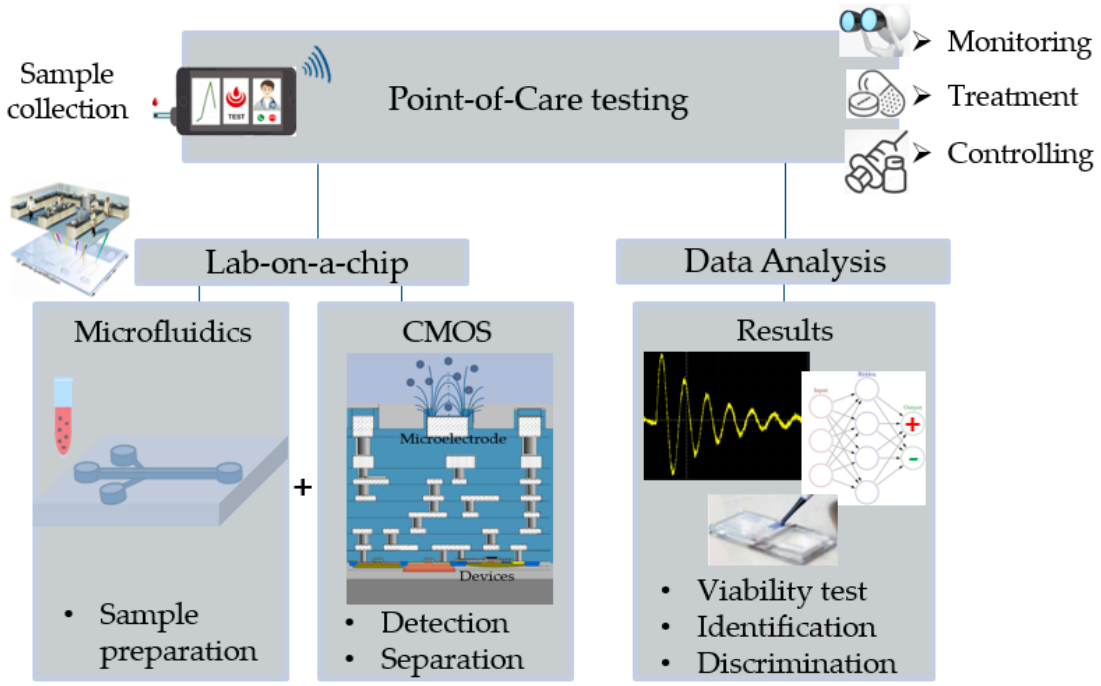

Figure 1.1. Point-of-a-care (PoC) testing device illustrating the sample-to-result processes.

CMOS technology with embedded electrodes has been extensively demonstrated for various biosensing applications so far, such as cell investigation and detection [11]. Scalability, low power consumption, high noise immunity [12] makes CMOS device favorable for disease detection purposes like viral infectious pathogens. Thus, the combination of CMOS-based microfluidics with dielectrophoresis (DEP) has been introduced as one of the most outstanding instruments in diagnostics requests for drug delivery, screening, and disease identification. Integrating microfluidic channel with CMOS can scale down in phases laboratory procedures all in a monolithic device with the capability to process micro and nano-liters samples in a fully isolated manner [125]. Implementing CMOS logics into practice are uncomplicated and consume little to no current in idle state [12]. According to the More Than Moore approach, the size of the CMOS device is getting smaller and smaller. This, at the same time, allows more functionality to fit in a smaller area and can ensure the right platform for miniaturized hand-held and versatile microfluidic devices [12] [125]. This thesis focuses on the use of CMOS-based microfluidic towards virus detection.

Yeast cells (S. cerevisiae) have been drawn by modern research as the model organism for studying bio-particles DEP spectra due to extensive knowledge about them. Yeast cells were the first model systems for studying viability determination using DEP conducted by Pohl and Hawk in 1966. Furthermore, yeast pathogens can cause infectious diseases and increase the mortality rate, especially in people with undermined immune systems. Therefore, studying yeast cells could benefit research (for microdevice proof-of-concept and efficiency testing), health applications, and several environmental safety ones. Thus, fast and reliable yeast detection with DEP offers many advantages in quality and safety protocols [13].

The main goal of this thesis is to generate a CMOS-based silicon microfluidic device to manipulate the cells using DEP with high throughput and selectivity. To develop such a successful DEP-based microfluidic platform, cells' responses to the applied inhomogeneous electric field were characterized. This is a critical step for the accurate determination of trapping and separation strategies. Therefore, to achieve this goal, the following studies were conducted:

- Designing and optimization of microelectrodes using finite element simulation, COMSOL Multiphysics, to assess optimal configuration for electrode geometry.
- Electrical analysis of the proposed DEP-based microfluidic to study different effects and potencies on the trapping force of a particle by using COMSOL FEM.
- Development of the sample chip with the optimized electrode structures.
- Development of the DEP setup and preparation of various cell suspensions.
- Testing the capabilities of fabricated CMOS-based electrodes with live yeast cells.
- Analyzing DEP spectra of live and dead yeast cells suspended in various aqueous media for trapping and separation applications with respect to electrical parameters.

Parts of this chapter have been published in [58,121,122,125].

1.1 Thesis Outline

The structure of the thesis is as follows:

- Introduction and literature review (**Chap. I**)
- Finite element modeling and electrode optimization (**Chap. II**)
- Chip fabrication, system, and sample preparation (**Chap. III**)
- Results of the measurement experiments and comparison with simulation results (**Chap. IV)**

1.2 Literature Review

1.2.1 Microfluidic LoC systems

Microfluidic systems can perform various complex tasks by including miniaturized channels, valves, mixers, sorters, and chambers. These system has been extensively gaining interest in biological and healthcare applications [14]. In general, microfluidic platforms can introduce and translate the sample through the device, perform various biological characterization and manipulation on the sample, and analyze the obtained results. To transport fluid flow across the channel through these continuous-flow devices, a mechanism is implicated. The fluid transport through the microfluidic channel is typically conducted by pressure-driven flow or electrokinetic flow [15]. The laminar flow at this micrometer-scale controls the fluid behavior unless the fluid's introduction through the channel carries out via mixers, resulting in turbulent flow initiation inside the channel [16]. The laminar flow regime occurs at a very low fluid velocity or low Reynolds-number (Re). The Re number is dimensionless and is used to characterize the fluidic behavior in the microfluidic system [17]. This number is the ratio of the inertial forces to viscous forces [17]. At low Re (< 1), when the flow is laminar and viscous forces are dominant over inertial forces, the viscous forces tend to keep fluid streams flowing very smoothly over each other without chaotic mixing [18]. As a result, a series of parallel fluid streams originate without mixing between them. This leads to precise and spatiotemporal control over the suspension fluid flow by providing a laminar flow over the system [18].

The typical diameter size of the microfluidic channel is in the range of 10-100 μm and can analyze and manipulate fluids in the orders of microliters or even less [18]. Handling low volumes samples results in less expensive setups and analysis, more accurate and rapid analysis of the sample, and efficient mass transport, large surface-area-to-volume ratios, and low thermal mass easier transfer of heat in the channels [14,18]. Microfluidic-based LoC system benefits from on-chip solution for conducting complex and sophisticated analysis and diagnostic tests that traditionally perform at the laboratories. To this end, microelectronic interfaces, sensors, and actuators are required to be integrated with LoC to form a fully automated diagnostic micromachine.

1.2.1.1 Microfluidic cell-manipulation techniques

There are many ways in which cells can be manipulated and detected within a microfluidic LoC device. Optical tweezers [19–22] can induce strong trapping force via photon refraction entering the cell with sub-nanometric precision [23]. However, utilizing a highly focused laser beam requires high power, expensive and bulky tools,

making them non-ideal for commercialization applications. Magnetic tweezers [24–28], unlike their good precision, have the same problem as optical ones. Hydrodynamic flow [29–34] is the most straightforward method, but it has a low trapping resolution. In return, the electrode-based AC electrokinetic technique [1,35–52] offers excellent benefits in terms of cost, operational power, easy electrode integration with the CMOS architecture, and requiring label-free sample preparation. This method employs DC or AC fields. DC field comes in the forms of electrophoresis and AC field in dielectrophoresis forms. Table 1.1 summarizes all these cell manipulation techniques that have been used in many biomedical approaches so far.

Table 1.1 Cell manipulation approaches

Manipulation method	Involved cell properties	Advantages	Disadvantages
Optical [19–22]	▪ Refractive index ▪ Size	▪ label-free ▪ non-destructive ▪ strong trapping force ▪ subnano metric precision [53]	▪ manipulation requires costly large specialized equipment and professional training
Magnetic [24–28]	▪ Magnetic susceptibility ▪ Size	▪ accurate ▪ high specificity	▪ labeling required ▪ expensive ▪ low capture efficiency ▪ manipulation requires costly large specialized equipment and professional training
Fluidic-hydrodynamic [29–34]	▪ Diffusion coefficient ▪ Size	▪ label-free ▪ non-destructive ▪ high precision ▪ simplest method	▪ non-spherical cells ▪ low trapping resolution
AC electrokinetics [1,35–52]	▪ Dielectric properties ▪ Size	▪ label-free ▪ non-destructive ▪ good detection and analysis precision ▪ operational simplicity ▪ low cost ▪ high capture efficiency ▪ small sample volume ▪ controllable liquid flow ▪ low sample consumption ▪ low voltage ▪ simultaneous acquisition of several sample parameters ▪ DEP can combine with other methods	▪ limited to 1-10 nm accuracy [53]

1.2.1.2 AC electrokinetics for cell manipulation

The electrode-based AC electrokinetics can be divided into two main groups of direct current (DC) or low-frequency alternating current (AC) and AC:

- **DC**
  - **Electrophoresis (EP)** is the movement of charged particles in a uniform electric field and is defined by the direction of the electroosmotic fluid stress resulting from the accumulation of the counterionic charge layer around the particle. Once a charged particle is exposed to a uniform electric field, it will be attracted towards the opposite polarity regions.
- **AC**
  - **Dielectrophoresis (DEP)** generates a non-uniform electric field (EF) that can be applied to any kind of biological and non-biological, charged or neutral particles (such as cells, viruses, bacteria, fungal, molecules, protein, DNA, micro and nanoparticles, CNT, etc.). Polarization field creation in particles takes place as a result of induced charge (negative and positive) migration towards the opposite directions. The induced dipole moment of the particle is specified by the opposite charges separation [53]. Pohl introduced the DEP technique for the first time in 1951 [54]. DEP technique comes in different forms:

    - **Conventional DEP**
    - Traveling-wave propulsion DEP on top of a linear phase-shifted microelectrodes
    - Asynchronous electrorotation in rotating fields
    - Electro-orientation of non-spherical particles in standing-wave field

An inhomogeneous electromagnetic AC field can generate cell traps, whereas the DC cannot create stable non-contact cell traps within the uniform electric fields. Utilizing DEP in microfluidic platforms has been investigated to answer various insufficiencies in chemical, biological, and medical fields. So far, this method is limited to the 1-10 nm accuracy [55], which is sufficient to manipulate and detect micron and nanometer-sized cells. DEP is among the most promising manipulation methods for micro/nano-scale systems Compared to other approaches due to its ease of integration with microfluidics, high-speed and high capturing efficiency, sensitivity, and selectivity [8]. Combining microfluidic and electrokinetic actuation platforms results in a promising direction towards complex sample handling processes [125]. This thesis aimed to apply the simplest and conventional DEP as a manipulation technique.

1.2.2 Dielectrophoresis (DEP) as a cell manipulator

As it was discussed, different techniques can realize cell manipulation. However, among these various cell manipulation methods for microfluidic devices, DEP has been utilized widely for biomedical applications and offers many advantages in terms of cell function, cost, accuracy, and analysis efficiency [56,57]. DEP is a non-invasive and label-free technique [56]. Based on the bioparticle's size and dielectric properties, DEP can be applied to manipulate the cells. By exploiting the cell and its medium's intrinsic dielectric properties (electrical conductivity and relative permittivity) [57], DEP can be used differentially to characterize and manipulate cells [58].

1.2.2.1 DEP theory

Variations in the dielectric behavior of the cells placed in a non-uniform AC electric field (Ef) is called Dielectrophoresis (DEP) [1]. When polarizable cells are subjected to a non-uniform AC-EF, as the result of the interaction between the induced dipole and the electric field, DEP force is induced on the cells [54]. Imposing an AC signal to an electrode, a non-homogenous electric field can be created. Changing the applied signal frequency can cause DEP forces in two different directions, resulting in either positive DEP (pDEP) or negative DEP (nDEP), as shown in Figure 1.2. The movement of the cell relies on the polarizability of the cell relative to its suspending solution. The DEP force is greatly dependent on the cells' size, electrical and dielectric properties, their surrounding media (Clausius-Mossotti factor), voltage, frequency, and EF vectors. At lower frequencies, where $\sigma_p < \sigma_m$ and $\varepsilon_p > \varepsilon_m$ the Clausius-Mossotti factor (f_{CM}) is negative and at higher frequencies is positive. Instead, when $\sigma_p > \sigma_m$ and $\varepsilon_p < \varepsilon_m$, f_{CM} obtains positive values at lower frequencies and negative values at higher frequencies.

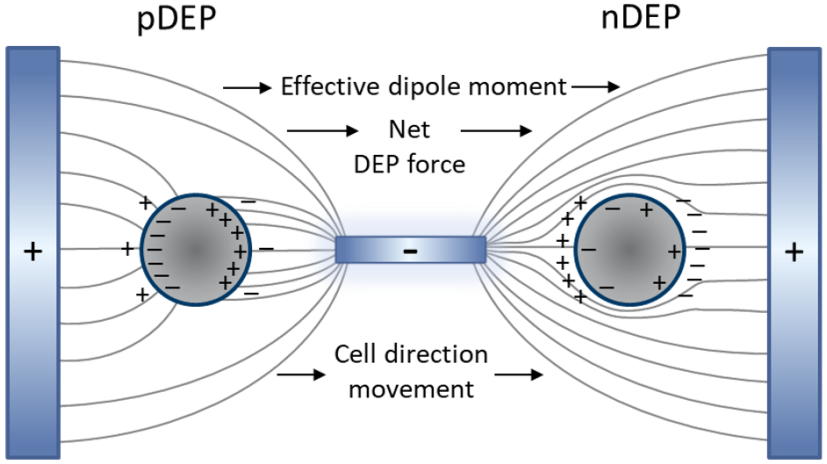

Figure 1.2. Generation of pDEP and nDEP resulted from cell polarization effect within the non-uniform electric field [58].

The crossover frequency or zero force frequency is a transition point for the real part of the CM factor from positive to negative or vice versa [59]. This point is particular for each cell suspension. At this point, the real part of the cell's effective polarizabilities and its suspending media are equal (i.e. $Re[f_{CM}] = 0$), thus making the DEP force zero. As a result of induced electric dipole and creation of the Electric field gradient (EFG) ∇E in each of the individual cells experiencing pDEP, lead to the attraction of the other cells experience the same DEP force to their neighboring cells. The polarized cells engender pearl-chains that are formed parallel to the EF direction [60]. Depending on the differential DEP forces, a particular cell population can be trapped at the electrode and detected [2,4,61], collected for further analyses (e.g., viability test) [62,63], or separated from a mixture of cell suspension in blood for purifying approaches [64]. Moreover, dead cells can be removed from live cells that cause bias during experimental measurements [65].

1.2.2.2 Cell characterization

Characterization, manipulation, and separation of biological cells are critical research topic areas because cells are the most substantial living organism elements. Cells carry essential information about biological processes and environmental situations [66]. The complex structure of cells comprises a cell wall, cell membrane, and nucleus with various proteins, lipid molecules, etc., with unique dielectric characteristics and surface charges (i.e., electrical phenotype). By exploiting the distinct differences of the cells and employing DEP electrokinetic techniques, cells can be isolated, trapped, and detected or separated.

- **Cell trapping and detection**
  Sensing pathogens (e.g., microbes, viruses, bacteria, etc.) is necessary for health, environmental, food, and air monitoring. For example, virus determination and detection are critical for early and effective infection prevention and even management. There is a dire need to develop methods for screening, characterization, detection, and identification of the environmental monitoring applications that could provide fast and timely results for our everyday life. Rahman et al. [56] has extensively reviewed the trapping and detection of various cells, viruses, bacteria, and so on using DEP.

- **Cell isolation from a cell mixture**
  Cell isolation from a cell mixture is vital in clinical applications. Thus, the secondary aim of a complete sample-to-result LoC device depends on its ability to isolate or separate a cell type from other cell types in a cell mixture. Using DEP and the CM function differing, the desired cell population pushes to high EF intensity regions using pDEP, and undesired populations push to low-intensity EF regions

by nDEP. Due to the weak trapping efficiency of nDEP, the undesirable cell moves in the stream of the fluid flow and can be washed away from the microfluidic channel. The Primary use of DEP for cell separation (live and dead yeast cells) as a means to determine microbe was reported in 1966 [67]. A rudimentary system consisting of a chamber and two electrodes were employed using this technique. While after, with the advent of advanced microelectronic (microelectrode systems and surpassing the microscale), DEP's application was developed to nanometric particles such as viruses.

1.2.2.3 Electrode geometry

Different shapes of microelectrodes can generate the EF in DEP. Since the electrode's shape, dimension, and EF distribution directly impact the DEP force distribution, the first step in manipulation approaches is defining a proper electrode structure [68]. The EFG is an essential factor influencing the cell's DEP function. In a microfluidic device, the non-uniform EF is produced by microelectrodes [68]. Electrode structure for DEP applications in microfluidic devices is classified into two main groups [68]:

- **2D – planar microelectrodes**
- **3D – Multilayered microelectrodes**

The commonly used electrode types used for DEP applications are among these two types of planar (2D) [65,69,70] and three-dimensional (3D) electrode structures [71,72]. 3D structures are integrated on sidewalls or the top and bottom of microfluidic channels, while planar structures are commonly fabricated on the bottom of microfluidic channels [73]. Although the fabrication alignment of 2D electrodes is simpler compared to 3D offers limited DEP active electric field areas [74]. Moreover, integrating optical observations with the operational investigation is less complicated using planar structures [58].

2D electrode structures have been extensively used in laboratory applications [68]. To fabricate these planar electrodes, procedures such as photolithography, thin-film deposition, lift-off, and etching are always required [74]. Remarkable examples of planar electrodes are, interdigitated electrode arrays (IDEs), castellated [75], quadrupole [76], curved [77], spiral [1], oblique [78] and matrix [79] and so forth. Among these 2D electrode structures, IDEs are the most common, favorable, and convenient form of electrode geometry used in DEP manipulation [80] and separation [8] of a specific cell population. So far, IDEs have been used to characterize and immobilize biological entities [6], proteins [37], and to determine the dielectric constant of organic fluids [81], etc.

1.2.3 Interdigitated electrodes (IDEs) for cell manipulation

IDEs were among the first microelectrode structures developed for DEP miniaturized processes after establishing the DEP concept with wire electrodes [82]. DEP devices with IDE-based electrode structures are the most common micromachines. They are usually comprised of a microfluidic channel or chamber in which the IDEs are patterned on the bottom surface of the channel/chamber [83]. The design of this electrode type relies on the two bars of adjacent parallel electrodes with two poles. These structures are usually made of Al, Au, Pt, Indium-Tin Oxide and might have equal or unequal finger width and spacing [83]. The spatial wavelength of IDEs can be fabricated in nano to the micro-meter [84]. For cell suspension introduction or injection through the IDE-based DEP devices, the fluidic area can be an open chamber or flow-through [85,86]. By applying AC signal to IDEs, an inhomogenous EF is created. This EF is powerful at the finger edges and very weak within the adjacent finger gaps (i.e., electrode intervals) and at the center of the electrode finger. The magnitude of the EF is declined with the distance from the electrode surface, and thus DEP force is significantly diminished in a vertical direction. Therefore, the DEP force is conversely proportional to the distance from the IDEs generating EF [8]. The IDE's effective DEP region is within the height equivalent to the width of electrode fingers from the IDE surface [83]. Based on the cell and its medium's relative permittivity, along with the signal's amplitude and field frequency, cells can experience a DEP force in positive and negative directions. The pDEP force moves the cells toward the strongest EF locations (i.e., finger edges), and as a result, cells can be immobilized there. The nDEP repels the cells from the IDEs and moves them against the highest EF regions. IDE's spatial wavelength (i.e., width, spacing, finger length) defines the DEP effective regions.

Owing to IDE's fabrication ease with many existing references, they are broadly merged with DEP investigations. Interdigitated electrodes have been used to capture bacteria [87], blood erythrocytes [75], DNA [88], polystyrene beads [75,89] and capture and release ribosomal RNA (rRNA) [90]. Furthermore, it was used to separate viable and non-viable yeast cells [91] and Listeria innocua cells [92] and micro or nano-particles [88,93], human colon cancer cells from RBCs [94], characterize and separate C. muris, G. lambia, and C. parvum [95], and pattern colloid particles [96]. Crews et al. [97,98] developed an equation to calculate the electric gradient term as a function of the electrode's width and spacing and the applied electric potential, and the distance above the electrode. Over the years, with the advancement of technology, IDEs have also been unified with other on-chip components for different biological applications. Suehiro et al. [99] developed a dielectrophoretic impedance measurement (DEPIM) technique for detecting biological cells and bacteria, utilizing positive DEP force to

immobilize biological particles in suspension onto an IDE array. Furthermore, IDEs also integrated with other on-chip components for various applications. As an example, Gadish et al. [89] combined IDEs with a chaotic mixer for the development of a micro-concentrator to investigate beads, B. subtilis, and spores concentrations. In other work, Vykoukal et al. [100] introduced a dielectrophoretic field-flow fractionation (DEP- FFF) micro-separator with flex-IDEs to discriminated stem cells from enzyme-digested adipose tissue. Shim et al. [101,102] used the same DEP-FFF method for isolation of circulating tumor cells (CTCs) from blood.

1.2.4 DEP-on-a-Chip

Over the few decades, much research has been carried out on the characterization and detection of the biological species on a single chip [58]. Implementing multiple features on a single chip with a minimum amount of reagents and high efficiency increases the throughput, strengthens sensitivity and accuracy, and decreases operational complexity and cost. Moreover, using a monolithic microfluidic chip allows high operation frequencies, which increases sensitivity and enables easy mass production. So far, various chip materials were used for the fabrication of such monolithic DEP-based microfluidic chips [58,122,125].

Flanagan et al. [103] explored DEP's use to characterize and identify stem cells and their differentiated progeny. To create DEP force, IDEs were embedded on glass wafers and were integrated at the bottom of a polymeric microfluidic channel. DEP demonstrated that stem cells and their differentiated deviations expand different dielectric properties. Even though this technique provided a platform to identify specific cells, it utilizes a large-scale setup. In other work, Park et al. [104] employed DEP for trapping, rotating, and detecting cells and microorganisms using DEP. The designed system applied octa-pola electrodes to trap and rotate the particles. Simultaneously, identification of these particles was achieved by in-situ impedance monitoring on the same chip. This single-chip platform included an on-chip Trans-Impedance Amplifier wire bonded to a printed circuit board (PCB) with external circuits to read-out the impedance change. To keep off the contact of the chip's electronics with aqueous biological media, PDMS wells were integrated on the chip.

Ning et al. [105] described a test system for simultaneous microwave measurement and visual validation of a live Jurkat's cytoplasm resistance employing a broadband-electrical technique. The setup is comprised of a homemade inspection station installed on top of an inverted microscope. This system incorporates an Au-based coplanar waveguide (CPW) positioned between a quartz substrate and a PDMS cover. A channel with the dimension of 150 μm wide and 50 μm height was etched underneath the PDMS cover. Miled et al. [106] proposed a microfluidic structure

containing 64 electrodes to manipulate cells. This structure was able to move, separate, and rotate the cells. Apart from the electrodes, an IDE was embedded in the microfluidic channel. The IDE was responsible for detecting the change of capacitance in the microfluidic channel. Moreover, this IDE was connected to a CMOS chip for data acquisition. The CMOS chip was used to control the DEP dependent variables (e.g., frequency and voltage) to assess the cross-over frequencies, which can be characteristic for each cell. However, this setup was not helpful for simultaneous cell manipulation and detection. Table 1.2 compares the various DEP devices for cell manipulation.

As shown in Table 1.2, various approaches have been tried to fabricate microfluidic-based LoC to enable label-free, high precision, and fast manipulation techniques. Most of the described systems have been manufactured on various rigid and robust platforms, namely glass, polymer (e.g., elastomer and PDMS), silicon, and PCB board. For example, PDMS is among the most common materials for microfluidic and chip fabrication since it is transparent and enables optical observations.

Table 1.2 Various DEP device examples for cell manipulation

Ref.	Purpose	Analyte	Microfluidic material	DEP microelectrode	Sensing microelectrode	DEP parameters	Substrate
[103]	characterization and identification	Stem cells and their differentiated progeny	PDMS	IDEs	-	25 kHz —10 MHz at 8 V	silicon wafers or glass slides
[105]	detection	Live Jurkat's cytoplasm	PDMS	gold-based coplanar waveguide (CPW)	-	10 MHz at 3 V	Quartz
[104]	trapping, rotating, and detecting	Hela cells and polystyrene particles	open-well or a closed microfluidic channel, both made of PDMS	IDEs	-	1 MHz at 76/80 Vpp	PCB
[106]	manipulation (separation) and detection	Micro-nano particles 500 nm–10 µm	Glass	L-shaped electrode	CMOS integrated IDEs	0-1MHz at >-1.3 V and <1.4	Glass on PCB

PDMS facilitates the design and integration of different components because it is compatible with lithography, deposition, and etching processes [12]. However, microfluidic devices require to be integrated with syringe pump actuators in order to able to control the fluid flow and optical cameras for data analysis. These configure structures are commonly desktop-sized and bulky, restricting the microfluidics' functionality to only laboratory-based applications. Therefore, to take a step further to PoC platforms, CMOS-based LoC has been repeatedly reported as one of the most reliable monolithic platforms to integrate the microfluidic platform with sensors, microelectronics, filters, and actuators on it [107]. Thus, this device can provide simultaneous manipulation, sensing, and detecting as well as signal processing.

Furthermore, integration of DEP and CMOS technology has been explained as one of the most ideal platforms in diagnostics applications for disease identification, drug delivery, and screening. This can be related to the low power consumption, high noise immunity, and scalability of such a system to larger setups such as PoC [12].

1.2.5 Development of the CMOS integrated microfluidics

Numerous CMOS integrated DEP platforms have been created for bio-particle characterization and manipulation (cell immobilization, purification, separation, differentiation, sorting, etc.) [39,61,80,108,109]. Combining Microfluidic LoC with CMOS technology heralds the realization of the completely CMOS miniaturized portable and versatile biomedical devices capable of detecting and diagnosing infectious diseases at the PoC. CMOS integrated microfluidic devices with embedded microelectrode have repeatedly demonstrated for biosensing applications due to their potentiality to form an autonomous hybrid system by integrating on-chip sample handling with sensors, actuators, and interfaces [12]. Table 1.3 compare various CMOS integrated DEP-based microfluidic for cell manipulation within the last two decades with this thesis state of the art [58,122,125].

Table 1.3 Comparison of some other CMOS integrated LoC devices for cell manipulation with the current thesis state of the art

Ref.	Purpose	Analyte	Microfluidic material	DEP microelectrode	Sensing microelectrode	DEP parameters	Substrate
[108]	manipulation and detection	Living cells 20–30 µm and 50- m polystyrene beads	SU8 walls and a conductive-glass lid 50-80 µm	102,400 actuation electrodes	optical sensor	800 kHz at 3.3-6.6 Vpp	CMOS
[80]	immobilization	Auto fluorescent protein R-phycoerythrin (RPE)/fluorescently labeled IgG Antibody	polyester laminating film/ITO glass slide for closing	more than 100 K cylindrical sub-microelectrodes	monitoring fluorescence intensity	100 kHz at 18 Vrms	CMOS
[111]	detecting cell concentration	Yeast cells	Silicon with silicon lid	-	IDE	-	CMOS
[60]	manipulation and monitoring	Yeast cells	PDMS well	3D octa-pole electrode	trans-impedance amplifier	1 MHz at 5Vpp	CMOS
[110]	plaque characterization in arteries	Fat and calcium in the blood	-	-	IDE	-	CMOS
[113]	particle counting/single particle sensing	Yeast cells	PDMS	-	IDE	-	CMOS
[112]	detecting the variation of fluid's relative viscosity	A mixture of glycerol/water and glycerol/alcohol	-	-	IDE	-	CMOS
[109]	single cell characterization and manipulation	Cancer cells	PDMS + SU8	Co-simulated with mm Wave sensor	mm Wave sensor ring resonator	20MHz at 0.9V/1.8V	CMOS
[39]	characterization and discrimination	cancer stem cells	PDMS	quadrupole sensor		50-500 MHz at 2-4 Vpp	CMOS
Current thesis work	characterization, manipulation, detection and separation	Live and dead yeast cells	Silicon + glass lid	IDE		1 kHz-20MHz at 2.3—20 Vpp	CMOS

Manaresi et al. [108] developed a LoC architecture based on a two-dimensional array of microsites on a CMOS microsystem to manipulate and identify particular cells using a standard CMOS microsystem. The chip with the dimension of 8 × 8 mm^2 comprised 102,400 actuation electrodes, optical sensors, and integrated memory for programming electrodes. Despite the parallel cell manipulation and identification manner, generation of the electric field to create DEP cage and cell identification was obtained through different units. To this end, counter electrodes were surrounded by in-phase electrodes to create a DEP cage. The optical sensor was used to detect the presence of the immobilized cells. Otto et al. [80] described the use of DEP as a simple technique to trap the protein particles on the CMOS device conductive surfaces. These surfaces could be narrow active regions with sizes of micrometer ranges. Furthermore, using DEP techniques, antibodies were permanently immobilized on the conductive surfaces. Even though this device can integrate with the microelectronics circuitry, data acquisition and processing circuits were absent.

Ameri et al. [109] worked on a DEP-assisted mm-Wave single-cell sensor integrated on a CMOS chip. The mm-Wave sensor utilized a ring resonator as the sensing element able to obtain very high sensitivity. The cells were positioned precisely on the sensing locations. He designed the DEP electrodes and co-simulated them with the mm-Wave resonator using EM tools to ensure no adverse effects on the sensor performance due to proximity effects. He used a combination of microfluidics and DEP to focus the cells on the desired location and implement a measure and capture mechanism. Manczak et al. [39] proposed a CMOS-based LoC platform to differentiate Glioblastoma (GBM) and to characterize cancer stem cells using an ultra-high frequency (UHF) DEP method. Using this technique, cells' characterization and detection were achieved based on individual cells' intracellular dielectric properties. To avoid the contact of the cell population suspended in a liquid carrier with the chip's electronics, a polydimethylsiloxane (PDMS) microfluidic channel was fabricated above the sensors on top of the CMOS device. Park et al. [61] proposed a CMOS-based LoC for trapping, rotation, and detection of cells and microorganisms utilizing DEP. They implemented a 3D octa-pole electrode structure directly using the built-in metal layers of standard CMOS process and demonstrate trapping and rotating of yeast cells.

Guha et al. [110–113] has extensively worked on developing single CMOS-based LoC platforms to sense and detect biological cell employing different techniques. For all of his works, variation of the relative permittivity of the material-under-test (MUT) was the sensing principle of the sensor. The change in the permittivity of the biological cell influenced the sensor's fringing field capacity and led to the shift of capacitance which could be detected via a silicon high-frequency readout circuit. An inhomogeneous EF between the IDE's consecutive fingers is created by applying a voltage to the electrodes. This technique is utilized to identify the MUT's dielectric

permittivity. In another study [111], for cytometric applications to detect the concentration of cells employing dielectric spectroscopy, he introduced a silicon integrated microfluidic channel with a CMOS sensor circuit. In this approach, the arrays of the IDE were embedded on the top part of the microfluidic channel. In other work [110], he proposed a high-frequency CMOS-based sensor with the capability of differentiating the normal blood sample from the blood sample with fat and calcium. For this study, the sensor was placed at the top and inside the catheter wall and exposed to the blood.

Moreover, he presented a high sensitive self-calibrating dynamic IDE sensor in a BiCMOS PDMS-based microfluidic platform [113]. The constant flow of the particles diluted in the fluidic solution resulted in capacitive pulses from the sensor embedded in the oscillator, which could be ultimately translated to frequency modulation using an integrated phase-locked loop demodulator. Using this radio frequency (RF) CMOS chem-bio sensor, the relative viscosity variation in an aqueous solution was also investigated [112]. The fringing field between the adjacent fingers was used to detect the MUT's dielectric permittivity. Therefore, in this work, we use a similar IDE developed by Guha et al. and optimized it to adapt it to our DEP application.

1.3 Motivation and State of the Art

The above-mentioned literature review shows that these published methods offered opportunities to manipulate and detect bio-particles on a CMOS chip. However, they employed relatively large-scale systems with polymeric microfluidic channels, which were not compatible with the standard CMOS process flows. The bulky polymeric LoC systems restrict the device performance by initiating parasites to the setup. Furthermore, due to the fabrication ease of PDMS-based microfluidic devices, they are more convenient for lab-based research than industrial applications [114]. Among various alternative materials available for microfluidic applications, such as polymethylmethacrylate (PMMA), amorphous polymers, thermoplastics, silicon, and epoxy photoresist SU-8 [115], silicon is a reliable replacement for polymer in microfluidic devices due to its noble integration robustness with electronics [58].

Moreover, silicon can be used in combination with fluidic applications that require high-temperature endurance, high aspect ratio structures, and very high-resolution channel alignments [115]. One of the most outstanding advantages of silicon is the possibility of fabricating thin membranes, which improves the stability of the device to high-temperature ramp rates by reducing thermal mass [115,116]. Silicon's high thermal conductivity ensures a uniform temperature distribution [117]. Therefore, from one side, the interest in using silicon microfluidic platforms is rising.

On the other hand, the demand for physically interfacing the fluidic samples with electrodes and sensors for analyzing biological and nonbiological samples increases the need to comb CMOS integrated circuits' capabilities with microfluidics. Combining these technologies offers excellent opportunities in the biomedical field for point-of-care diagnostics, implantable devices, and high throughput screening[118]. The CMOS hetero-integrated technology enables integration of sensors, microfluidic channels, and circuitry as monolithic devices. This approach is very profitable for future applications, since trapping, sensing, detecting, and analyzing can be achieved on a single-piece chip [58].

In contrast, polymeric-based microfluidic channel approaches lack sensor and circuitry integration on a single chip solution. The combination of CMOS and microfluidics on the same die allows highly miniaturized LoC fabrication. Furthermore, CMOS processing's high alignment accuracy provides smaller distances between the isolated fluidic and electrical interfaces. Integration of microfluidics with the CMOS process for miniaturized microsystems assists the portability of the LoC and enables fast diagnostic results even out of non-laboratory conditions. However, the lack of promising integration methods remains a challenge, and realizing a fully functional device is under research. Only one report on detecting cells using a silicon microfluidic channel had been published. However, in this work, due to the use of silicon as the channel closing lid, the optical observation remained challenging [58].

Moreover, among these reported works, some of the systems were benefited from/ potential for using the same CMOS integrated platforms for sensing and detection. However, using a single IDE electrode for DEP manipulation and sensing/detecting accompanied by microelectronics circuitry for readout on one single chip, except one work that used a quadrupole electrode, has not yet been explored.

This thesis presented and designed IDEs to characterize and manipulate the cells using the DEP technique. This IDE platform can be integrated with the circuit and microfluidic channel by IHP's CMOS process line for simultaneous immobilization, sensing, and detection of biological and non-biological particles. The IDE's geometry has been adapted from the previous works done at IHP [119,120]. The objective of this PhD work is to enable the design of an IDE with the capability to manipulate micron and nano-sized biological particles.

To this end, we investigated a five × five mm^2 CMOS integrated silicon-based microfluidic device comprised of six different IDEs, with various spatial wavelengths (geometrical ratios), for the immobilization and separation of live and dead yeast cells employing DEP. Using glass to encapsulate the microfluidic channel enabled simultaneous electrical investigation and optical observations. The concept of

incorporating both the fluidic solution and electrical components improves the miniaturized LoC's functionality and precision by using discriminate interfaces for microfluidics and electrical connections. This system offers operational simplicity and a low voltage DEP approach that ensures the portability of the LoC device. Costly and multi-step fabrication procedures substitute the hetero-integration technology. The highly-alignment precision of the microfluidic channel on CMOS electronics warrants a reliable and reproducible integration approach compared to the relatively large polymeric-based microfluidic LoC systems. The opportunity to immobilize, sense, and detect cells on the same chip increases the measurements' reproducibility using less complicated setups. The contamination-free fabrication process of CMOS integrated microfluidic offers reliable measurements. One of the most significant advantages of using silicon instead of polymer to fabricate the microfluidic channel is the high integration level of the sensors and circuitry on a monolithic platform. State-of-the-art of this CMOS technology offers chances to immobilize, sense, and detect the particles on the same chip. However, this thesis's main contribution is to create a platform for DEP characterization of the cells, which counts as the preliminary and fundamental step for detection applications. The circuitries for sensing and read-out of the cells are in the outlook of this work. Thus, combining the microfluidic platform with the same microelectrode structure for simultaneous DEP characterization and sensing is expected to illustrate a landmark stage for the next generation of PoC devices [58,121,122,125].

The electrode structures used in this study followed the Guha. et al. approach used IDEs to sense and detect biological cells on a single chip [110–113]. This sensor structure, which has been already established at IHP, in Frankfurt/Oder, Germany, for radio frequency (RF) bio-sensing applications, inspired us to use a similar DEP structure design. Thus, this enables us in the future by adding circuitry to the electrode to simultaneously characterize and sense the cells using the same structure. This method improves the accuracy and sensitivity of the LoC device. This interdigitated electrode geometry was optimized to be adapted to our DEP application using finite element simulations. To this end, a systematic simulation study was conducted using COMSOL Multiphysics (version 5.3) [121,122]. A wide-ranging of diverse IDEs with varying spatial wavelength (electrode width and spacing between fingers) were modeled. To verify and validate the simulation results, some promising IDEs were elected and proposed for fabrication [58].

Additionally, after successfully characterization and manipulation of yeast cells, our device's ability to carry out separation action was evaluated. Based on the results, the isolation action was achievable using the same IDEs without any additional or specialized electrode structure. This achievement ensures maintaining device simplicity.

1.4 List of Publications and Presentations

Data presented in this thesis was partially published in peer-reviewed journals or peer-reviewed conference proceedings. Some result parts were further presented at international conferences in talk or poster formats.

Peer-reviewed Journal Articles and Conference Proceedings:

[1] **Matbaechi Ettehad, H.**; Guha, S.; Wenger, C. Simulation of CMOS compatible sensor structures for dielectrophoretic biomolecule immobilization. In Proceedings of the COMSOL—Bioscience and Bioengineering COMSOL, Rotterdam, Netherlands, October **2017**; p. 6.

[2] **Matbaechi Ettehad, H.**; Yadav, R.K.; Guha, S.; Wenger, C. Towards CMOS Integrated Microfluidics Using Dielectrophoretic Immobilization. *Biosensors 9(2)* **2019**, 77.

[3] **Matbaechi Ettehad, H.;** Soltani Zarrin, P.; Hölzel, R.; Wenger, C. Dielectrophoretic Immobilization of Yeast Cells Using CMOS Integrated Microfluidics. *Micromachines* 11(5) **2020**, 501.

[4] **Matbaechi Ettehad, H.;** Wenger, C. Characterization and separation of live and dead yeast cells using CMOS-based DEP microfluidic. *Micromachines* **2021**, *12*, 270.

Conference presentations (Talks/ Poster):

[1] **Matbaechi Ettehad, H**.; Guha, S.; Wenger, C. CMOS compatible sensor structures simulation for dielectrophoretic biomolecule immobilization. International COMSOL conference on Bioscience and Bioengineering COMSOL, Rotterdam, Netherlands, 19 October **2017**.

[2] **Matbaechi Ettehad, H**.; Guha, S.; Wenger, C. Simulation of dielectrophoretic immobilization of Micro-Nano ranges beads in a Silicon based microfluidic platform. In Proceedings of the Dielectrophoresis, Surrey, United Kingdom, July **2018**.

[3] **Matbaechi Ettehad, H**.; Wenger, C. Design and fabrication of Silicon based microfluidic devices. BTU GRS-Cluster "FuSion", Cottbus, Germany, 8 October **2019**.

[4] **Matbaechi Ettehad, H**.; Wenger, C. Dielectrophoretic immobilization of yeast cells using different size interdigitated electrodes integrated into the silicon microfluidic channel. In Proceedings of the Dielectrophoresis, Arizona, US, July **2020**.

[5] **Matbaechi Ettehad, H**.; Wenger, C. Characterization and manipulation of yeast cells using microfluidic-based interdigitated biosensor. In Proceedings of the European Biosensor Symposium (EBS 2021), Wildau, Germany, March **2021.**

[6] Manganelli, C. L.; **Matbaechi Ettehad, H**.; Masood, M.; Spirito, D.; Wenger, C. Towards CMOS compatible materials for Surface enhanced Raman Spectroscopy (SERS). In Proceedings of the European Biosensor Symposium (EBS 2021), Wildau, Germany, March **2021**.

Chapter II

2 Components Modeling and Optimization

DEP characterization can be utilized using enhanced planar technologies like complementary metal-oxide-semiconductor (CMOS) using interdigitated electrode arrays (capacitive biosensors). Since DEP can be an operative and functional means of cell manipulation and separation, it requires careful balancing between interplaying forces within the microsystem and optimizing the electrode geometry to produce the compelling force. Therefore, a COMSOL model was produced to assess different effects and potencies on the immobilization or trapping force and assess the optimal configuration for the electrode geometry. In this chapter, the dielectrophoretically immobilization of micron and submicron size particles using interdigitated electrode (IDE) arrays were presented by finite element simulations. CMOS compatible-based IDEs have been embedded into the microfluidic channel. A thorough investigation of the DEP force propulsion, the IDE's dimensional parameters, and the fluid dynamics are necessary for allowing the complete platform for CMOS-based microfluidics and detection of micron and submicron particle sizes. The electrode design was done by robust FEM analyses to avoid iterative, time-consuming, and costly fabrication processes. Non-biological and homogenous particles were used as model particles for the preliminary microfluidic test analysis. To produce DEP force, an AC field was applied to the IDE. This chapter follows the influence of the effective internal and external properties, such as driving voltage, DEP filed frequency, fluid flow velocity,

and IDE's geometrical parameters were investigated. Parts of this chapter have been published in [121,122].

2.1 Interdigitated electrodes (IDEs) design

Arrays of microfabricated interdigitated electrodes (IDEs) are the most common and easiest form of electrode geometry for the DEP manipulation and characterization of biological particles (e.g., viruses and cells) through microfluidic biochips. These electrodes are used to trap and separate particles or purification of live cells from dead cells. IDEs are the subsets of the advanced technological process required for immobilization of the cells [122].

The electrode geometry used in this work is similar to the electrode geometry that has been previously established for nearfield biosensing applications [120,123]. The IDE fabrication was performed based on the standard 250 nm high-performance SiGe BiCMOS technology of IHP. This unit (Figure 2.1a) was embedded on the bottom of the microfluidic channel and relied on the multi-fingered planar interdigitated capacitor arrays. This IDE was fabricated on the topmost metal level of the back-end-of-line (BEOL) stack of the CMOS/BiCMOS process (Figure 2.1b). This IDE was used to model the dielectrophoretic structures [122].

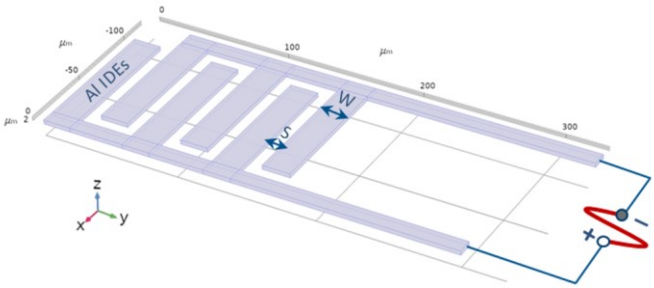

(a)

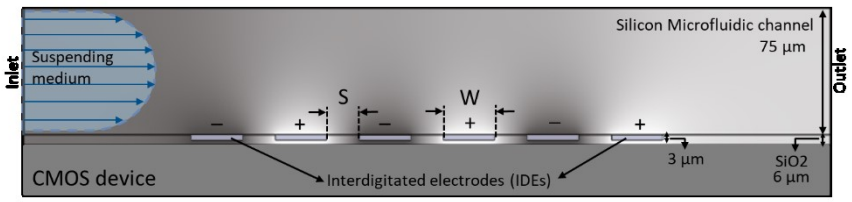

(a)

Figure 2.1. (a) Multi-fingered planar interdigitated electrodes (IDEs), (b) Cross-sectional view of IDEs embedded in the microfluidic channel [58].

We initially used the same IDE structures in this work, which were previously established for high-frequency CMOS dielectric sensors [119]. However, to enhance

the performance of DEP, the geometry of these IDEs was optimized using COMSOL simulations [122]. Different IDE structures with various geometrical parameters were simulated.

2.1.1 Working principle of IDEs

A non-uniform electric field (E) between the adjacent fingers is generated by applying AC electric potential to the electrodes. When cells are subjected to this AC field, dipole moments are induced in the cells. As a matter of the change in the cells' dielectric behavior, a net DEP force is generated on the cells and causes them to move within the field gradient. The direction of the cell motion is defined by the field gradient vector ∇E. Gradient of the electric field is significantly influenced by the geometry of the electrode. Taking to account the electrode geometry is a crucial consideration for experimental designs in controlling the field factor. For example, an optimum electrode dimension benefits from a modest applied voltage and high magnitude of field factor, which results in producing a great DEP force on a cell. Figure 2.2 illustrates the microfluidic channel's schematic with embedded IDEs at the bottom of the channel and material under test (MUT) flowing through the channel over electrodes. The MUT consisting of the carrier fluid and suspending cells flows through the channel. The direction of the cell's motion depends on the gradient of the electric field [122].

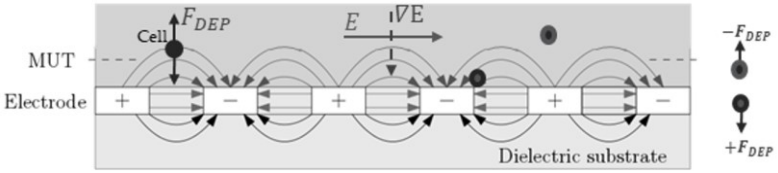

Figure 2.2. Electric field (E) distribution of the IDEs within the microfluidic channel. MUT is the material under test, consisting of the carrier fluid and suspending cells [122]**.**

2.2 Finite Element Modeling and Simulation

2.2.1 Model definition

The 2D and 3D models were developed using the COMSOL Multiphysics® tool. For simulations, the fluid flow in the microfluidic channel was considered through a single inlet and a single outlet. Arrays of IDEs were utilized to create a non-uniform electric field that impacts cells' trajectory due to dielectrophoretic forces. The DEP force was optimized for different geometrical parameters of electrodes, particle size, and flow velocity. Figure 2.3a demonstrates the chip design (in 3D geometry).

However, to reduce the computational time, the simulation studies were all done in 2D, as described in Figure 2.3b. For these simulations, various geometrical parameters of IDE, such as width and spacing between adjacent fingers, were studied. The electric current (ec) module was used as the physics interface in conjugation with particle tracing for fluid flow (fpt), drag, and dielectrophoretic forces modules [122].

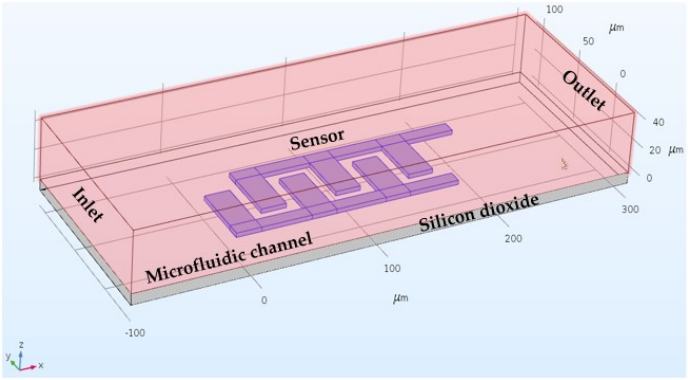

(a)

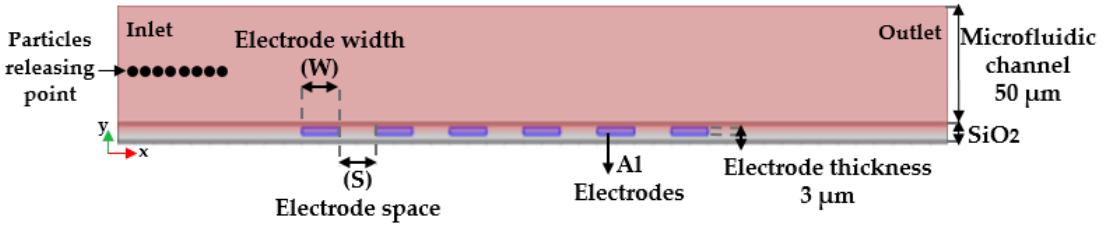

(a)

Figure 2.3. Finite element modeling: (a) 3D and; (b) 2D geometry modeled to investigate the DEP on particle trajectory [122].

Different equations were used to simulate the cells' flow path diluted in the fluidic solution and subsequently trap them on the IDE by DEP [122]. The laminar flow (spf) module was applied to model the fluid tracing through the microfluidic channel. The velocity of the fluid driven through the channel is calculated based on the Navier–Stokes Equation shown in 2.1. Figure 2.4a illustrates the velocity field profile across the channel [122].

$$0 = \nabla \cdot \left[-pl + \mu(\nabla u + (\nabla u)T) - \frac{2}{3}\mu(\nabla \cdot u)l\right] + F$$

$$\nabla \cdot (\rho u) = 0. \qquad \textbf{2.1}$$

Where p is the pressure, μ is the dynamic viscosity, u is the velocity vector, and F is the volume force vector imposed on the fluid. When a cell is suspended in the fluidic medium, it can be influenced by several forces, such as drag force caused by the fluid flow. Drag force has the same direction as the fluid flow. This force is calculated based

on Stokes drags law and is also applicable for creeping flows with Re_r « 1, as seen in Equations 2.2 and 2.3 [122].

$$F_{Drag} = \left(\frac{1}{T_c}\right) \cdot m_c(u - v), \quad \textbf{2.2}$$

$$\tau_c = \rho_c \cdot \frac{{d_c}^2}{18\mu}, \quad \textbf{2.3}$$

where τ_c is the velocity response time of cells, m_c is the cell mass, v velocity of the cells, u fluid velocity, μ fluid viscosity, ρ_c cell density, and d_c is the diameter of the cell. Moreover, to absorb and trap the particles, the dielectrophoretic force (F_{DEP}) is essential, given by Equation 2.4. The cells were subjected to a non-uniform AC electric field [122].

$$F_{DEP} = 2\pi {r_c}^3 \varepsilon_f real(CM) \nabla |E|^2, \quad \textbf{2.4}$$

$$CM = \frac{(\varepsilon_c{}^* - \varepsilon_f{}^*)}{(\varepsilon_c{}^* + 2\varepsilon_f{}^*)}, \quad \textbf{2.5}$$

$$\varepsilon_f^* = \varepsilon_r - \left(\frac{i\sigma}{\omega}\right). \quad \textbf{2.6}$$

Here, r_c is the cell radius, ε_f is the medium's relative permittivity, ε_f^* and ε_c^* are the fluid and cell's complex permittivities, respectively. E is the root-mean-square of EF. Permittivity is a complex quantity that functions with the electric field's angular frequency (ω) and conductivity (σ). Based on the electric potential (V), which was coupled with the electrode structure (as shown in Figure 2.4b), the electric field (E) was simulated by the ec module and was calculated based on Equation 2.7 [122].

$$E = -\nabla V, \quad \textbf{2.7}$$

This relationship illustrates the local electric field E, which is linked to the potential field V. The intensity of E points to the direction of the greatest rate of potential V decrease. This means that the E intensity is obtained from the negative gradient of the scalar potential, in other words, by a difference in the electric potential between two points. The fpt module, i.e., the particle tracing module (Figure 2.4c), contains the equations governing the motion and trajectory of cells in the fluid flow under the influence of the drag and DEP forces. Regardless of buoyancy, gravity force, and Brownian motion forces, the relevant equation can be written as shown in Equation 2.8 [122].

$$m_c \frac{dv}{dt} = F_{DEP} - F_{Drag} = F_T, \qquad 2.8$$

where, m_c is the mass of cells, v is the fluid velocity, and F_T is the total force acting on the cell.

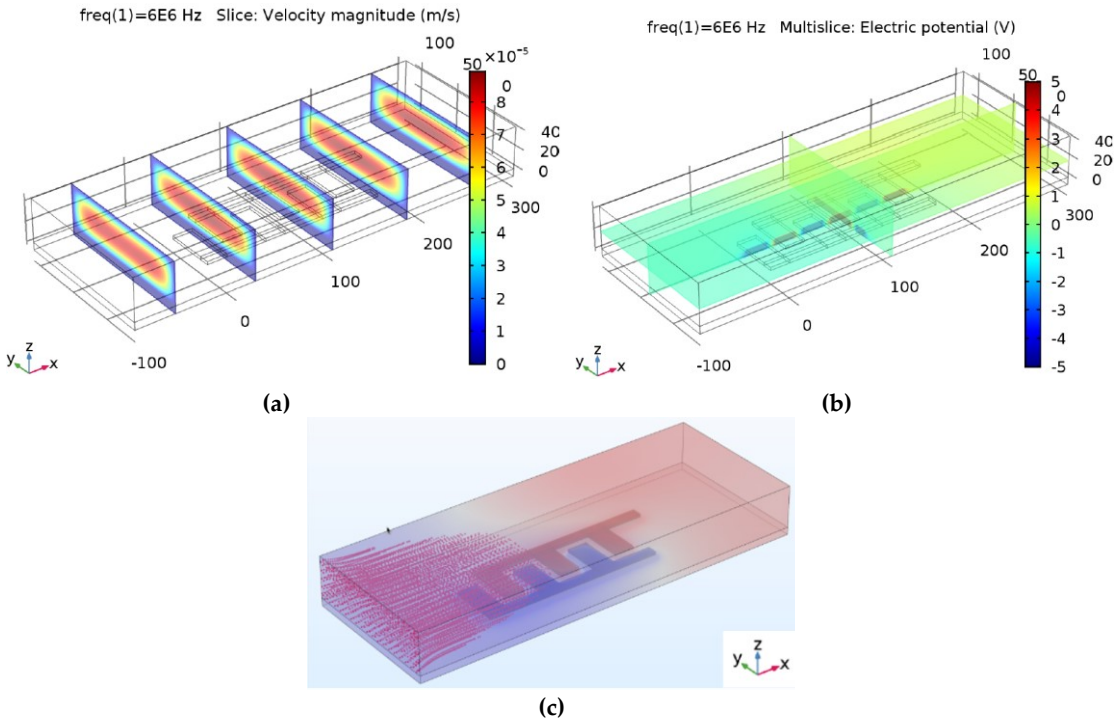

Figure 2.4. 3D simulation results showing: (a) Multislice view of the velocity field; (b) coupled electric potential with the IDEs, and; (c) particle trajectory.

2.2.2 Boundary conditions

To the fluidic boundary, an electrically insulated boundary condition was applied. This condition was active on the exterior boundaries of the model. A peak-to-peak (positive and negative) electric potential was imposed on the IDEs. As a further initial condition, a zero Volt electric potential was then applied to the electrodes. The wall condition of no-slip was imposed on the microfluidic channel boundary. This condition (u = 0) was used to model solid walls for modeling the tracing of particles in the fluid. The inlet and the outlet were positioned perpendicularly to the device structure. The inlet condition was set as velocity to apply a well-posed condition, and the outlet was set as pressure. The initial fluid flow (v_0) was set to 50 μm·s⁻1. The flow rate value was then altered to study its influence on the immobilization of particles. The initial fluid velocity was applied at the inlet, and the outlet was kept to zero flow rate with suppressing the backflow of the medium. For tracing the particles, the conditions of disappearing or freezing walls

were chosen for the outlet. The disappearing condition was used when the particles were released from the channel, and they were no longer interested. To calculate the velocity and the position of particles releasing from the channel, the freezing wall condition was used. Upon applying this condition, particles could stay frozen at the channel outlet boundary [122].

2.2.3 Simulation analyses

The simulation process for particle tracing analysis was done in three steps. To simulate the electric potential and create a non-uniform EF, the electric current module was applied. In order to calculate the flow velocity through the channel, a stationary analysis was performed. A particle tracing module was used to model dielectrophoretic force through the channel. Figure 2.5 describes an example of the simulation analysis steps for 3.5 μm diameter-sized particles. As shown in Figure 2.5a, a total peak-to-peak voltage value of 5 V (2.5 V and −2.5 V) was applied to the IDEs. Figure 2.5b shows the electric field contour plot where the electric field is intensified between the IDE fingers. Figure 2.5c demonstrates the fluid flow velocity within the channel. The pressure within the microfluidic channel was constant. A time-dependent solution was carried out for particle tracing simulation using the values calculated from frequency domain analysis, as shown in Figure 2.5d [122].

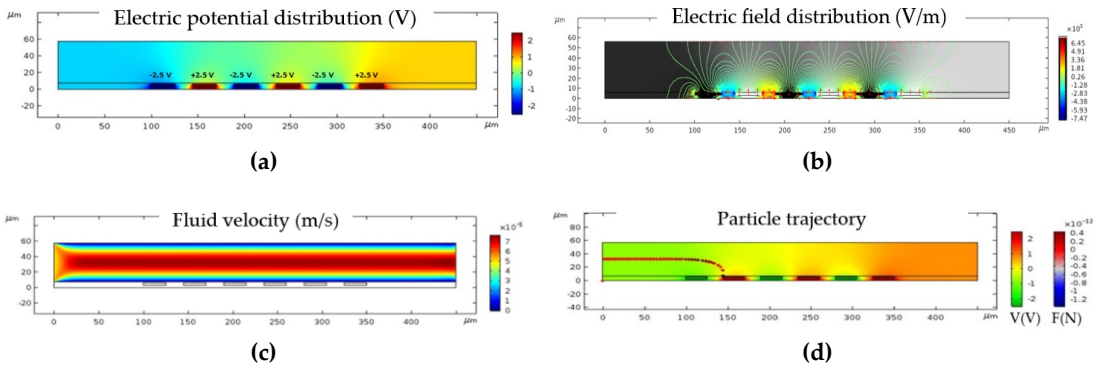

Figure 2.5. Finite element simulation steps to achieve particle immobilization for particles with 3.5 μm diameter size: (a) Distribution of EF in the microfluidic channel at V = 5 V at 10 MHz; (b) Contour plot of illustrate the EF distribution; (c) Velocity field distribution in the microfluidic channel; (d) Trajectory of particles as a result of forces acting the particles and immobilization of particles at the IDEs [122].

Since this study aimed to immobilize the particles on the electrodes, simulations were performed systematically to optimize the electrode geometry and find suitable electric field frequency ranges and fluid velocities to attract different size particles [122].

The micron and submicron-sized particles used for these simulations were in the range of 10, 3.5, and 0.5 µm. Keeping the primary model simple and reducing the complex parameters, these particles were considered homogeneous spheres and non-biological. The fluid carrier was supposed to be water. The influence of osmotic pressure on the particles was not considered for these simulations. Table 2.1 represents the properties of the particles for the simulations [122].

Table 2.1. Particle properties used for FEM [122]

MUT	Particle Diameter (µm)	Density (kg/m³)	Permittivity	Conductivity (S/m)
Particle 1 (platelet)	3.5	1000	50	25
Particle 2	0.5	1000	50	25
Particle 3	10	1050	5	0.69

The fringing electric field's magnitude is enlarged between two consecutive IDE fingers (Figure 2.6a). Due to the increased EFG at rectangular electrode corners, the EF distribution is non-uniform [124]. This leads to the attraction and immobilization of the particles to the electrode edges. Figure 2.6b shows the exponential decrease of EF magnitude with increasing distance to the IDE arrays [122].

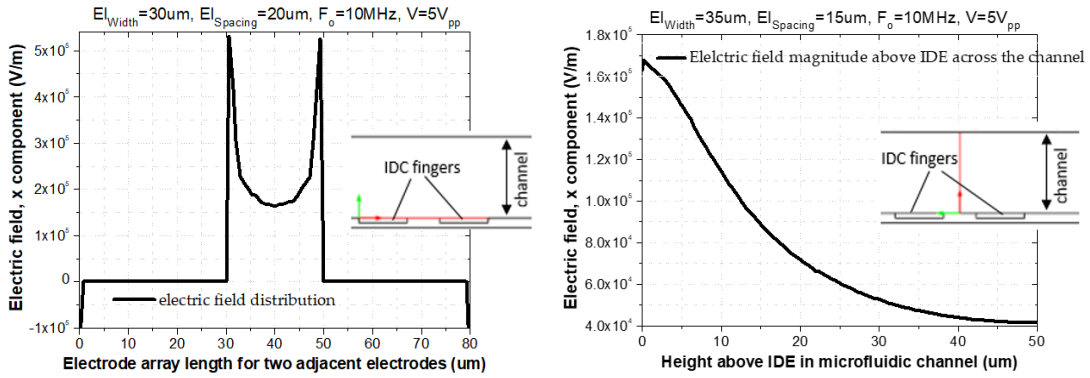

(a) **(b)**

Figure 2.6. (a) Distribution of EF above two consecutive IDE fingers; (b) Reduction of EF magnitude by increasing distance from the IDE surface [122].

To visualize the simulated EF, a cut line (2D data set) was used. This cut line creates lines through the modeled 2D geometry, as shown in cross-sectional schematic figures above. The EF was plotted along the red arrow-line, Figure 2.6a,b. The EF distribution was calculated based on Equation 2.7 [122].

2.3 Simulation Results

2.3.1 Impact of frequency on DEP

By calculating and plotting the Clausius-Mossotti (CM) factor diagram, the field frequency which results in the immobilization of the particles at the IDEs can be predicted. CM Factor is a frequency-dependent parameter that results in positive and negative DEP. Changing the frequency results in the crossover frequency shift and can stimulate the DEP force between positive and negative values. The CM factor's real part for 10 μm-sized particles in water was bounded between +1 and −0.5. Positive DEP forces act on the particle when the real part of the CM factor is positive. This results in the attraction of the particles to the regions of EF intensity maxima, i.e., electrode edges. Vice versa, when Re[CM] < 0, particles are repelled from high EF intensity regions and consequently deviated from the IDEs. Plotting the CM factor using MATLAB® enabled the prediction of particle's DEP behavior and, as a result finding the suitable frequency range for positive DEP. Figure 2.7 illustrates the CM factor for 10 μm diameter size fluorescent particles [122].

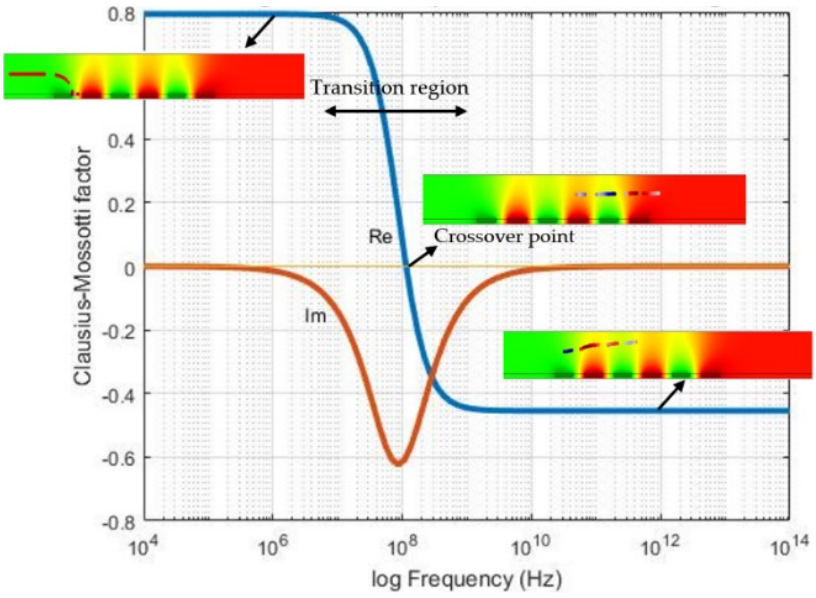

Figure 2.7. Clausius-Mossotti (CM) factor for a particle with 10 μm (in diameter) particle suspend in water over a broad frequency spectrum [122].

Particle properties are shown in Table 2.1. For positive real part values (Re[CM] > 1), particles were immobilized at the IDEs because positive DEP was dominating. However, for negative real part values (Re[CM] < 0), the opposing negative DEP force acts on the particles. This results in the deviation of particles from the IDEs. Thus, for reliable pDEP characterization, frequencies below 10 MHz must be chosen for this type of particle and its suspending media [122].

2.3.2 Impact of voltage variation and particle size

Simulation assumptions for tracing the particles with 3.5 and 0.5 µm diameter sizes are shown in Figure 2.1. The immobilization of particles was positively related to the voltage. As shown in Figure 2.8a, for the same IDE structure, the immobilization of 3.5 µm size particles occurred at 1 V. In contrast, the immobilization of 0.5 µm particles occurred at 8 V, as shown in Figure 2.8b [122].

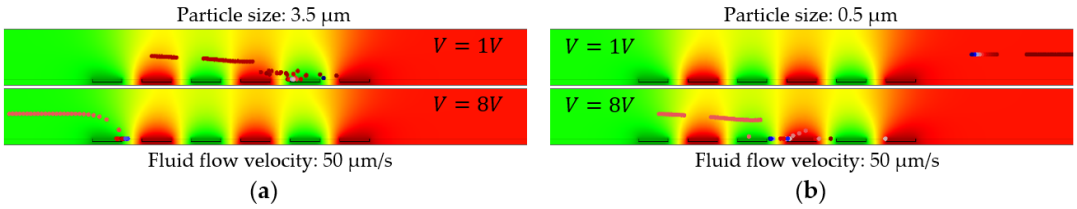

Figure 2.8. Voltage change influence on particle trajectory for particles at constant fluid flow velocity (50 µm·s⁻¹) and field frequency (1 MHz) for: (a) 3.5 µm and; (b) 0.5 µm diameter-sized particles. IDE has a width of 30 µm and spacing of 20 µm) [122].

The enforced DEP on the particles is positively associated with the electric potential, and for the trapping of smaller particles on electrodes, higher electric potentials are needed to overcome the drag force from flow and compensate for the mechanical force [122].

2.3.3 Impact of fluid flow velocity

To immobilize the submicron particle and study the influence of fluid flow velocity, the voltage was kept at CMOS compatible ranges, and the flow velocity was varied. The trapping of submicron-sized particles inversely impacted the flow rate. Figure 2.9 shows a representative simulation result when the fluid velocity was reduced at a constant voltage of 5 V. The 50 µm·s⁻¹ fluid flow velocity was set as the reference. It was seen that lowering the fluid velocity to 30 µm·s⁻¹ enhanced the particle immobilization [122].

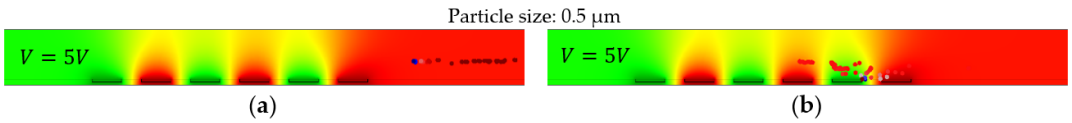

Figure 2.9. Fluid flow velocity impact on particle trajectory of the 0.5 µm particles at a constant frequency of 1 MHz and voltage of 5 V: (a) at 50 µm·s⁻¹; and (b) 30 µm·s⁻¹ flow rates [122].

2.3.4 Impact of IDE's geometry on DEP

The influence of the electrode's geometrical dimensions on particle trajectory was investigated by simulations. For these simulations, the voltage, field frequency, and flow velocity were kept constant. COMSOL® applications can calculate the immobilization probability of the IDE structures. According to these analyses, the immobilization probability was specified as the ratio of trapped particles to the total number of particles diluted in the medium. The impact of the fringing EF for various electrode width to spacing ($\frac{S}{W}$) ratios versus immobilization probability are shown in Figure 2.10 [122].

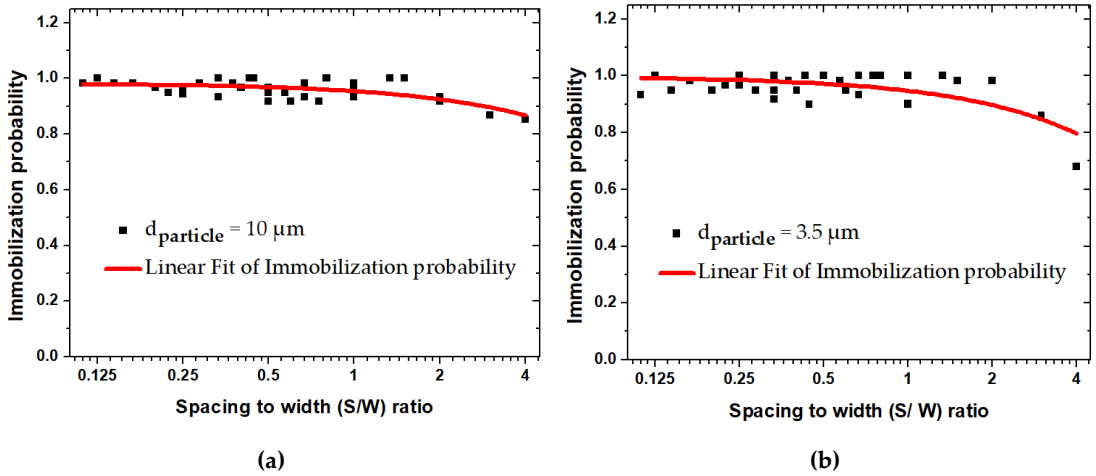

Figure 2.10. Simulation assumptions based on immobilization probability (IP) for structures with different spacing to width ($\frac{S}{W}$) ratios at 1 MHz and 50 µm·s^{-1} for: (a) 10 µm; (b) 3.5 µm-sized particles [122].

For the systematic simulations, the spacing varied between 5 and 20 µm, and the width varied between 5 and 45 µm. These graphs define the immobilization probability (IP) for two particle sizes (10 and 3.5 µm). For both of the particles, IP was greater than 0.9 for ratios below 2. At larger rates, IP values declined for both of the particles. For IDE structures with ratio 4, this attenuating trend became significant for smaller particles. The IDE structure was optimal when the spacing to width ratio was lower than 2. This trend will be discussed more in detail in Figure 2.11 and Figure 2.12 [122].

In the next simulation step, the IDEs were assigned into two groups of uniform and non-uniform geometries. Uniform IDE pertains to symmetrical geometries with equal sizes of width and spacing, and non-uniform structures have asymmetric width and spacing sizes. Figure 2.11 shows the IP trend for uniform electrode structures. Using the uniform electrode geometries, the IP for bigger particles (10 µm) was about

100% in all cases. IP of smaller particles (3.5 µm) raised by 90% for IDEs with 10 µm spacing and 100% for IDEs with larger spacing. For small particles, IP was almost zero for IDEs with spacing and width of 5 µm, while for bigger particles, it was nearly 1. As a result, it is assumed that the uniform IDE design is optimized when spacing and width are larger than 10 µm [122].

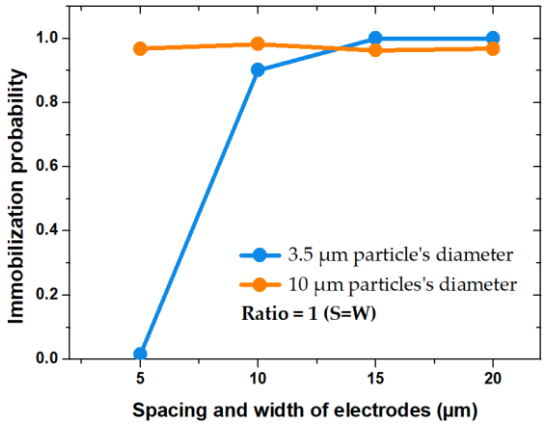

Figure 2.11. Impact of uniform IDEs ($S = W$) on IP under the same voltage, frequency and fluid velocity. In these simulations, 10 and 3.5 µm-size particles were used [122].

Figure 2.12 demonstrates the impact of non-uniform electrode structures on the immobilization probability of particles (3.5 µm and 10 µm). Figure 2.12a,b illustrate the IP at the constant spacings of 5 µm and 20 µm for varying widths (5 – 45 µm). Figure 2.12c,d represents the IP at constant widths (5 and 45 µm) for different spacing (5 – 20 µm). Simulation assumptions showed that variation of width and spacing has less impact on IP of 10 µm size particles compared to smaller particles (3.5 µm). For the constant spacings of 5 µm, IP dropped significantly for 5 and 10 µm widths, as shown in Figure 2.12a. Varying the spacing and keeping the width constant at 5 and 45 µm, it was seen that for both particle sizes, IP is optimum for bigger width, as shown in Figure 2.12c,d [122].

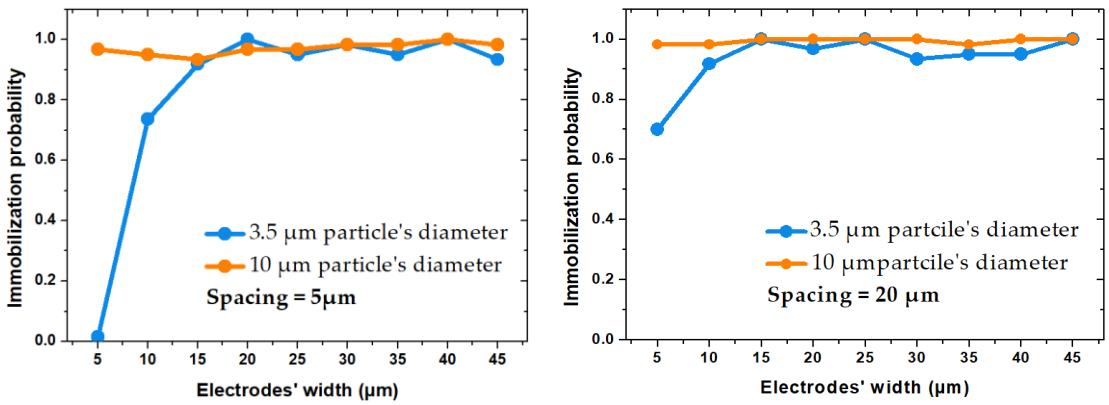

(a) **(b)**

Figure 2.12. Continued to the next page

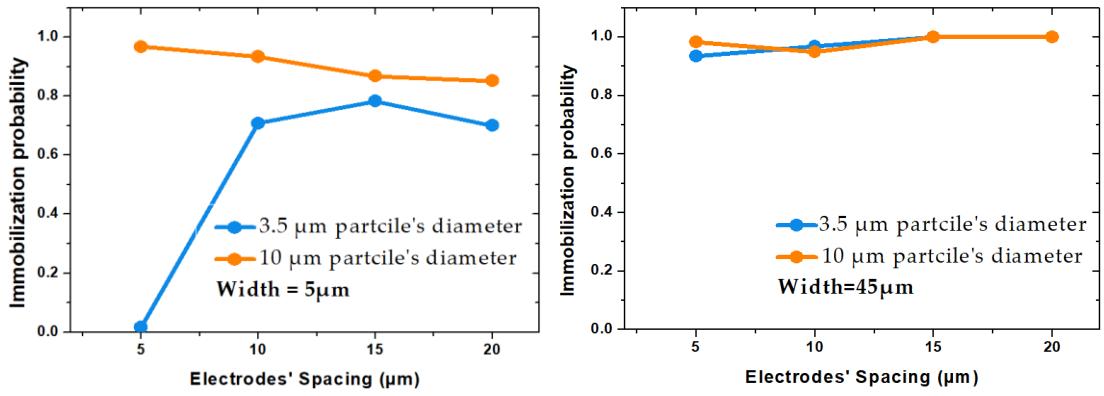

(c) (d)

Figure 2.12. Impact of non-uniform IDEs ($S \neq W$) on IP under the same voltage, frequency and fluid velocity: (a and b) IP variations for changing widths at fixed spacings of 5 and 20 μm; (c and d) IP variations for various spacings at fixed widths of 5 and 20 μm. In these simulations, 10 and 3.5 μm-size particles were the targeted particles [122].

Figure 2.13 shows tracing predictions of various structures for submicron particles (0.5 μm). For these studies, different IDEs with optimal geometrical parameters were used. For these simulations, the electric potential maintained at 5V (CMOS compatible range), and the fluid velocity was reduced to 30 μm·s^{-1} [122].

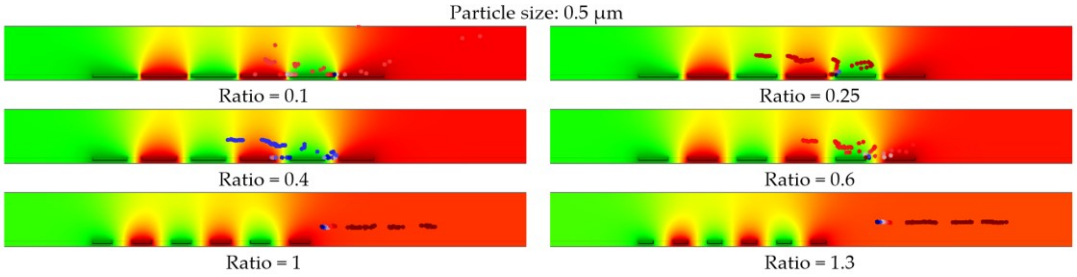

Figure 2.13. The trajectory of submicron particles (0.5) μm using the optimized IDE structures and flow velocity at constant voltage and flow velocity (5 V and 30 μm·s^{-1}, respectively) [122].

At reduced flow rates, similar tracing trends as micron-sized particles were observed for submicron-sized particles for lower-ratio structures (< 1). The decreased spacing to width ratios enhanced the tracing and trapping of submicron size particles [122]. However, using higher ratios, particles were repelled from the electrodes and released from the channel. Figure 2.14a shows the electric field (E) distribution over two consecutive fingers of the IDE structures at applied AC electric potential of 5 V and 10 MHz. It can be seen that, for IDEs 1 to 4, the intensity of the E field declines as the S/W ratio increases, whereas for the structures with constant spacing, IDEs 4 to 6, the E field intensity remained almost unvaried. Figure 2.14b demonstrates the EFG

gradient distribution with the distance from the electrode surface. For the lowest ratios, the EFG is stronger and decreases as the dimension ratio increases.

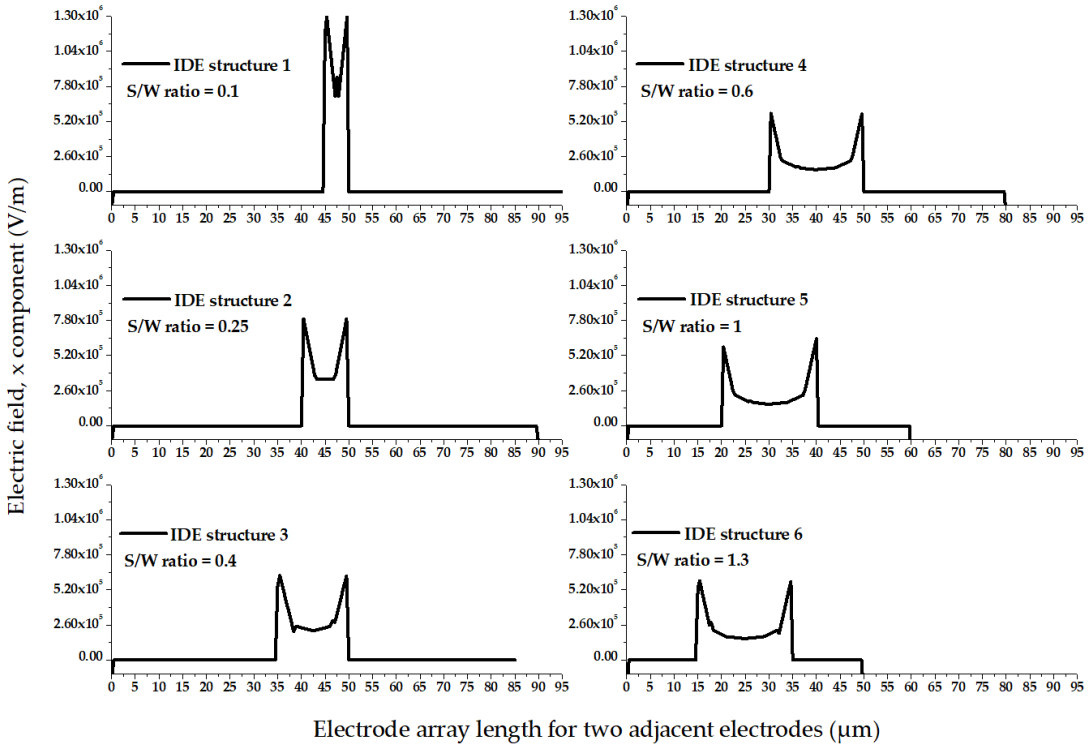

(a)

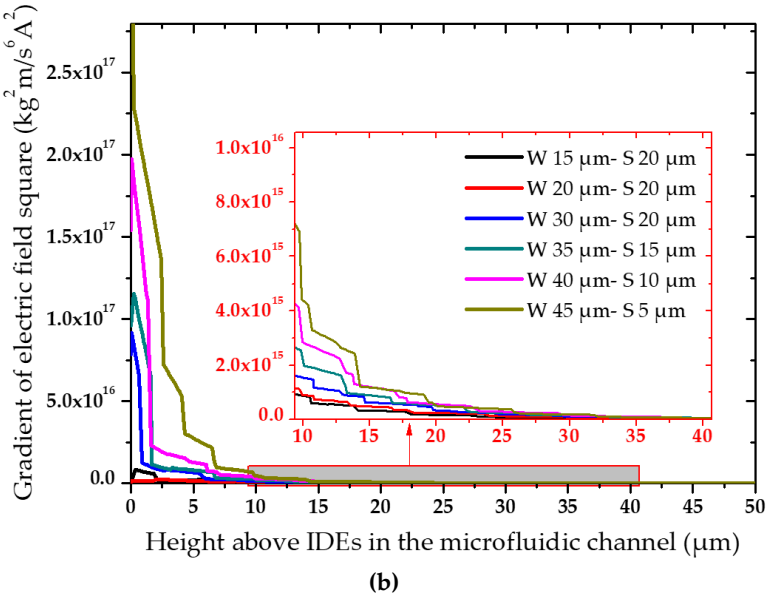

(b)

Figure 2.14. Electric field and electric field gradient distribution: (a) EF distribution above two adjacent fingers of the optimized IDEs; (b) EFG distribution with the distance from the IDEs surface.

It can be concluded that smaller sizes of spacing aids in higher electric field intensities. However, simulation results showed that IDE 5 and 6 with 1 and 1.3 ratios

were unsuitable for trapping submicron particles (see Figure 2.13). It is assumed that for the structures with the same spacing (IDEs 4,5 and 6), bigger electrode widths (e.g., design 4) positively impact particle immobilization. Therefore, it can be concluded that the pDEP force acting on the cells, which leads to the attraction of cells to the electrodes, is optimized for smaller spacing to width ratios. Experimental confirmations and validations will be further discussed in chapter V [122].

2.4 Selected IDEs Geometries and Initial Prototype Fabrication

It was seen that for trapping micron size particles, IDEs were optimized for ratios below 2. In contrast, for the immobilization of submicron particles, the geometrical parameters of the IDEs were optimized for ratios below 1. Based on these systematic simulation studies, IDEs with geometrical ratios below two were selected and proposed for the initial fabrication prototype [122].

Table 2.2. Selected IDE geometries compatible with CMOS operating range [58,122]

IDE Structure	Structure 1	Structure 2	Structure 3	Structure 4	Structure 5	Structure 6
Electrode width (W)	45 (μm)	40 (μm)	35 (μm)	30 (μm)	15 (μm)	20 (μm)
Electrode spacing (S)	5 (μm)	10 (μm)	15 (μm)	20 (μm)	20 (μm)	20 (μm)
Ratio = S/W	0.1	0.25	0.4	0.6	1.3	1

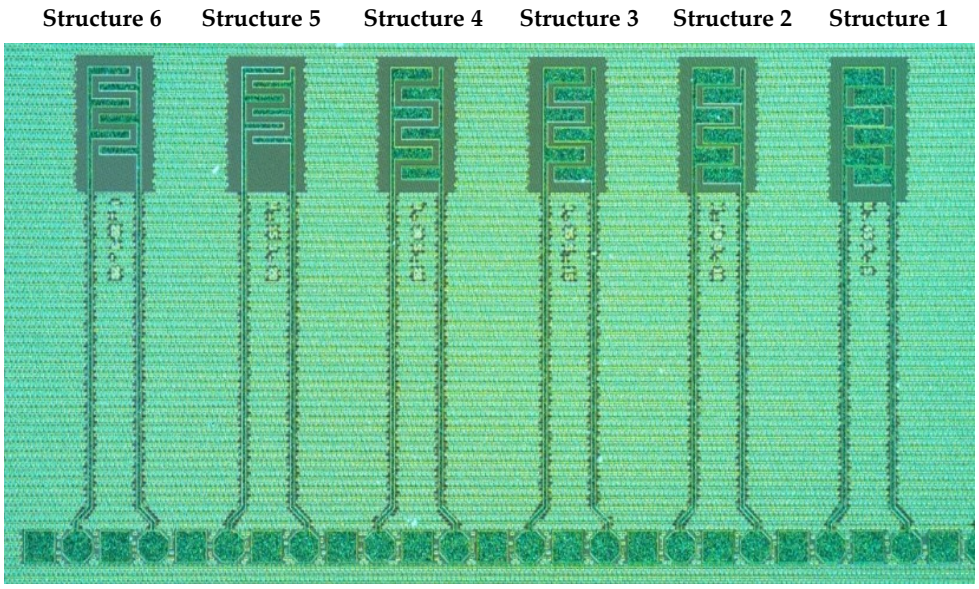

Figure 2.15. Initial IDEs prototype based on the optimized parameters achieved by FEM [122]**.**

For the experimental validation, six IDEs were aligned vertically in the microfluidic channel [122]. The geometrical specifications of these IDE structures are shown in Table 2.2, and the first electrode prototypes are shown in Figure 2.15.

2.5 Summary

In this chapter, a COMSOL model was produced to assess different effects and potencies on a particle's trapping force and assess the optimal configuration for the electrode geometry.

Simulation results showed that designing a better performance IDE was highly influenced by the optimum ratio of the electrode's spacing to width. Furthermore, the medium's flow rate inside the microfluidic channel impacted the particles' movement behavior inside the electric field. The AC field values and dielectric properties of the cells and medium influenced the particle tracing and the dielectrophoretic behavior of the particles. These are essential factors to consider for the immobilization of submicron and micron-size particles.

Systematic simulation studies for micron and submicron particle sizes showed that trapping probability decreases with increasing structure ratios, especially by particle size reduction. Moreover, the optimized IDE parameters for trapping submicron particles were related to IDE geometries with ratios below one. However, for trapping of micron size particles, the IDE was optimized for ratios below two. Based on these analyses, six different structures were selected and proposed for fabrication and validated by experimental measurements.

Chapter III

3 Sample-preparation Development

Once the prototype IDEs had been determined on the CMOS chip, the next step was integrating the CMOS with the microfluidic channel. The target process was to produce a monolithic CMOS LoC in which all the steps were compatible with the CMOS line process. From the research done in chapter 3, optimal electrodes were selected to evaluate their potential and fabricated on the topmost metal layer of the CMOS in a way that they embedded on the bottom of the microfluidic channel. The sample-preparation development to be used for the final application was covered in three parts:

1. Lab-on-a-Chip Technology and Integration: Development of the chip components that would form the final sample-preparation chip development. The sample-preparation device was the first part to be devolved, based on the optimized IDE design introduced in chapter 3.
2. System preparation: Design and fabricate the chip holder and prepare the experiment's platform to determine the best sample-preparation system.
3. Material under test (MUT) preparation: Different cell suspensions with live and dead yeast cells and various buffer solutions were prepared to validate the device's capability for dielectrophoretic manipulation and separation applications.

Parts of the contents of this chapter have been published in [58,122,125].

3.1 LoC Technology and Silicon Microfluidic Integration

3.1.1 Device overview

The LoC platform introduced in this work combines a microfluidic channel with high-performance CMOS electronics. The process flow according to the design of IDEs was performed by MPW (multi-project wave) service at IHP. The fabrication strategy used in integrating the microfluidic channel into the CMOS process was adapted from [126,127] and developed by the technology department of IHP. Based on this technique, isolated microfluidic and electrical interfaces can be achieved. The fabricated CMOS device was integrated with a silicon-based microfluidic channel, and the chip was packaged with transparent glass. The integrated glass wafer on top of the microfluidic channel provides simultaneous electrical and optical measurements. The combination of CMOS microfluidic channel technologies has been encouraging enough to merits cost-cutting and high throughput integration level, therewith making this method affirmative for biomedical demands. Tapping the potential of the system miniaturization, downsizing channels, and integrating sensors near the fluidic interface is possible, engenders a more sensitive LoC system [58].

3.1.2 Design and fabrication

To analyze biological suspension, CMOS IDE was combined with a microfluidic channel on a single chip. As mentioned earlier, the IDE fabrication was performed based on the standard 250 nm high-performance SiGe BiCMOS technology of IHP. This technology's back-end-of-line (BEOL) has five metal layers of aluminum/tungsten metallization with an interlayer dielectric made of silicon dioxide. The top two metallization layers (TM1 and TM2) are thicker than the other metallization layers. These layers were used to pattern the RF passive components of high-quality factors such as inductors, capacitors, resistors, transmission lines, etc. Interconnects within the circuit are fabricated on the lower metal layers. The electronic circuitry for data acquisition, signal processing, and read-out are combined with CMOS active devices (transistors). In this thesis, to trap and detect the cells using IDEs, these electrodes were fabricated on the topmost metal level (TM2) of the BEOL stack of the CMOS/BiCMOS process. The choice of electrode fabrication on one of the two top layers depends highly on biology aspects. For example, for immunosensors applications, due to the surface chemistry requirement for trapping biomolecules (like protein) on top of the topmost metal layer's passivation layer, the electrodes are fabricated on the TM1 layer [120].

On the contrary, for microfluidic applications to intensify the system's overall sensitivity, electrodes are fabricated on the topmost layer (TM2). This ensures the proximity of the sensor to the biological integration. The interaction of biological samples on top of the electrodes does not influence the transistor's operation. The BEOL stack of the process is shown in Figure 3.1.

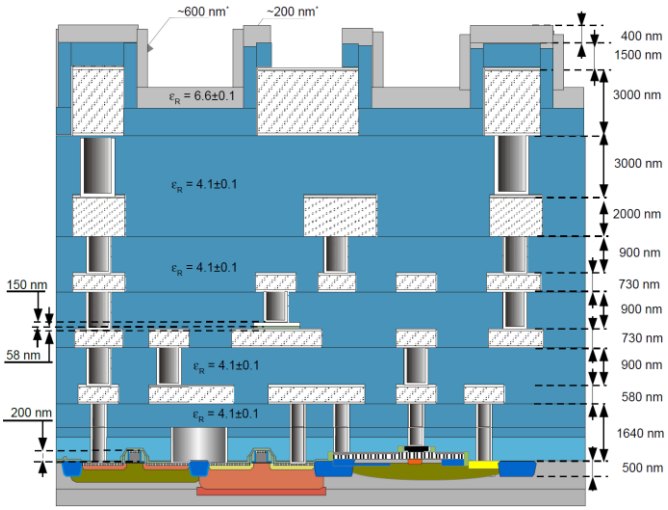

Figure 3.1. Cross-section schematic of IHP's CMOS/BiCMOS back-end-of-line stack, representing the SG25H1 CMOS/BiCMOS process with five metal layers.

This stack is comprised of five metal layers. The lower three metal layers are thinner than the TM2 and TM1 layers on top of the BEOL stack. The thickness of TM2 and TM1 is 3 and 2 μm, respectively, whereas the lower layers' thickness is 730 and 580 nm. The top two metal layers are less resistive. The integration technology of the CMOS IDE with a silicon microfluidic channel improves the functionality and precision by combing the fluidic solution and electrical components. This technology integrates CMOS circuitry with microfluidics as part of the 3-wafer-stack approach in a CMOS-compatible manner. Replacement of the relatively large-scale polymeric-based fluidic channel with miniaturized silicon microfluidics facilitates the possibility of bringing cells closer to the fringing EF created by the electrodes. Notably, fabrication reliability, reproducibility, and fabrication cost saving are the main benefit of this approach. One of the remarkable benefits of this technique is the separate interfaces for microfluidics and the electrical connections, enabling highly miniaturized LoC systems. This is shown in Figure 3.2, where the electrical contact pads are placed far from the electrode arrays covered by the microfluidic channel. This offers the opportunity of immobilizing, sensing, and detecting the particles on the same chip. The DEP technique's operational simplicity and low voltage requirement, and the small volume of samples for testing facilitate the LoC devices' portability even out of the non-laboratory conditions.

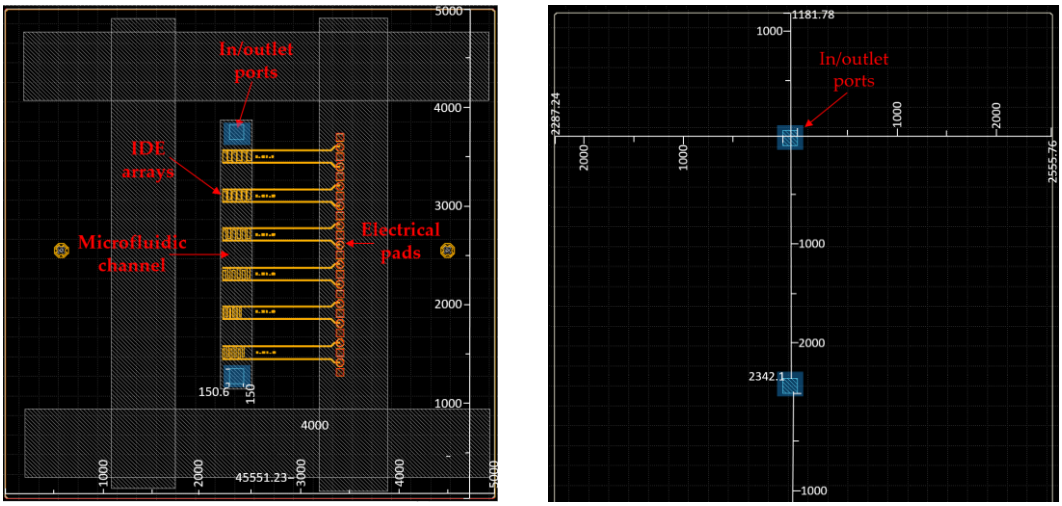

(a) (b)

Figure 3.2. The layout of a CMOS integrated LoC device: (a) Front side; and (b) Backside.

State-of-the-art of this CMOS integrated silicon-based microfluidic lab-on-a-chip depends on the compatibility of IHP's CMOS and the hetero-integration technology of the microfluidic device [58]. CMOS technology compatibility can be interpreted in two aspects. One is choosing new materials to prevent contamination issues during fabrication. The other one is the pilot package line, i.e., the CMOS line packaging tool. The fabrication of CMOS-based microfluidics is free of contamination problems of the CMOS process line. Fabrication of electrodes, microfluidic channels (and potential circuitry, which will be the outlook of this thesis) on a single chip is based on the hetero-integrated CMOS technology. This silicon microfluidic channel is a reliable substitute for the polymeric-based microfluidic channel that suffers from integrating the electrodes and circuitry on the same chip.

200 mm wafer bonding technologies did the integration of CMOS circuitry, silicon channels, and glass wafers. First, the fabricated CMOS wafer and the channel wafer were bonded by plasma-activated oxide-oxide fusion bonding. This process is subsequently followed by the adhesive bonding of a glass wafer to the back side of the channel wafer. Backside grinding was used for the arrangement of the channel height in the former step. Bonding was a crucial step in this process because high bonding strength increased the packaging yield. The increased bonding strength was achieved by applying surface roughness optimization on the CMOS wafer. Due to the low bond strength, the wafer stack might undergo stress forces from grinding, which could have damaged the wafer and packaging. Atomic Force Microscopy (AFM) and scanning auger microscopy (SAM) characterization techniques provided a good understanding of bonding before and after bonding steps of packaging flow [127]. Before fusion bonding, to achieve the best roughness conditions, the deposited

thick oxide layer's effect on top of the last metallization layer was optimized by the oxide layer's type and thickness. The surface micro-roughness was decreased from 1.79 nm to below 1 nm over 20 x 20 μm^2 area through these optimizations. This step was followed by a short Chemical Mechanical Polishing (CMP) touch-up to lower the surface roughness further and decrease the oxide micro-roughness by around 0.35 nm [127]. This CMP touch-up techniques increased the bonding yield up to 99% of the total 200 mm wafer surface area compared to the standard flat terminated CMOS of the IHP technology with a bonding yield of around 60% of the overall 200 mm wafer area, which dropped down even further (to 10%) after grinding step which was applied for adjusting the microfluidic channel height [127].

Due to the wafers' partial bonding, the loosely bonded wafer parts were flying around and hitting back on the surface with high velocity during grinding, which could damage and break the neighboring parts and structures. In contrast, for wafers with touch-up optimization and 99% bonding yield, the post-grinding yield was increased over 90% compared to the 10% post-grinding for the wafer stack without surface optimization [127]. The plasma-activated bonding was applied at 300 °C and low power (1.5 kN) bonding force. On the one hand, this bonding technique offered bonding at low temperatures to catch up with CMOS thermal budget. On the other hand, it provided high-quality and leakage-free bonding interfaces. After achieving a high-quality bonding (with alignment accuracy less than 1 μm) of the CMOS wafer and the channel wafer and grinding step to arrange the channel the height, the second wafer bonding was applied. The glass wafer's surface was covered by an adhesive layer of 30 μm thickness using spin coating and was bonded to the backside of the engineered channel wafer [126]. After channel encapsulation with the glass wafer dicing of the chip (by 5 x 5 mm^2), the CMOS integrated microfluidic LoC device's fabrication was done.

Figure 3.3 briefly illustrates the entire process flow for microfluidic devices [58]. The 8-inch wafer with the CMOS devices, including the BEOL electrodes, was processed on 200 mm Si substrates. In the subsequent phase, the inlet and outlet were opened from the wafer's back side by localized backside etching, Figure 3.3a. Another bare silicon substrate was used to structure the channel by etching, Figure 3.3b. Using a low-temperature plasma activated fusion bonding at 300 °C, the silicon channel wafer and the CMOS wafer were bonded together from their front sides, Figure 6c (1). After this step, the channel's height was adjusted by grinding the backside of the microfluidic channel. Finally, for encapsulating the microfluidic channel, a glass wafer was adhesively bonded to the channel wafer's backside at 200 °C (see Figure 3.3c) [126]. The transparency of the top layer enables simultaneous optical investigation and electrical characterizations.

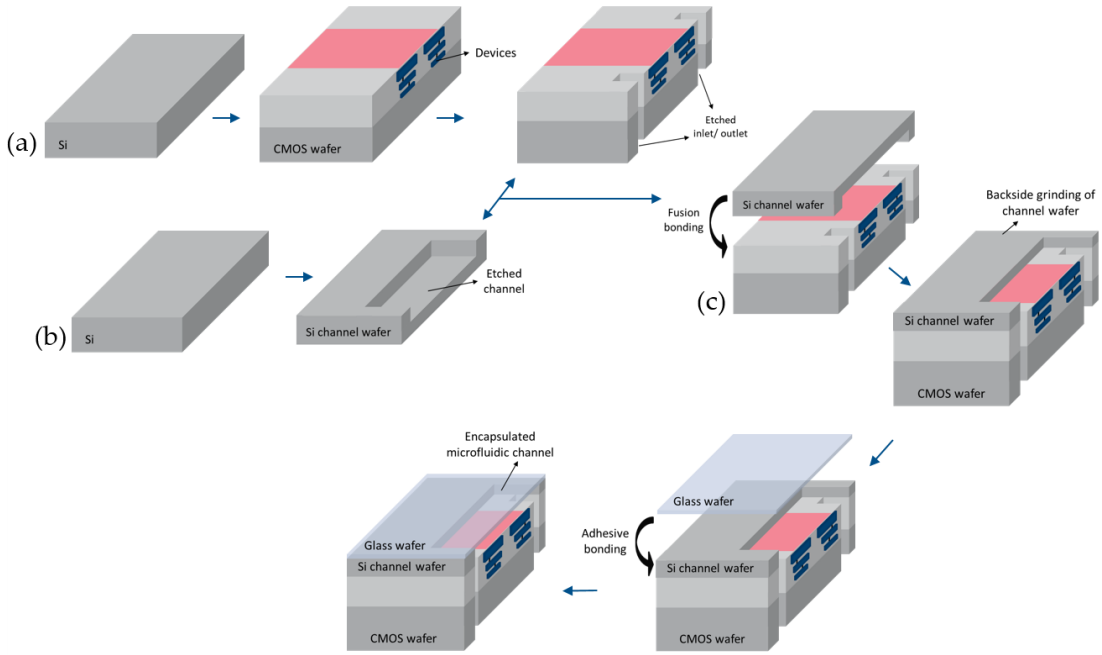

Figure 3.3. Schematic cross-sectional image of the silicon-based CMOS integrated microfluidics LoC based on three-wafer stack approach [126,127]**: (a) Fabrication of CMOS (b) Microfluidic channel fabrication; (c) bonding process of three wafers** [58]**.**

The dimensions of the chip and the microfluidic channel are shown in Figure 3.4.

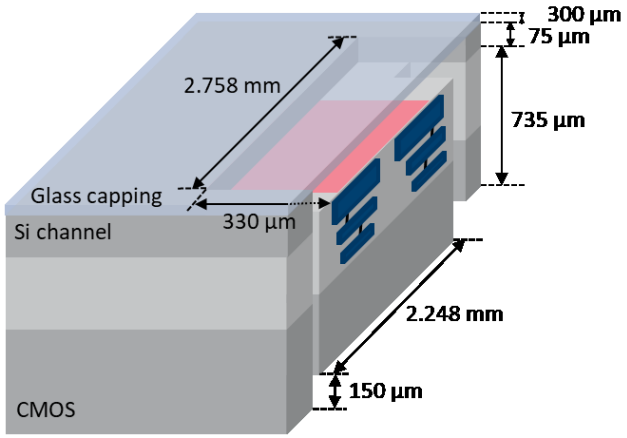

Figure 3.4. Approximate dimensions of the CMOS integrated microfluidic device.

Figure 3.5a,b shows the resulting packaged wafer and the diced device chips with a dimension of 5 × 5 mm^2, respectively.

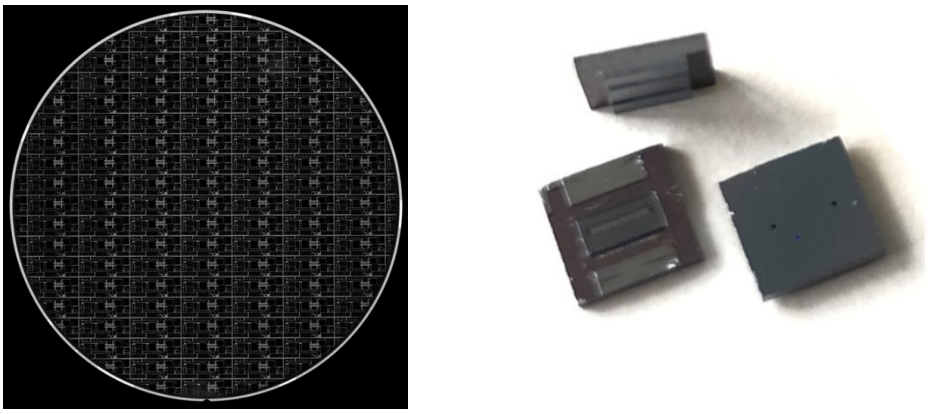

(a) (b)

Figure 3.5. CMOS integrated microfluidic LoC: (a) Resulting packaged CMOS integrated microfluidic device wafer [127]**; (b) 5 × 5 mm² diced devices** [58]**.**

Figure 3.6 illustrates the device chip. The standard compatible CMOS materials used to fabricate the IDEs are recognized for being long-term durable in CMOS-based products. The reliability issues of these materials used for biochip fabrication are required to be assessed in the future. Different IDEs were then developed to determine and verify the simulation results experimentally. For the CMOS integrated microfluidic channel prototype, as a consequence of design limitations for electrical contacts, the electrode structures were fabricated perpendicularly to the microfluidic channel [58].

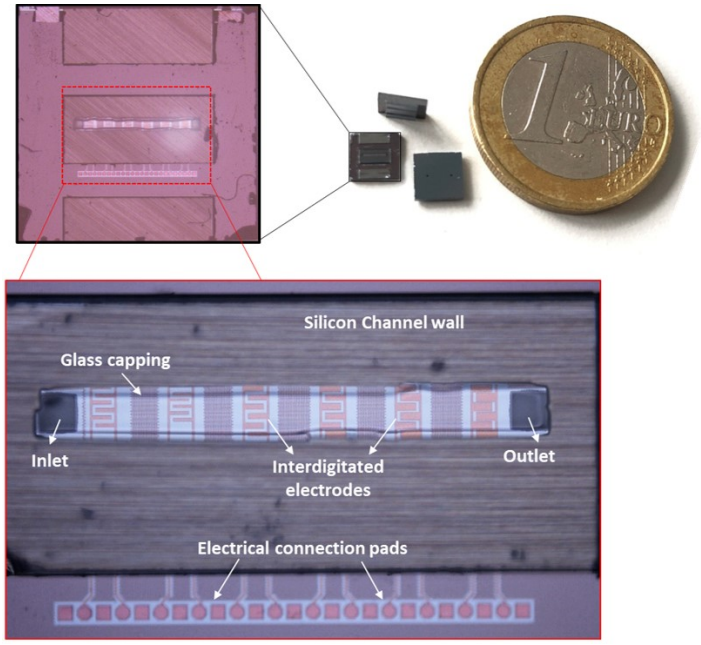

Figure 3.6. The 5 × 5 mm² diced CMOS integrated microfluidic LoC devices with the magnified view of the chip and IDEs in the microfluidic channel and contact pads [58]**.**

3.2 System Preparation

3.2.1 Macrofluidic equipment design and fabrication

To create an interface to inject the sample through the microfluidic channel and control the fluid flow, an external macrofluidic technology was employed. The fluidic manifold holds the device and assists various microfluidic steps. To this end, a chip-holder was designed (Figure 3.7a). This chip was fabricated using a commercial 3D printer (Keyence Agilista-3200W, Keyence Co., Osaka, Japan) (Figure 3.7b) and made of transparent rigid polymer (PMMA), interfacing the micro-device to the macroscale fluidic environment. A 5 × 5 mm² cavity (the same size as the chip) was formed in the manifold. From the CMOS chip's bottom side, the square-shaped inlet and outlet (150 × 150 μm) of the microfluidics were arranged directly on the manifold channels. To prevent leakage at the chip and manifold interface, two O-rings (with an inner diameter of 0.5 mm) were used to secure the fluidic connections between the manifold and the chip. Using two screws, the chip was fastened between the fluidic manifold cap and base. The thread connectors, screwed into the inlet/outlet ports of the manifold, were used to provide external tubing connections [58].

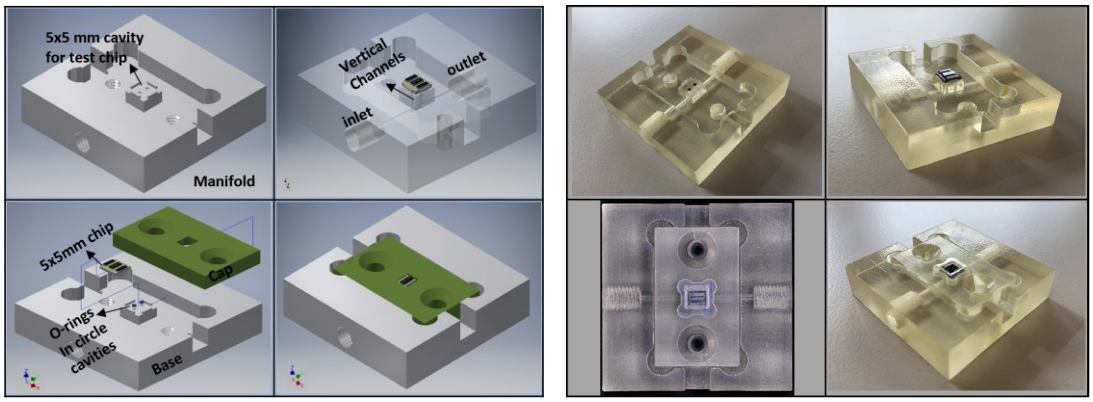

Figure 3.7. Developed manifold technology using 3D printing to hold the microfluidic chip and to interface it with macroscale setup: (a) 3D design of the manifold; (b) Manifold made of PMMA and fabricated using 3D printing including a test chip [58].

3.2.2 DEP measurement system

Figure 3.8 presents the measurement setup, which comprised of an AC signal generator (Agilent-33220A, Agilent Technologies/Keysight Technologies, Santa Clara, CA, USA) for fringing electric field generation between the adjacent electrode fingers, a programmable syringe pump (NEMESYS, CETONI GmbH, Korbußen, Germany) for sample injection through the microfluidic channel, and an upright tabletop microscope

(Nikon Eclipse-LV100ND, Nikon GmbH, Tokyo, Japan) supplied with a CCD camera (Nikon-DS-Fi2, Nikon GmbH, Tokyo, Japan) coupled to a computer for simultaneous optical investigations and analyzation of the captured images and videos [58]. To access conductive pads and provide the electric field using an external source, two micro positioners (manipulators) were used. The probe needles were accurately positioned and aligned to touch down on the contact pads.

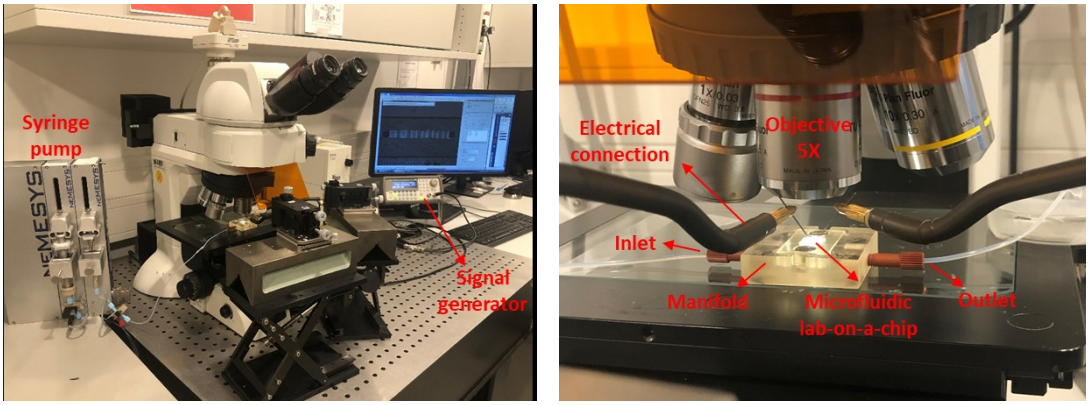

Figure 3.8. DEP characterization experimental setup: (a) overall view of the DEP equipment; (b) device under test with electrical connections under the objective [58].

3.2.3 Experimental protocol for DEP

By applying the AC signal (electric field) to the IDEs, the DEP characterization and manipulation of yeast cells in the microfluidic channel were attained. Six interdigitated electrodes with different dimensional ratios (spacing to width ratios) were used individually to perform DEP characterization experiments on yeast cells. The electric field was supplied by the signal generator. The field frequency was altered between 1 kHz to 20 MHz (limited by the AC generator with the highest output voltage of 20 V). The cell suspension was loaded into the chip using a syringe pump. 50 μm s^{-1} flow rate was used to drive the sample suspension through the pipes. The flow was stopped when the cells reached the channel's region, and when the cells were settled (after 15 s), the flow rate was then increased to 1 μm s^{-1}. The flow rate was then kept constant during the DEP characterization. Employing a high fluid flow rate through the channel discarded the cells from the channel rather than entrapment and immobilization of the electrodes. Switching off the AC signal after cell entrapment led to desorption of the entire immobilized cells from the electrodes and elution of the cells from the channel. For various voltages, frequencies, and flow rates, the trajectory of the cells was observed under the microscope. A CCD camera with a 5× objective was used during experiments to acquire and record images and videos

of the microfluidic channel. As an initial input signal parameter, a 1 MHz AC signal with 20 Vpp (peak-to-peak), where pDEP was expected, was applied [58].

3.3 Material Under Test Preparation

3.3.1 Cell

Yeast cells (Saccharomyces cerevisiae RXII, Commercial fresh baker's yeast) were used as the model particles for DEP investigations. Live yeasts were suspended in a 40 mL aqueous medium at a concentration of 1.5 mg $mL^{-1.}$ This suspension solution was incubated at room temperature for 15 min and was stirred every 5 min [58,125]. Dead cells achieved by heat-killing live-cell suspension with the same concentration, using a dry bath block (AccuBlock Mini-Compact Dry Bath, Labnet International, Inc., Edison, NJ, USA), at 100 °C for 30 min [125]. These live and dead suspensions were applied separately for characterization and manipulation experiments and were mixed for separation experiments. The average diameters of the live and dead cells were measured as 7 to 8 µm and 6 to 7 µm, respectively. Figure 3.9a presents yeast cells under 100× objective and bright field mode and the yeast two-shell model used for numerical calculations and simulations.

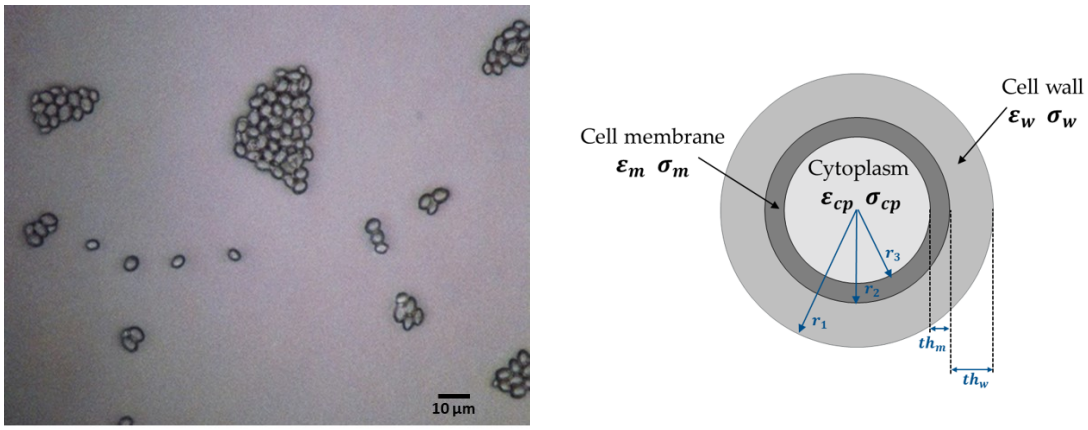

(a) Yeast cells (BF-100×) **(b) Yeast two-shell model**

Figure 3.9. Yeast cell: (a) image of the yeast cell in the bright field under 100X objective; (b) Two-shell model is simplified to a sphere.

As described schematically in Figure 3.9b, a cell was modeled as a dielectric sphere, in which the inner cell (cytoplasm) is covered by two layers, cell membrane and cell wall, respectively. Electrical properties of the viable and non-viable yeast were taken from [128] and presented in Table 2.1. Yeast cells are exposed to some

modifications when they experience heat shock. Such changes could reduce size and alternate to the cell's dielectric properties, as shown in Table 3.1. As a result of the heat shock, the intercellular water of the yeast cell is decreased, and the cell experiences water stress. Due to an impaired membrane, dead cells lose their viability. This results in the cell membrane's wrinkling and downsizing in the cell diameter, which is linked to the shrinkage of the whole yeast cell [129–131]. Their membrane conductivity is expanded while their cytoplasmic conductivity is diminished [58].

Table 3.1. Viable and non-viable yeast cell dielectric properties [128]

Cell	Permittivity			Conductivity (S/m)			Radius	Thickness	
Yeast	ε_{cp}[1]	ε_{m}[2]	ε_{w}[3]	σ_{cp}[1]	σ_{m}[2]	σ_{w}[3]	r_1	th_m[2]	th_w[3]
Live yeast cell	50	6	60	0.3	0.25×10^{-6}	0.024	3.5 μm	8 nm	0.22 μm
Dead yeast cell	50	6	60	0.012	1.6×10^{-4}	0.0025	3 μm		

[1] Cytoplasm. [2] Cell membrane. [3] Cell wall.

3.3.2 Cellular suspensions

Yeast cells were diluted in four various medium solutions with different conductivities. These sample media were used to compare the cell's DEP responses. The sample stock solutions were further diluted for other experiments such as separation, viability, and cell density measurements. The conductivity of the mediums was arranged in a way that covers different conductivities ranges (ranging from 10^{-4} to 1) for DEP investigations. Yeast cells were estimated to be robust enough to survive any osmotic stress resulting from the non-physiological media used [125].

Deionized water (DIW) was used for its availability and low conductivity, making it ideal for efficient measurement and broad frequency range under pDEP. Furthermore, the risk of Joule heating during the measurement is reduced for this solution. Tap water was chosen for its availability. Besides, due to the presence of ions in the tap water, the impact of ionic concentration on the DEP characterization compared to DIW could be investigated. Potassium chloride (KCL) was used because it offers the possibility to control and change the conductivity, which is a function of the solution's concentration. The preparation of different concentrations for different conductivity values is possible. 20 mM was chosen because it yields a conductivity value in the desired order of magnitude (10^{-1}). The solution was prepared by dissolving 149.10 mg of KCl (Supelco, Merck KGaA, Darmstadt, Germany) in 100 mL of deionized water. Phosphate-buffered saline (PBS) is a typical cell buffer used to maintain the osmolality and pH (which is generally 7.4) of cells in solution. It was used as a high conductivity medium that simulates physiological fluids. The ionic concentration and osmolality of this solution usually match those of the human body.

To obtain a 0.1 M solution, the PBS solution was prepared by dissolving a 1.66 gr of the powder (Sigma-Aldrich, Merck KGaA, Darmstadt, Germany) in 100 mL of deionized water. A lower conductive PBS buffer was prepared via diluting 1 mL of the stock solution in 25 mL DIW. The conductivity of the final diluted PBS (D-PBS) suspension was measured and reported in Table 3.2.

To differentiate between live and heat-killed yeast cells and to better visualize the separation experiment under the microscope, the dead yeasts were stained with methylene blue (MB) dye based on the following recipe:

1) 0.01 gr MB dye (Sigma-Aldrich, Merck KGaA, Darmstadt, Germany) + 10 mL DI water + 2 gr sodium citrate (Sigma-Aldrich, Merck KgaA, Darmstadt, Germany).
2) Filtering the prepared solution through filter paper.
3) Adding DI water until 100 mL is reached.
4) Mixing diluted MB solution with a fraction of the diluted cell suspension with ratios of 2:3 and keeping it for 15 minutes before running the experiment or viability test.

After preparing sample solutions with desired dilutions, the conductivity of the mediums was measured by a conductivity meter (Accumet AET30 Conductivity Tester, Thermo Fisher Scientific, Inc., Waltham, MA, USA) at room temperature with 10 μS – 0.10 mS resolution sensitivity [125]. For this, the solutions were filled into 6 mL tubes, and the conductivity meter tip, which was comprised of a pair of electrodes, was soaked in the tube for few seconds until the displayed value got stable. Table 3.2 presents the measured conductivity values and literature reported permittivity values of the mentioned media solutions.

Table 3.2. Fluidic media and their respective measured conductivity values

Medium solution	Conductivity (S/m) (empirical)	Permittivity (Literature)
DIW	0.0002	78
Tap water	0.08	78
KCL (20 mM)	0.2	78
PBS (0.1 M)	1.39	78
D-PBS	0.1566	78
MB dye	0.99	-

3.3.3 Cellular density estimation

A hemocytometer (BRAND® counting chamber BLAUBRAND® Neubauer improved, BRAND GMBH + CO KG, Germany) was utilized to estimate the density of the cells by counting the cells per volume concentration unit (cells/ mL). The stock

suspension solutions were made with a concentration of 1.5 mg mL^{-1} (60 mg of yeast suspending in 40 ml of suspending medium) in each of the buffer media. The cellular density of the stock solutions, for both live and dead, were estimated to be in the average range of 1.45×10^7 cells mL^{-1}. 1:10 diluted samples were prepared by adding 1 mL of each of the suspensions to 9 mL of its respective stock medium solution. In separation experiments, the 1:10 dead cell suspensions were stained with MB dye in a 2:3 ratio before mixed with live ones. So, 2 mL of the diluted dead cell solution was mixed with 1 mL of MB. To obtain a live and dead mixture with roughly equal live and dead cell density, 1 mL of diluted live samples were then re-suspended in 1 mL of their respective medium/buffer solutions. After that, the prepared viable and non-viable samples were mixed in a 1:1 ratio. The mixture's cellular density was approximately in the average range of 1.3×10^5 cells mL^{-1} [125]. Table 3.3 below shows the measured conductivity variations for both live and dead cells suspended in DIW before and after staining.

Table 3.3. Measured conductivity values for unstained and stained cell mixture in DIW

MUT[1]	Unstained 1:1 cell mixture	Stained 1:1 cell mixture
Conductivity (S/m) (empirical)	0.0023	0.128

[1] Material under test

As it is clear, the stained cell mixture increases the conductivity of the cell mixture. Therefore, before separation experiments, DEP characterization was first performed separately on stained live and dead cells compared with the result obtained from both unstained cell types. The differences were then considered for separation experiment analyses on stained cell mixture.

3.3.4 Viability estimation assessment

The cell mixture's viability was estimated through optical microscope observation. The heat-killed cells were stained to turn blue-color cytoplasm [125]. Figure 3.10 shows an example of the mixture of viable and non-viable solutions in a 1:1 ratio under a 10× objective within a counting chamber (hemocytometer). The blue spheres represent heat-killed (dead cells), and white ones define live cells. The measured viability for this sample was around 54%.

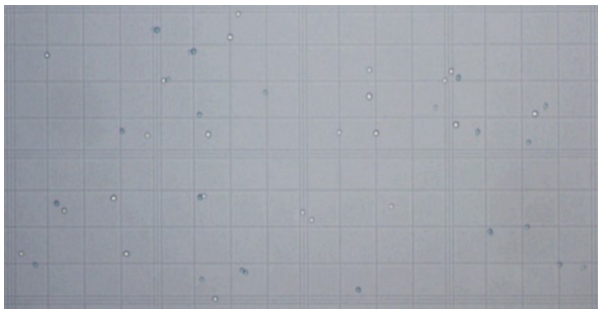

Figure 3.10. A mixture of 1:1 live and blue-dyed dead yeast solution in a hemocytometer with around 54% viability.

3.4 Summary

In this chapter, the development of the sample preparation system was discussed in detail. The different aspects of the test chip's preparation and development, measurement system, and material under test were explored.

The hetero-integrated CMOS technology allowed the fabrication of the CMOS device along with the optimized electrode designs and the microfluidic channel on top of the BEOL stack as a monolithic device. The fabrication of the silicon microfluidic channel and IDEs were compatible with the CMOS process line and performed based on the standard 250 nm high-performance SiGe CMOS/BiCMOS technology of IHP.

A chip-holder was designed to interface the microdevice with the macroscale fluidic system and provided a more accessible DEP characterization platform. A programmable syringe pump was utilized to control the fluid flow through the channel, and a function generator was used to provide an inhomogeneous AC field through the microfluidic channel. An upright microscope was used to capture images and videos during the DEP process.

To test the device performance, viable and non-viable yeasts were used as model cells. Dead cells were achieved by heat-killing the live cells at 100°C for 30 min. The cell suspensions with similar cell concentrations were prepared by diluting the cells in various media like DIW, TW, KCL, and PBS. The choice of media was made in such a way as to cover various conductivity ranges (from 10^{-4} to 1). The functionality and validation of the chip are covered in the following chapter.

Chapter IV

4 Dielectrophoretic Characterization

As the LoC device and sample preparation system were developed, the various sub-components were tested to ensure they performed as intended and allowed the complete system to be validated. Once the LoC platform and measurement system's functionality were confirmed through various test steps, DEP characterization was introduced in the experiments. This section gives an overview of the live and dead cells' characterization suspended in five different suspending carrier liquids. The first section describes the dielectrophoretic (DEP) characterization and manipulation of live and dead yeast cells and compares the experimental results with simulation assumptions. The second section discusses the functionality of this CMOS integrated microfluidic platform for separation applications. This section, as well as the previous section, compares the experimental data with simulation results. Some parts of this chapter have been published in [58,125].

4.1 Dielectrophoretic Manipulation of Live and Dead Yeast Cells

Manipulation of cells suspended in a medium of different characteristics can be achieved when cells become electrically polarized as exposed to an electric field. As the result of the interactions between the non-uniform electric field and the induced polarization, a DEP force acts on the cells, which is strongly dependent on the

dielectric properties of the cell and suspending medium, the angular frequency of the applied electric field, and spatial configuration of the field [1]. In this part, the impact of field frequency, dielectric properties of the cells and mediums, geometrical parameters of the IDEs, and electric potential on trapping and immobilization of the cells have been studied thoroughly. Figure 4.1 shows experimental and simulation manipulation examples.

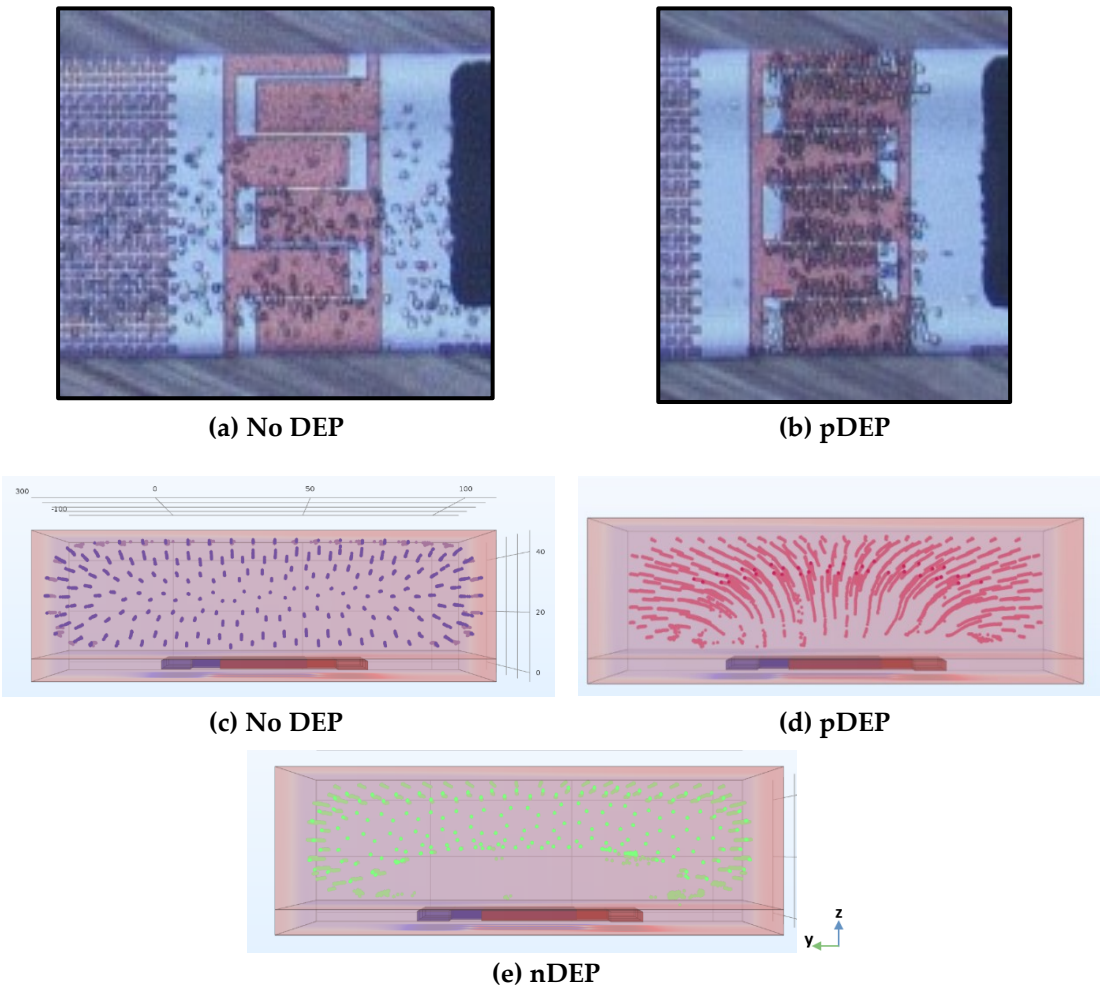

Figure 4.1. Cell manipulation with the microfluidic channel; (a) shows the cell trajectory from inlet to outlet (from left to right) when there was no DEP and cells pass over the electrode, whereas, (b) in the presence of pDEP, cells trapped [58]**; (c-e) are the 3D simulation (perspective view from the outlet side) for No DEP, pDEP, and nDEP; (c) normal trajectory of the cells without being influence by the DEP force, while (d) cells experiencing attractive force and pushed to the IDE region; (e) cells undergoing repulsive force and getting elevated over electrodes.**

Figure 4.1a shows the cell trajectory from the top view when DEP was zero, and cells were not influenced by any effects. The perspective view of the 3D simulation (Figure 4.1c) from the outlet side provides a clear picture of cells' normal trajectory. Cell entrapment (see Figure 4.1b) occurs when pDEP acts on cells. The translational

motion induced by the pDEP and nDEP is clearly shown by 3D simulations in Figure 4.1d (where cells flowing through the channel experiencing attractive force and get pushed to the IDE region) and Figure 4.1e (cells experiencing repulsive force and get elevated over the IDEs and repelled from them.), respectively.

For manipulation experiments, the DEP behavior of live and dead yeast was derived numerically from five different suspending solutions mentioned in chapter 4 and studied empirically.

4.1.1 Finite element simulations

4.1.1.1 CM factor calculation

Figure 4.2 illustrates the CM factor's ovulation with the frequency of the applied electric field for live and dead yeasts with typical parameters [128] in different conductivity fluidic carriers (DIW, Tap-water, KCL, PBS, and D-PBS). Once the conductivity of carrier fluids was measured, the cells' DEP spectrum was determined using numerical simulations. The f_{CM}, was numerically calculated for both live and dead yeast cells suspended in five various medias over a wide frequency spectrum, using myDEP software [132], in reference to the two-shell model [133] where cells are presumed to possess two concentric layers of different dielectric and electric properties. Variation of the imposed field frequency to the IDEs results in the generation of DEP force in two reverse directions, which results in pDEP and nDEP. The shift from the pDEP (top half) to nDEP (bottom half) and vice versa is called crossover frequency. At this specific frequency, the intrinsic properties of cells can be determined. For the frequency ranges lower than crossover frequency (fc), $Re[f_{CM}]$ was positive, while for higher frequencies $Re[f_{CM}]$ was negative. As shown in Figure 4.2a, for live cells suspended in DIW, the real part of the CM factor was defined between 0.9 and −0.13. For dead cells this value was bounded between 0.82 and −0.13. For sample suspension in DIW, crossover frequency was calculated at around 65.4 MHz for live yeast and 2.5 MHz for dead yeast. At lower frequencies than fc the pDEP was acting on both cell types. For live cell suspension in tap-water (Figure 4.2b) f_{CM} was limited between 0.28 and -0.47. The f_{CM} of dead cells was completely under nDEP. The same trend as tap-water can be seen for the KCL solution (Figure 4.2c) for dead and live cells. The maximum value of the f_{CM} for nDEP was around -0.49 for both tap-water and KCL medias while for pDEP was 0.28 for tap-water and 0.3 for KCL. This denotes that forces generated by pDEP are weaker compared to nDEP forces. For KCL compared with the tap-water, the pDEP spectrum was restricted to smaller frequency range and the maximum value of CM factor was lesser. Figure 4.2d, shows the f_{CM} for the sample suspension with highest conductivity (PBS, 0.1M) where $Re[f_{CM}]$ for both live and dead cells were limited to nDEP for all frequencies.

Nevertheless for live-cell suspension in PBS a pDEP spectrum was expected over a wider frequency range compared to KCL. For this cell suspension $Re[f_{CM}]$ was bounded between 0.1 and -0.48 [58,125].

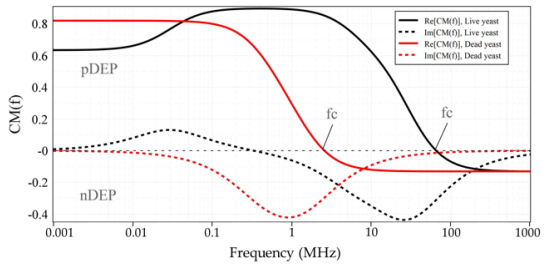

(a) Cell suspension in DIW

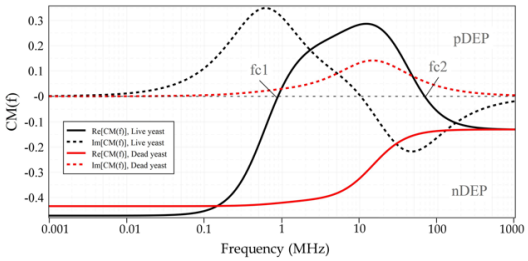

(b) Cell suspension in Tap-water

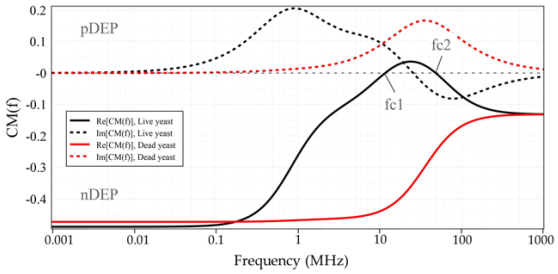

(c) Cell suspension in KCL

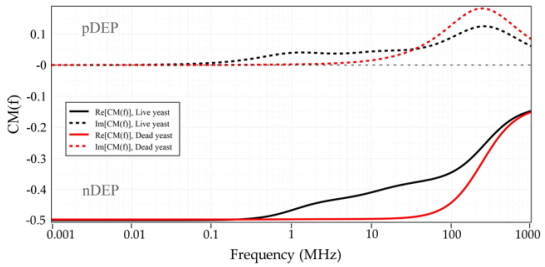

(d) Cell suspension in PBS

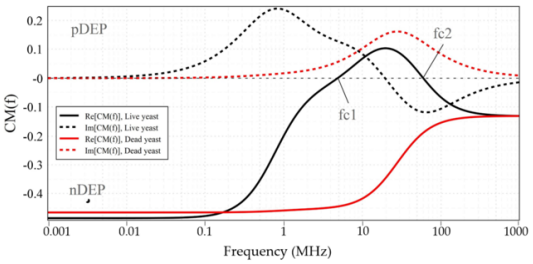

(e) Cell suspension in D-PBS

Figure 4.2. Numerical calculation of CM factor for live and dead yeast cell suspensions in: (a) DIW; (b) Tap-water; (c) KCl; (d) PBS; (e) D-PBS as a function of frequency. The two-shell model was used for these calculations. Yeast parameters are listed in Table 3.1 [125].

These calculations illustrate that the evolution of the pDEP disappears in high conductivity buffers. In other words, the higher the conductance of the buffer (carrier liquid), the less the dominancy of the pDEP becomes to immobilize cells. It is noteworthy to explain that the impact of carrier fluid's conductivity on the cell's permittivity is not notable. In contrast, the cell's conductivity is strongly dependent on the carrier fluid's properties [125]. This is due to the conductive double layer (Stern and diffuse layer) formed around the cell imposed on an inhomogeneous electric field [134].

4.1.1.2 COMSOL modeling for cell tracing

Based on the CM factor numerical determinations, the suitable frequency ranges for pDEP to trap cells were chosen and applied as an input for the COMSOL simulations. The same 2D model created for designing and optimizing the IDEs in COMSOL 5.5, chapter 3, was utilized to simulate the yeast tracing behavior [47]. This model was used to simulate the trajectory of the yeast cells through the microfluidic channel. Furthermore, the capability of the six IDEs for cell trapping was evaluated. The simulation assumptions were compared with the measurement results. Figure 4.3 shows the voltage contours (lines) imposed on the IDEs and the distribution of EF (arrows) over the IDEs in the channel. EF is intensified between the electrode fingers and maximized at the rectangular corners of the IDEs, which results in the inhomogeneous distribution of the electric field. As discussed earlier and shown in Figure 4.3, the magnitude of EF over the IDEs declines with the height over the IDEs towards the top of the microfluidic channel. Further simulation results will be discussed more in detail in each of the upcoming sections [58,125].

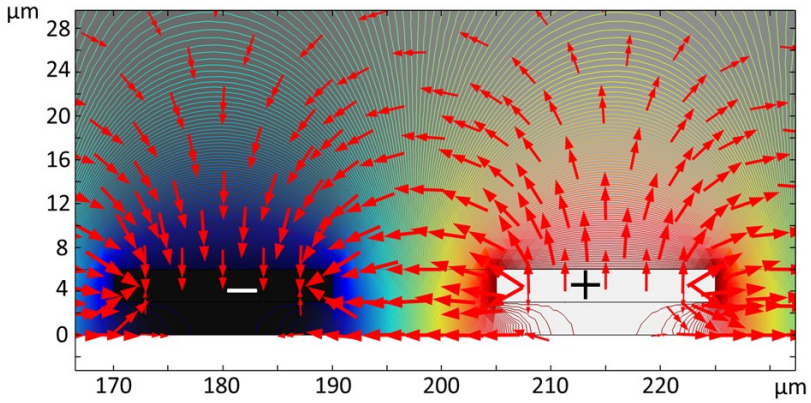

Figure 4.3. Electric potential (line contours) and EF distribution (red arrows) illustrations of two adjacent IDE fingers illustration using numerical simulation [58].

4.1.2 DEP characterization and manipulation

4.1.2.1 Impact of frequency

Using COMSOL modeling, the impact of signal frequency on both live and dead cells' trajectory was investigated for the same configuration and operating conditions utilized in experiments. These experiments were repeated for different yeast suspensions.

Figure 4.4 shows simulation examples of cell trajectory behavior experiencing positive and negative DEP when exposed to an inhomogeneous EF, respectively. The

maximum electric field gradient always points to the electrode edges, where for $Re[f_{CM}] > 0$ at frequencies where the cell's polarizability is higher than the medium, the pDEP causes yeast cells to be attracted to higher electric field locations and trapped at the edges of the IDEs, Figure 4.4a. In contrast, at frequencies, where yeast cells exhibit less polarizability than the medium and $Re[f_{CM}] < 0$, the nDEP repels cells from high intensity regions and pushes them upward against gravity [1], Figure 4.4b. The simulation results were reasonably consistent with the numerical predictions shown in Figure 4.2a.

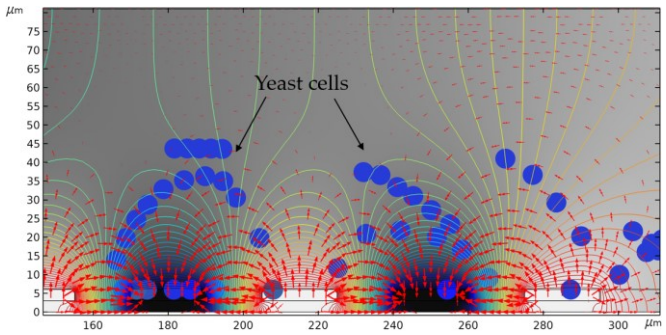

(a) pDEP

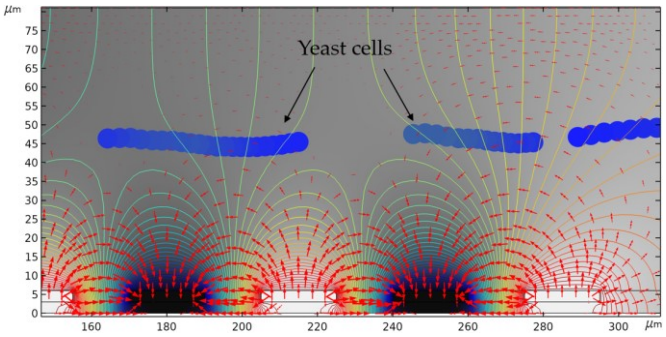

(b) nDEP

Figure 4.4. Simulation results of live cell trajectory behavior for: (a) pDEP and; (b) nDEP as a result of imposing an AC voltage of 20 Vpp at 1 MHz and 50 MHz, respectively. pDEP attracts the cells toward the high electric field locations, and nDEP repels the cells from these locations.

During experiments, the affective frequency ranges for pDEP were determined empirically by observing cell behavior when the given field frequency was changed to see whether cells moved towards the electrodes or away from them. To characterize the dielectrophoretic behavior of the viable and nonviable yeasts diluted in various solutions, 20 Vpp was applied at frequencies between 10 kHz to 20 MHz (maximum frequency allowed by the signed generator). According to the experimental results, the live and dead yeasts suspended in DIW exhibited both pDEP and nDEP behaviors. Figure 4.5 illustrates the empirically proven pDEP regime for both live and dead yeast suspension in DIW. Contrary to CM factor calculations (Figure 4.2a), the pDEP

spectrum for viable yeasts in DIW (the frequency band between the dotted black lines) was restricted between 100 kHz-12 MHz. The positive scope for nonviable yeasts in DIW media was between 20 kHz-2.3 MHz. The frequency at which the fc occurs (2.3 MHz) was in good agreement with the numerical simulation results. However, the frequency range at which cells experience enough DEP force to get trapped was between 300 kHz-10 MHz and 70 kHz-2.3 MHz for viable and non-viable cells, respectively.

Moreover, at specific frequencies, within this range, optimal trapping yield was achieved. Figure 4.5 demonstrates the lower trapping frequency regime in yellow than the green areas over which optimal trapping was obtained. The variation of trapping yield over the frequency spectrum was observable under the microscope. For the dead cells, the regime of pDEP occurred over a narrower frequency band and at lower frequencies than viable cells [125].

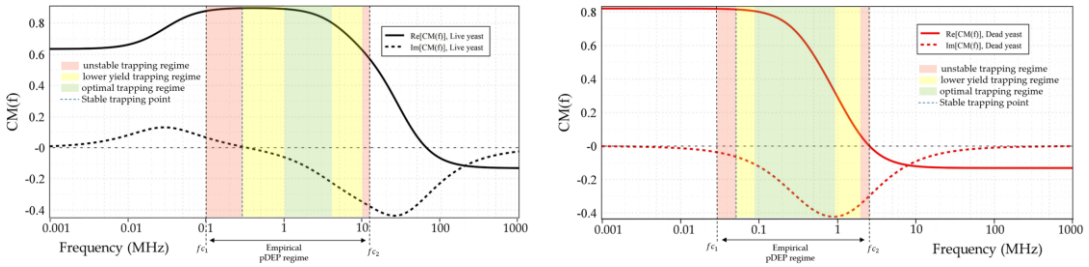

(a) Live cell suspension in DIW **(b) Dead cell suspension in DIW**

Figure 4.5. Numerical calculation predictions vs. empirically proven pDEP spectrum and fc for: (a) live and; (b) dead yeasts suspended in DIW. Colored frequency spectrums demonstrate cell trapping trends based upon optical observations [125].

The validity of such trapping behavior was examined via diluted live cells in DIW. Several images were taken to analyze and estimate the trapping rate (yield) for given frequencies at various measurement steps. Using ImageJ software, images were then analyzed. The cell coverage over the entire IDE area was then analyzed for each of the images. The immobilization percentage was estimated by calculating the ratio of the area covered by cells to the total area of the IDEs, as demonstrated in Figure 4.6a. Experimental analyses were performed at the frequency range of 10 kHz-20 MHz. For viable cells, the optimal frequency range was between 1–3 MHz. The image of the immobilized cells in Figure 4.6(b-g) illustrates the trapping trend based on frequency variation. The DEP force can only influence the cell trajectory for frequencies beyond 10 MHz (within the mentioned frequency regime) and below 300 kHz. Velocity reduction of cells arriving at the IDEs due to partial absorption to the electrode area followed by spontaneous desorption was observable. This can be correlated to insufficient pDEP force strength to trap the cells constantly at the electrodes. Upon

switching frequency, immobilization got stable between 300 kHz – 10 MHz, and optimal trapping, i.e., considerably more cells immobilized at the IDEs, achieved between 1 to 3 MHz [125].

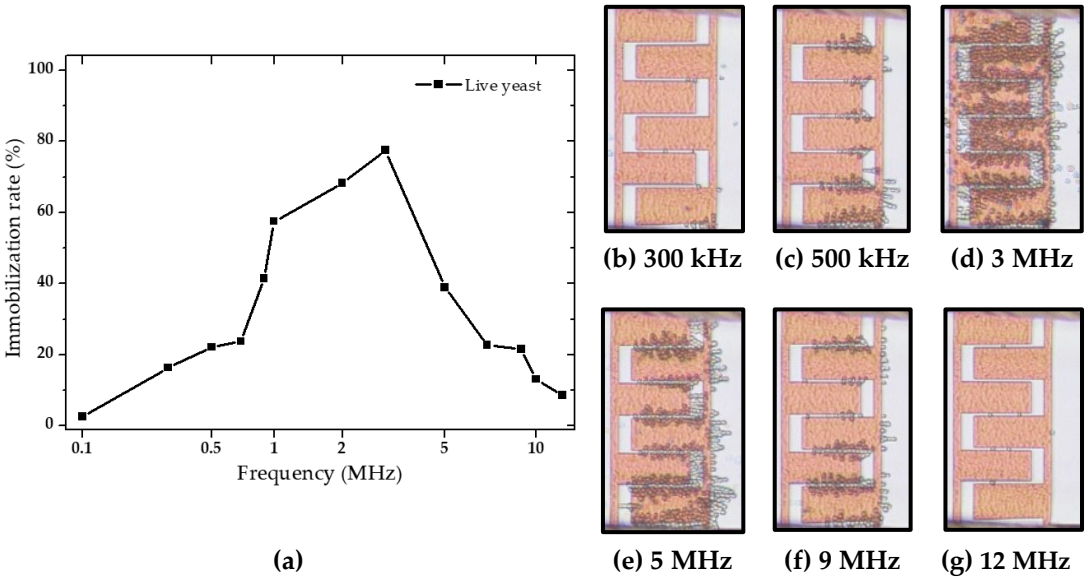

Figure 4.6. DEP behavior of viable yeasts in 1 min: (a) Immobilization rate approximation by frequency variation based on covered cell region at the IDEs; (b-e) illustrates trapping trends upon switching frequency [125]**.**

Keeping the trapping yield at an optimum rate, increasing or decreasing frequency up to crossover frequencies, results in entrapped cells' desorption. Figure 4.7a shows desorption rate estimation upon changing frequency to below 1 MHz and beyond 3 MHz. Using ImageJ, the desorption rate was calculated by applying the same procedure mentioned above. The varying frequency to 700 kHz and 9 MHz desorption rate was less than 30%. This rate increased drastically at higher frequencies (10 MHz ≤ f_o) due to nDEP and at lower frequencies ($f_o < 300$ kHz) due to weak pDEP. At frequencies between 700 - 900 kHz and between 7 - 9 MHz, the stability of entrapped cells diminished with the time passage, and entrapped cells gradually tend to desorb from the electrodes [58,125]. Reaching 12 MHz and 100 kHz, cells experience a repulsive force or very weak attractive force, resulting in significant desorption of the immobilized cells from the electrodes. However, some cells remained at the IDEs. Changing the frequency to below or beyond these frequencies desorption rate did not change. However, it seemed that cells were not fully attached to the IDEs because cells were easily eluted from the IDEs by applying a bit higher flow rates; similar behavior happened by turning off the AC. Figure 4.7b,g displays the desorption trend by varying frequency [125].

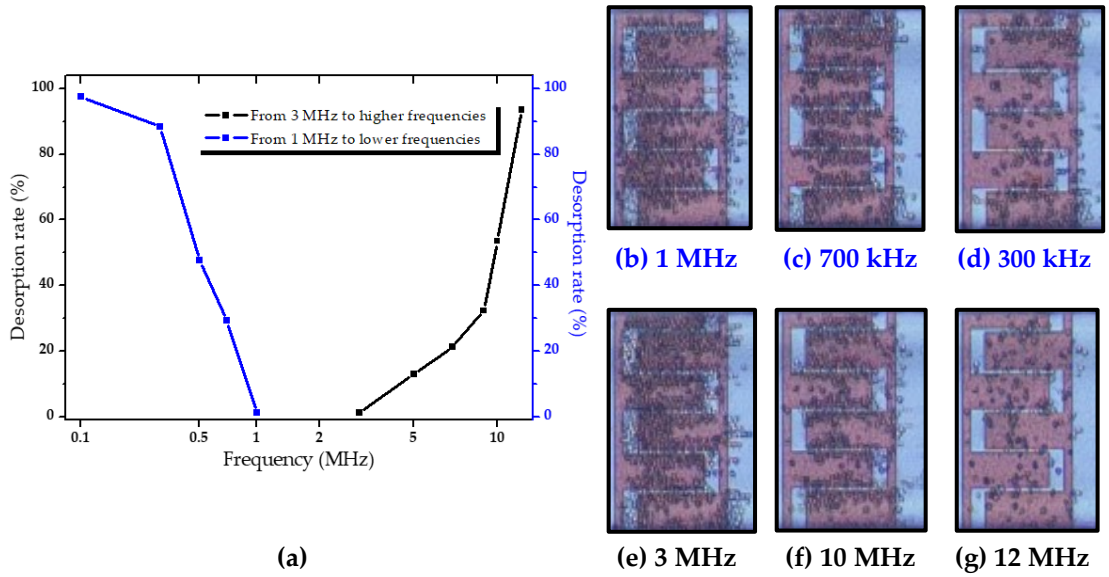

Figure 4.7. DEP behavior of viable yeasts: (a) Desorption rate approximation by changing frequency based on cell coverage at the IDEs; (b-e) the images show the trapping at optimum frequencies (c and g [58]**).**

Further experimental observations indicated that the live cell suspension in tap-water and KCL experienced negative and positive DEP. As expected from simulations, viable yeast cells in PBS solution experience nDEP, whereas in diluted PBS, both negative and positive forces act on the cells. Figure 4.8 illustrates the trajectory of viable cell suspensions in different mediums (water, KCL, PBS, and D-PBS), which leads to trapping of the cell at the IDEs except for sample suspension in PBS, that no trapping taken place due to nDEP. Non-viable cell suspensions in tap-water, KCL, and PBS buffer solutions were solely under nDEP within the entire frequency range [125].

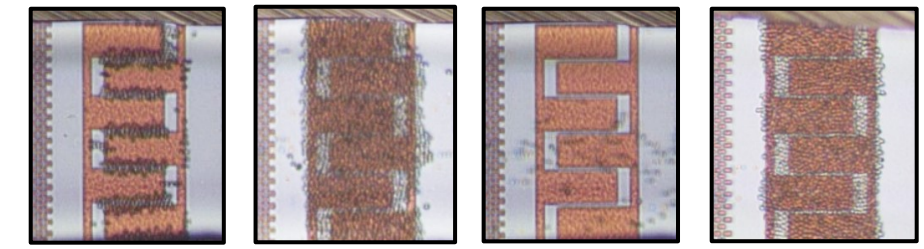

Figure 4.8. DEP behavior of viable yeasts in different suspensions at 20 Vpp and 1 µm s^{-1} flow rate: (a,b, and d) cell immobilization as a result of pDEP and; (c) no trapping as a result of nDEP [125]**.**

Due to the limitation of our signal generator (up to 20 MHz), an investigation of the complete range of pDEP was not possible. However, fc1 (which occurs at around 1

MHz, 11 MHz, and 4 MHz for tap-water, KCL, and D-PBS dilutions, respectively) for all the cases closely matched with the numerical analysis. Figure 4.9 presents the experimentally proven pDEP spectrum for these suspensions and yeast type II in DIW. It can be seen that changing frequency causing DEP change, which affects the trapping behavior over the pDEP band [125].

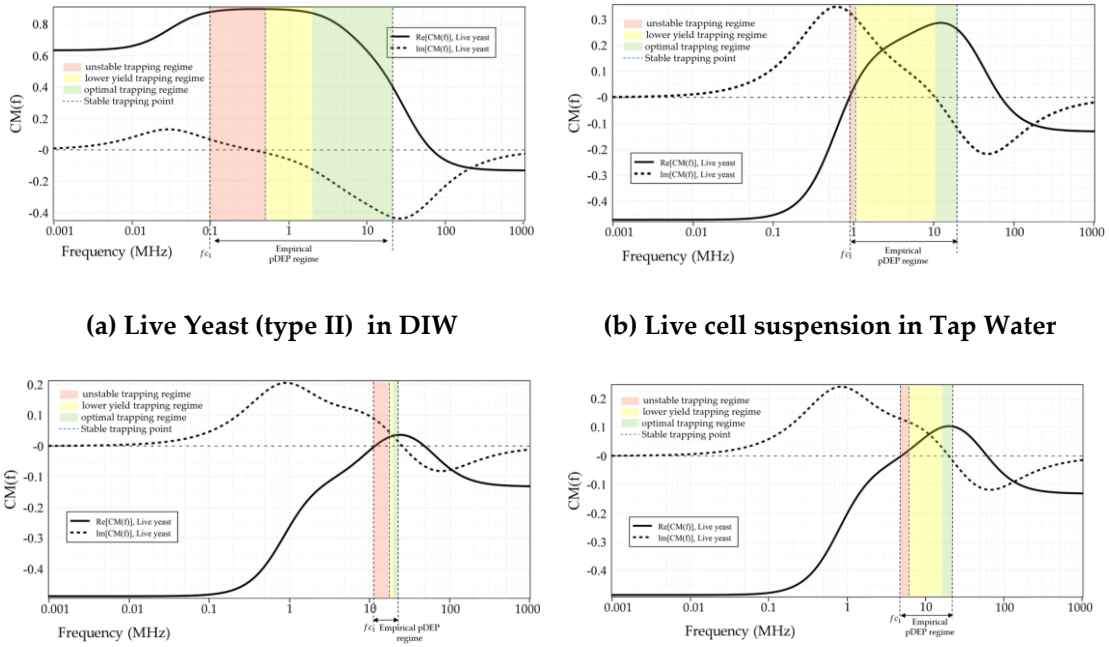

(a) Live Yeast (type II) in DIW

(b) Live cell suspension in Tap Water

(c) Live cell suspension in KCL

(d) Live cell suspension in D-PBS

Figure 4.9. Numerical calculation predictions vs. empirically proven pDEP spectrum and fc for: live yeast suspensions in: (a) DIW and; (b) Tap water [125]**; (c) KCL** [125]**; (d) D-PBS** [125]**. Colored frequency bands demonstrate trapping behavior based upon optical observations** [125]**.**

By comparing all the experimental results, it can be assessed that as the cell solution conductivity expands, the trapping takes place at higher frequencies, and the pDEP spectra get narrower [125]. The trend of cell trapping was approximately similar for all the cases [125]. The immobilization rate was successively enhanced by shifting the real part from the negative (dominant conductivity area) to positive (where permittivity begins to dominate) and obtained its highest value with frequency rise [125]. Furthermore, over the positive $Re[f_{CM}]$ spectrum, the trapping yield was optimum when not only the $Re[f_{CM}]$ was around its maximum level, but also the imaginary part ($Im[f_{CM}]$) was negative (up to shortly before its maximum peak) or minimum positive (around zero) values [125]. The impact of the imaginary part on the trapping trend should be investigated more thoroughly in the future.

Table 4.1 summarizes the DEP characterization results of live and dead cells suspended in various media consistent with all IDE structures at the constant electrical potential and different given electric potential ranges [125].

Table 4.1. DEP characterization results for yeast cell suspensions [125]

MUT [1]		pDEP range (numerical prediction)		pDEP range (empirical)		
Cell	**Media**	**fc1** [2]	**fc2**	**fc1**	**fc2**	**f_{opt}** [3]
Viable yeasts	**DIW**	-	65.4 MHz	100 kHz	12 MHz	1-3 MHz
	Tap water	887 kHz	68.2 MHz	1 MHz	40 MHz [4]	10-14 MHz
	KCL (20 mM)	11.6 MHz	48 MHz	11 MHz	not measured	18-20 MHz
	PBS (0.1 M)	nDEP	nDEP	nDEP	nDEP	-
	D-PBS	4.86 MHz	59.98 MHz	4 MHz	not measured	13-20 MHz
Nonviable yeasts	**DIW**	-	2.5 MHz	20 kHz	2.3 MHz	90-900 kHz
	Tap water	nDEP	nDEP	nDEP	nDEP	-
	KCL (20 mM)	nDEP	nDEP	nDEP	nDEP	-
	PBS (0.1 M)	nDEP	nDEP	nDEP	nDEP	-
	D-PBS	nDEP	nDEP	nDEP	nDEP	-

[1] Material under test, [2] Low-and high crossover frequency points, [3] Optimum trapping frequency range, [4] Measured through separate experiments not mentioned in the text

4.1.2.2 Impact of IDE's geometrical parameter on cell trapping

The impact of geometry on the DEP immobilization was investigated for the yeast suspension in DIW. Computational predictions showed that the IDE's geometrical dimension impacts the DEP-dependent behavior of the cells. Figure 4.10 illustrates simulation analysis of the influence of various geometry ratios on cell trapping. As shown in Figure 4.10a, with increasing ratio, more cells tend to leave the channel, whereas trapping was maximized for smaller dimensional ratios. Figure 4.10b explains this trend more precisely with respect to the total number of the cell treated by DEP using Finite element modeling (FEM). Based on these analyses, immobilization probability defines the number of trapped cells to the total number of cells suspended in the medium solution. By maintaining the spacing at a constant value of 20 μm, IP decreases steadily with decreasing width [58].

DEP experimental outcomes were in good agreement with the simulation assumptions. By applying 20 Vpp at 1 MHz, obvious cell immobilization was observed [58]. For all the cases, cell trapping started right away after cell suspension had reached the IDEs. Cell trapping started at the edges of the IDEs, where the electric field gradient is intensified. Figure 4.11 demonstrates the cell immobilization behavior for the six different IDE structures at three-time intervals [58]. Cell polarization effect, i.e., creation of polarization field in each of the individual cells in an inhomogeneous EF, led to dipole-dipole interaction and forming pearl chains of cells [71].

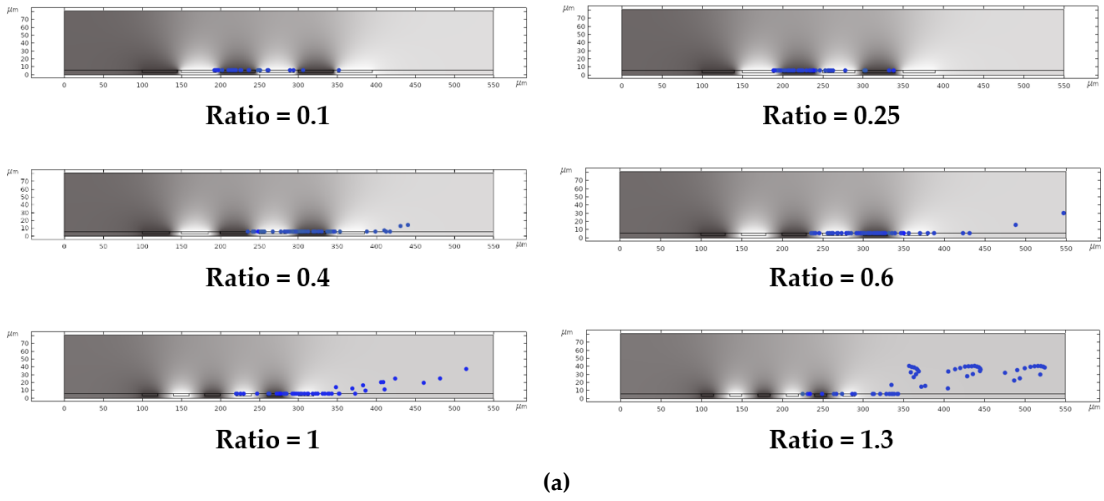

(a)

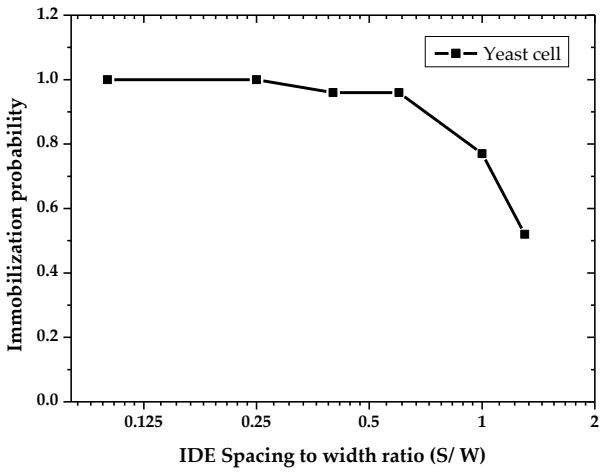

(b)

Figure 4.10. Finite element modeling (FEM) results for dielectrophoretic immobilization of yeast cells at 20 Vpp, 1 MHz: (a) Graphical view of cells trajectory; (b) the immobilization probability analysis [58] **as a result of spacing to width ratio impact.**

As shown in Figure 4.11, the number of entrapped yeast cells is strongly dependent on the dimensional ratio of the IDE structures. The number of entrapped cells was declined with rising IDEs geometrical ratio. Cell entrapment reaches its optimum efficiency by using IDEs with the smallest spacing (5 µm) between consecutive fingers and the biggest finger width (45 µm) [58]. Furthermore, the immobilization of cells using IDEs with higher geometrical ratios was challenging. For these IDEs obtaining a high trapping yield was possible but over a more extended period than the lower ratio IDEs where the optimal trapping was achievable in a shorter time duration [58].

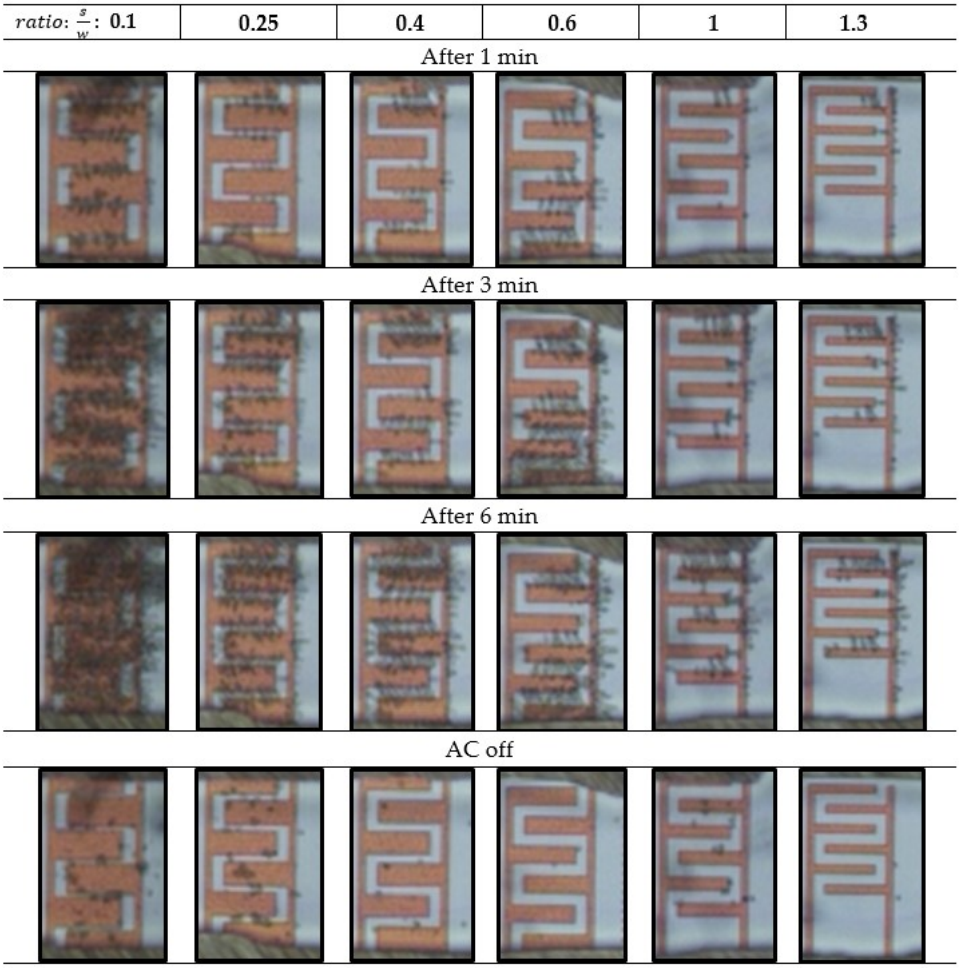

Figure 4.11. Micrographs of the DEP immobilization of live yeast cells utilizing various IDE structures (spacing to width ratios) at 1 min, 3 min, and 6 min intervals [58] **and when AC was turned off. DEP conditions: 20 Vpp, 1 MHz, 1 μm·s^{-1} flow rate.**

This is because the immobilized cells desorb from the IDE structures with increased S/W ratios throughout the DEP trapping [58]. It was seen that for a constant spacing size, increasing an electrode width expands the number of immobilized cells. These optical inspections were in accordance with the simulation assumptions presented in Figure 4.10 [58]. FEM simulations validated the influence of geometrical parameters on the DEP behavior. Increasing the IDEs ratio conversely affects the IP. Cell trapping probability enhanced with lowered IDEs geometrical (spacing to width) ratios. Moreover, it was seen that by keeping the spacing constant at 20 μm, there had been a continuous decay in IP with shortening width (at ratios of 0.6, 1, and 1.3). Thus, it could be noted that the functioning of the IDE is highly affected by its geometrical ratio (S/w) [58].

As demonstrated in Figure 4.12, measurement results showed that smaller IDE ratios minimize the required peak voltages for DEP trapping. For the highest IDE

geometrical ratio, the needed voltage value was almost double as much as the necessary value for the smallest IDE ratio [58].

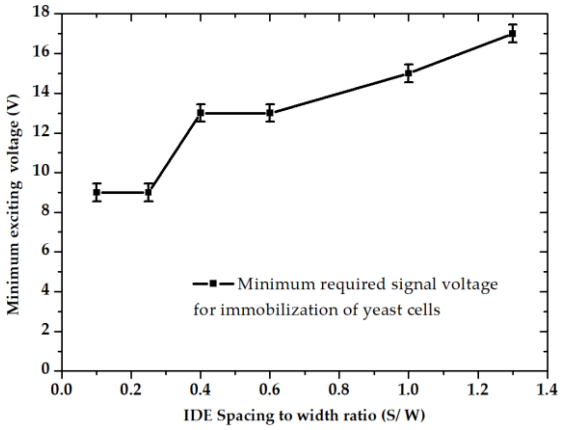

Figure 4.12. Minimum required driving voltage for the initiation of yeast immobilization utilizing various IDE structures, according to DEP experimental data [58]**.**

Furthermore, cell immobilization was improved considerably with a rising voltage trend. As shown in Figure 4.13, the DEP force was intensified by increasing the electric potential, and thus more cells were absorbed by the IDEs. Moreover, it was seen that the trapping trend as a result of frequency variation remains the same, even at a lower electric potential [58]. As demonstrated in Figure 4.13a,b, in both cases (9 Vpp and 20 Vpp), the trapping yield was higher for the given 1 MHz field frequency compared to 9 MHz.

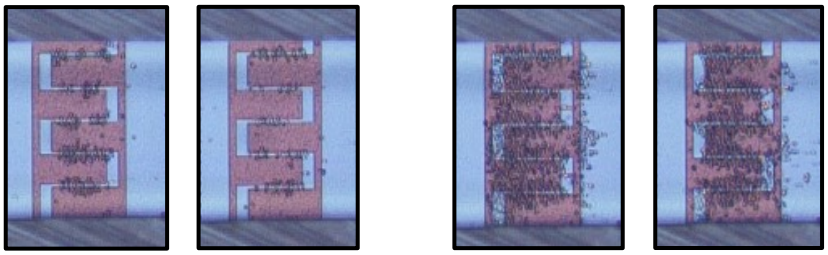

Figure 4.13. Voltage impact on the trapping behavior of the cells.

Furthermore, for all of the IDE structures at the lower voltages, the trapping was very weak, and over time entrapped cells tend to desorb from the IDEs. Figure 4.14 illustrates an example of the weak immobilization due to imposing an AC voltage of 9 Vpp and at 8 MHz, where only a few cells were trapped at the IDEs and entrapped cells eluted from IDEs with the time passage. In contrast, at optimal AC ranges, not only were the cells strongly attracted to the electrodes but also the number of trapped cells was increased over time [58].

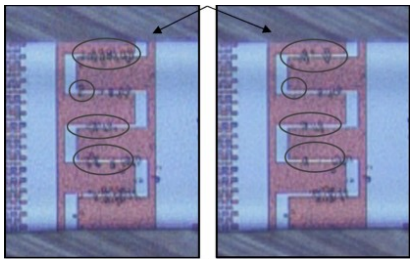

(a) (b)

Figure 4.14. Weak immobilization example upon applying 9 Vpp, 8 MHz, and 1 μm·s^{-1}: (a) Live-cell immobilization results after 2 min; and (b) 3 min, which led to partial desorption of immobilized cells from the IDEs [58]**.**

The minimum required voltage for other yeast suspensions in tap-water, KCL and D-PBS was also examined for the optimum IDE structure (with 0.1 ratio) [58]. Comparing these results showed that immobilization of the cells suspended in tap-water required the lowest voltage value. In contrast, DI-water required the highest electric potential for trapping initiation among all buffer solutions (see Table 4.2).

Table 4.2. Electric potential for pDEP and cell trapping initiation

Medium solution	V_{min} [1]	V_{opt} [2]
DIW	8.5 V_{pp}	14-20 V_{pp}
Tap water	2.5 V_{pp}	10-20 V_{pp}
KCL (20 mM)	8 V_{pp}	17-20 V_{pp}
Diluted PBS	5 V_{pp}	13-20 V_{pp}

[1] Minimum voltage required for trapping, [2] Optimum trapping voltage

4.2 Towards Separation of Cell Mixture

To discriminate viable and non-viable and dead yeast cells and to selectively trap them from live and dead cell mixture, the influence of the AC frequency on live and dead cell mixture trajectory was investigated experimentally and simulated using COMSOL Multiphysics [125]. According to the simulation assumptions shown in Figure 4.2, the live and dead cells' DEP responses are significantly different at high frequencies [63]. Based on the reported experimental results shown in Table 4.1, the fc of dead yeast suspension in DIW occurred at 2.3 MHz compared to 12 MHz for live yeasts [58]. In the other cell solutions (Tap water, KCL, and PBS), dead cells continuously experience nDEP. This change in the DEP behavior of non-viable cells is because of the viability loss of dead cells due to an impaired membrane. Their interior nucleus conductivity is decreased while their membrane conductivity is increased [125]. A damaged membrane of a dead cell is polarized differently when it

is subjected to an EF. Thus, due to these dielectric discrepancies, live and dead cells' responses to the fringing EF are not similar [63,71,135].

Considering the distinct DEP responses of live and dead yeast cells at specific frequency ranges, preliminary indications of cell separation have been carried out. The separation principle was also simulated using COMSOL Multiphysics. Our simulation results were adequately in line with experimental results. Applicability of this microfluidic device for separation, as well as detection applications, leads us a step closer towards the development of multifunctional LoC devices. Cell separation is essential in clinical research and diagnosis of early-stage diseases and various areas such as food production, pharmaceutical industry, and environmental monitoring [125].

4.2.1 Simulation results

Figure 4.15 illustrates the trajectory behavior of non-viable (red dots) and viable (blue dots) yeast cells exposed to an AC electric field with a voltage of 20 Vpp at 6 MHz. Under these conditions, live cells attract to the high electric field regions and immobilize at the electrodes, while dead cells experience nDEP and repel from the electrodes [125]. Therefore, the separation of dead cells from live ones can be achieved.

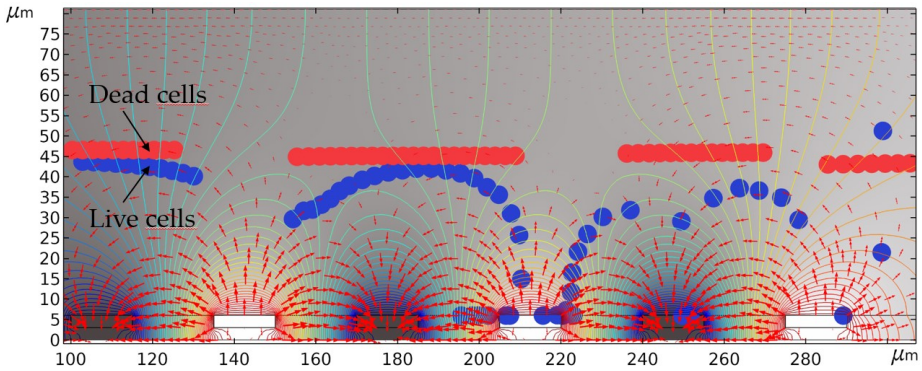

Figure 4.15. Finite element modeling (FEM) results for DEP separation of live and dead yeast cells under 20Vpp, 6 MHz, and 1 μm s^{-1}.

Figure 4.16 illustrates the separation strategy, i.e., how selectively DEP can be used to isolate specific cell kind from a mixture of cells using the differential DEP behavior by exploiting the intrinsic properties of live and dead yeast cells [58]. Holding the field frequency at a fixed value of 3 MHz, dead cells were isolated from live cells, which were simultaneously trapping at the electrodes (Figure 4.16a). The

reverse function happened when a lower range field frequency ($f_o \leq 100$ kHz) was exerted to the system (Figure 4.16b) [58].

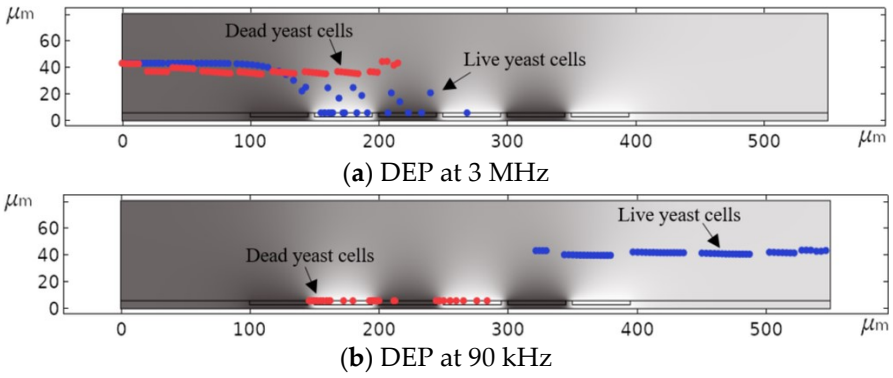

(**a**) DEP at 3 MHz

(**b**) DEP at 90 kHz

Figure 4.16. Finite element simulation assumption for DEP separation of live or dead yeast cells from live and dead cell mixture: (a) Isolation of live cells from dead ones and (b) vice versa as a function of frequency [58].

4.2.2 DEP separation

As discussed earlier, the DEP trapping of live and dead yeast cells under the AC electric field with a frequency spectrum of 10 kHz to 20 MHz was tested separately. Figure 4.17 couples the numerical predictions with the experimentally measured effective pDEP ranges for both viable (highlighted gray zone) and nonviable (highlighted pink zone) cells into one plot. This can be used as a phase diagram to find out the separation regimes of each cell population in the cell mixture. The labeled 1-3 areas determine the measured effective trapping ranges for both types of cells [125].

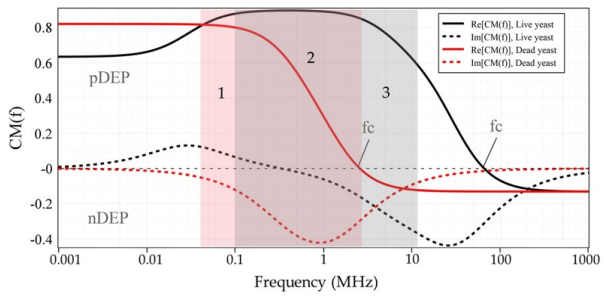

Figure 4.17. CM factor numerical predictions (solid lines) and experimentally measured affective pDEP bands (pink and gray regions) for viable and nonviable cell suspension in DW as a function of frequency [125].

Experimental results demonstrated that dead cells experienced an attractive force between 20 kHz and 2.3 MHz (pink zone). In contrast, pDEP was feasible for live cells in the greyed frequency band (100 kHz-12 MHz). Figure 4.18 shows snapshot images for the trapping of live and dead yeasts at 20 Vpp, where live cells immobilized at 5

MHz (Figure 4.18a) and dead cells immobilized at the electrodes at 80 kHz (Figure 4.18b) [125].

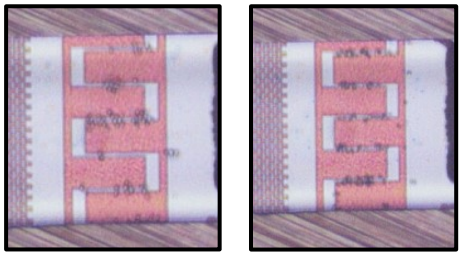

pDEP at 5 MHz (**a**) pDEP at 80 kHz (**b**)

Figure 4.18. DEP separation of viable and non-viable yeast cells: (a**) trapping and isolation of live cells at the IDEs, while dead ones repelling from the IDEs and pushing by the flow through outlet; and (**b**) separation of dead cells from live ones, at 20 Vpp, and 1 μm.s^{-1} flow rate.**

As shown in Figure 4.17, at specific frequency ranges, one type of the cells in the mixture can be selectively trapped and continuously separated from the other cell type. The dead cell can get immobilized and isolated from the live cells upon applying any frequencies from zone 1. Conversely, live cells can be immobilized and isolated from the dead cells while dead yeasts are pushed by the flow through the channel and be separated from live ones upon switching to any frequencies from zone 3. By changing to any frequencies from zone 2, i.e., the overlapped regime, both cell types can get trapped. As a result, to selectively trap live cells from the mixture frequencies less than 100 kHz (in zone 1) and trap dead cells frequencies more than 2.3 MHz (in zone 3) were the most influential conditions for differential separation. The cells released from the microfluidic channel can be collected at the outlet and utilized for further studies and examinations, e.g., viability measurement [125].

The isolation efficacy of viable cells from a viable and stained-nonviable cell mixture was defined during the DEP characterization process (for frequencies within zone 1-3), as shown in Figure 4.19. This was achieved by calculating the entire trapped cells' viability at the IDEs by counting viable and non-viable cells. The rate of the viable cells to the total number of entrapped viable and non-viable cells is termed viability. The targeted cells were trapped at the IDEs differentially separated from the cell mixture introduced into the microfluidic channel by switching frequency using the 1 μm.s^{-1} flow rate at 20 Vpp. As it was expected, it was seen that upon applying frequencies from zone 1, only dead cells could be immobilized, and increasing frequency to zone 2 and 3, the yield of the entrapped viable cell population increased steadily compared to dead cells [125]. Contrary to what was expected from the previous experimental results and simulation predictions, the separation of the viable

cell population attained 100% efficiency at around 5 MHz rather than about 2.3 MHz. This can be referred to as the solution conductivity elevation due to dying the cells with MB, which shifted the higher fc of dead cell solution from 2.3 MHz to around 4.5 MHz. Switching to frequencies below 100 kHz (within zone 1) immensely lowered the isolation efficiency of live cells to 0%. Upon these applied frequency fields, the isolation efficiency of dead cells increased by 100%. Examples of these trends are demonstrated in Figure 4.19b-g [125].

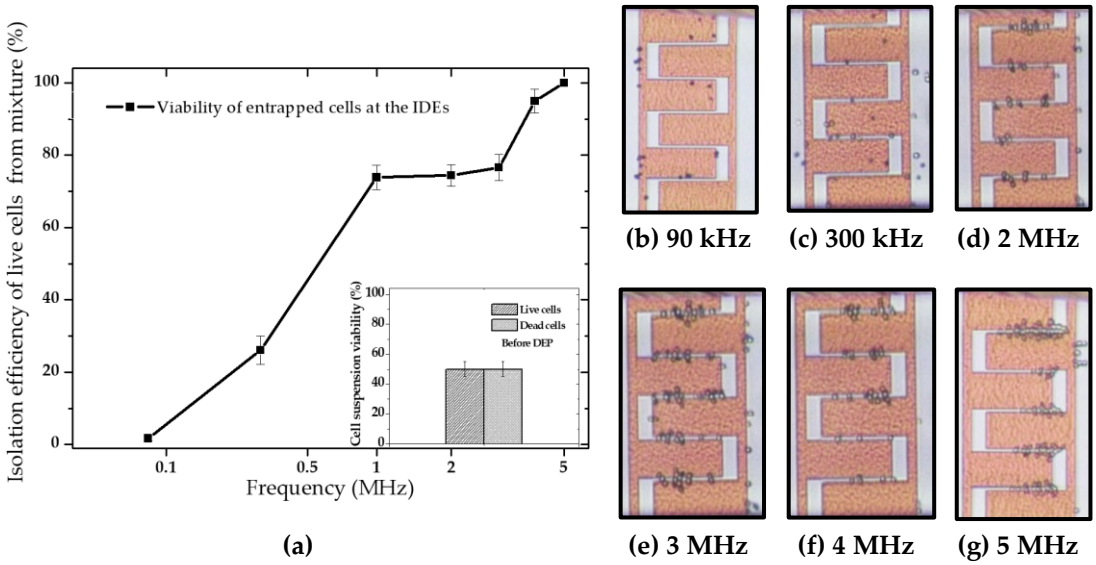

Figure 4.19. Selective DEP separation empirical results from a live and dead cell mixture at a constant voltage of 20 V_{PP}: (a) Live-cell isolation efficiency from the mixture upon switching frequency; (b-e) Micrographs illustrate the isolation percentage of live cells at the IDEs upon frequency rise (b) 0%; (c) 22.22%; (d) 77.35%; (e) 80.19%; (f) 91.66%; and (g) 100%. Colorless cells are live, and stained blue cells are dead. Conductivity of the mixture was 0.1282 S/m, and the ratio of the live and dead cells in the mixture was 1:1 [125]**.**

Figure 4.20 illustrates the differential separation of live and dead cells from a mixture of various buffer media (DIW, KCL, and diluted PBS) [125].

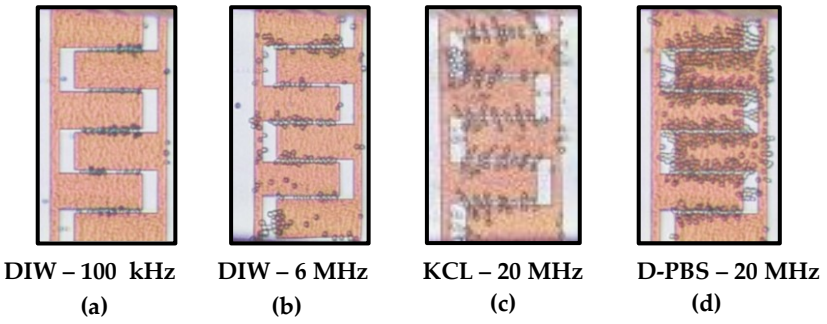

Figure 4.20. Differential separation of the viable and non-viable yeasts from live and dead (1:1) cell mixtures by DEP at 20 V_{pp}: (a) Isolation of dead cells at the IDEs; (b,c [125]**, and d** [125]**) Isolation of live cells using pDEP while dead cells were removed by nDEP.**

4.3 Trapping Efficiency

Optical observations showed that this LoC device has a very fast response, and the immobilization starts right away after applying voltage. At optimal AC ranges, trapping appears spontaneously, as soon as the AC was used, in less than 1 second. This duration can be increased to 5 seconds after running the fluid through the microfluidic channel, depending on other applied AC ranges. Disabling the AC, desorption occurs very fast [125]. However, some cells might remain attached to the electrodes, especially when the material under test had a high cell density. In this case, completely removing the cells off the IDEs was achievable via introducing a higher flow rate through the channel. At some frequencies, where nDEP force was dominant, by approaching the cells to active DEP regions, the mobility of the cells in the direction of movement speeded up instantaneously, and cells tended to pass over the electrodes faster in comparison to cells movement when pDEP or zero DEP was acting on the cells. In contrast, at some frequencies, especially close to crossover frequencies, where pDEP was dominant, the velocity of the cells was relatively reduced as soon as the cells reached the IDE region. However, no trapping was observed. It is assumed that the pDEP was too weak at these frequencies to overcome the drag force and trap the cells [125].

Trapping efficacy of the lowest ratio IDE was approximately estimated at 20 Vpp, 1 MHz, for yeast suspension in DIW, by counting the cells before and after the DEP process inside the collection tubes when the AC was still on. The cell suspension (1 mL) was loaded in the microfluidic channel at a 1 $\mu m \cdot s^{-1}$ (1 $\mu L.min^{-1}$) flow rate. The cell population that was not trapped at the IDEs and released from the channel was collected at the out let in the tubes for additional analysis (counting and viability test). The cell density was approximately counted per milliliter using a hemocytometer (Figure 4.21a) [125]. Using these estimations, the percentage of the entrapped cells (immobilized) was calculated by subtracting the number of the cells gathered at the outlets (Post-DEP) from the entire cells (Pre-DEP), see Figure 4.21b. Analyses estimations showed that almost 53% of the cells were trapped at the electrodes upon the DEP immobilization. In contrast, nearly 47% did not overcome drag force and were pushed by the flow and eluted from the channel because they were either impacted vaguely by pDEP or did not encounter this force at all [125]. This can be linked to the embedded IDEs orientation within the channel, the height of the microfluidic channel compared to the size of the cells, or the effective distance of the electric field gradient over the electrodes. The height of the microfluidic channel was more than 10 times the cell's diameter. Furthermore, as was discussed earlier, the EF's magnitude over the IDEs diminishes towards the top of the microfluidic channel from the IDE surface. As a result, the flowing of the cells from significantly above the effective EF region and

not getting affected by EFG because they did not encounter this field (based on the simulation results shown in Figure 4.22.) led to deflection of the cells by any of the DEP forces. Therefore, cells only kept flowing in the solution stream and released from the microfluidic channel [125].

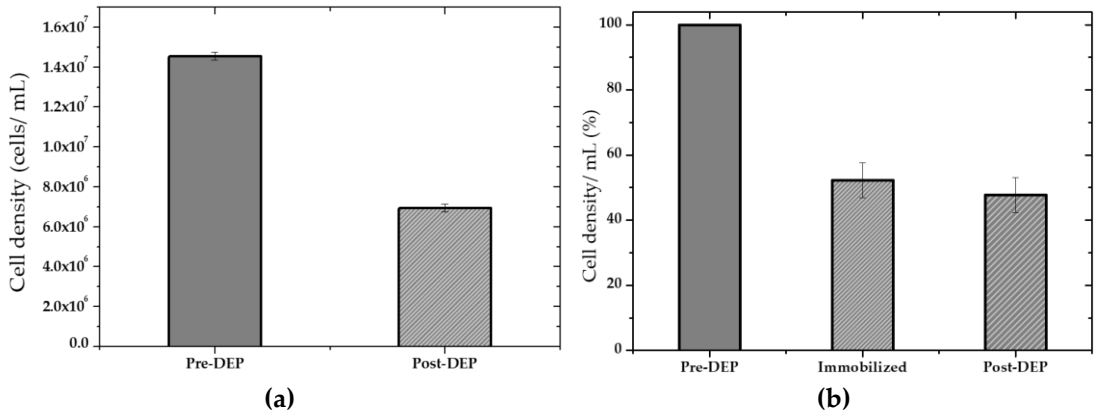

Figure 4.21. Trapping efficiency with cell density estimation before and after DEP. The cells were immobilized using pDEP at 3 MHz, 20 V_{pp}: (a) Approximate MUT cell density; (b) Estimation of the immobilized cell percentage using cell counting [125].

Thus, channel height can be reduced by at least half of its current size to solve this problem. So, optimization of the channel height should be considered for future investigations.

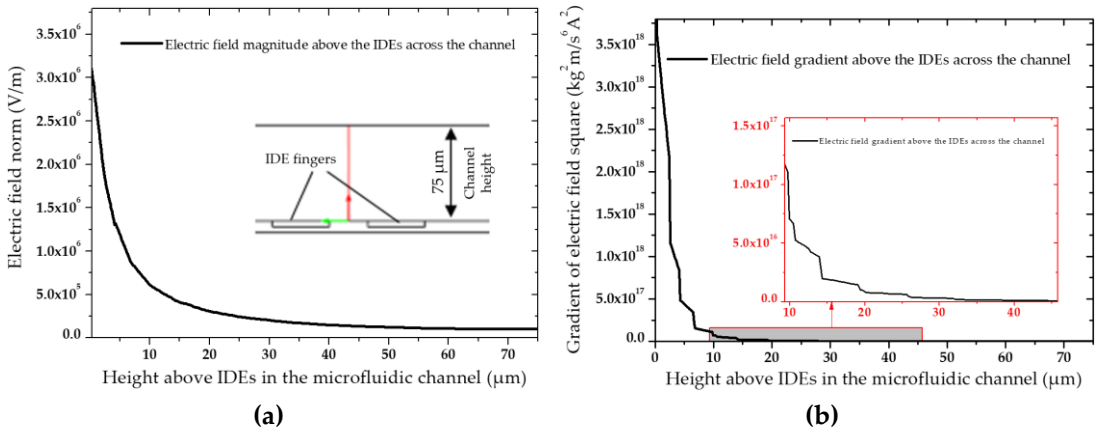

Figure 4.22. (a) Electric field (E) and; (b) Electric field gradient (∇E^2) distribution between the electrode fingers with the distance from the IDEs across the microfluidic channel.

Moreover, it was observed that the trapping efficiency for low cell density MUTs was higher compared to high cell density MUTs. One reason can be attributed to the trapping capacity of the electrodes. For high cell density samples, oversaturation of the IDEs with trapped cells appeared as a result of cell accumulation around the IDEs, especially the electrode edges where the EFG is maxima. As cell injecting through the

channel was continued during the DEP process, the IDEs saturation with immobilized cells started to take place, and pearl chains structure were formed in the direction of the EF. This led to trapping yield shrinkage because the pDEP regions were not available for new cells. On the other hand, oversaturation occurred, which promoted cells desorption from the IDEs with the time passage [125]. Figure 4.23 is an example of these illustrations where saturation negatively impacts the trapping efficiency.

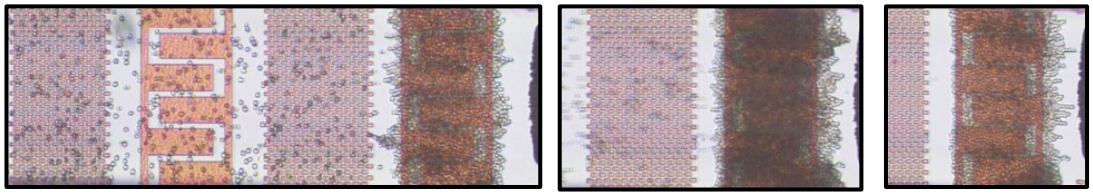

(a) Trapped cell population during DEP **(b) Oversaturated** **(c) Desaturated**

Figure 4.23. Oversaturation of the IDEs with already enriched cell population using a high cell density MUT (1.45×10^7 cells mL^{-1}) which led to trapping instability.

Thus, adjusting a cell density to lower orders of magnitude ($< 10^6$) could benefit the absorbing efficacy. Using meager flow rates and even further by stopping the flow rate for a while when cells reach the channel, letting the cells be settled down and sediment at the channel, and then re-starting the flow rate could also improve the trapping efficiency to around 100% [125].

As represented in Figure 4.24a, analysis before DEP measurement and after that revealed that the viability of the cell solution has fallen by 14% after DEP measurement. Viability estimation indicated that at 1 MHz (in the overlapped region - zone 2), live cells experienced the pDEP more than the dead ones. Thus, the rate of live cells immobilization and isolation from the mixture was higher than dead cells (see Figure 4.24b) [125].

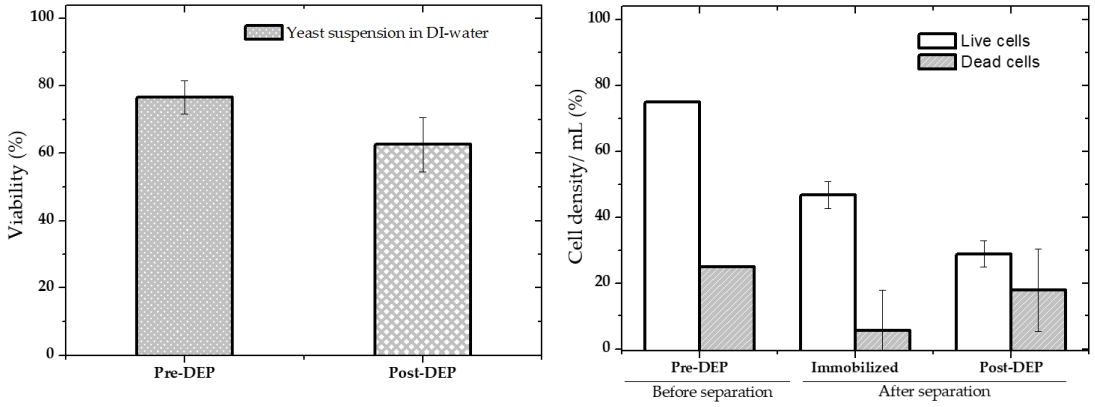

Figure 4.24. An approximate estimate of cell separation from a cell mixture at the applied condition of 20 Vpp, 1MHz, and 1 $\mu m.s^{-1}$ flow rate. The dilution ratio of live and dead cells in the mixture prior to separation was 3:4 [125].

It was estimated that during cell isolation from the mixture, more than 37% of the non-viable cells and more than 59% of the viable cells remained in the pDEP at the IDEs. In comparison, almost 63% of the non-viable yeasts and less than 43% of viable ones were eluted from the channel. This can be attributed to dead cell response to a weaker pDEP as a result of inadequate permittivity and conductivity difference with its surrounding media. In addition, the DEP force is closer to fc at 1 MHz and weaker than lower frequencies in its effective pDEP spectrum. Accordingly, the release of non-viable cells from the channel is 20% more than viable ones [125].

4.4 Summary

This chapter explored the DEP characterization of viable and non-viable yeast cells. Different sample suspensions were used during the measurements, and the experimental results were compared with the numerical simulations [58]. The proof-of-concept for detection and separation applications using the developed LoC device was validated and confirmed by experiments.

These characterizations were compared in terms of electrode performance with a view to determine the best electrode geometry structure to implement an on-chip detection process. The results were found to be mostly close to the simulation assumptions. Both COMSOL simulation results and experimental verifications demonstrated that the optimal configuration belongs to the lower IDE ratio (i.e., bigger electrode width and smaller spacing).

The device was found to have a rapid response time, and trapping was obtained spontaneously after applying an electric potential. DEP force-frequency profile indicated that frequency variation influences cells' trajectory and generates DEP force in two different directions (positive and negative). Moreover, frequency impacts the trapping yield (cell accumulation) at the IDEs. Keeping the flow velocity at a minimum rate improved the trapping yield [125]. The increasing electric potential was found to be very influential in obtaining higher immobilization rates. The pDEP manipulation was applicable for low-conductivity media. Thus, trapping was tunable by changing the medium's electrical conductivity.

The differential separation approach was found to work sufficiently well to be suited for implementing the final design. Therefore, due to the dissimilar intrinsic DEP behavior of the viable and non-viable yeast cells, selective separation of cells from live and dead cell mixture using the proposed design was achievable.

The trapping efficiency was estimated to be limited to around 53% for high cell density suspensions as a result of electrode saturation and tracing of the cells flowing

in the stream of the fluid from the very top of the channel where the magnitude of the electric field was limited and led to elution of cells flowing from the channel. The latter can likely be improved upon, as the microfluidic fluidic channel's height was not optimized.

5 Conclusion and Outlook

This thesis covered the work undertaken for my doctoral research studies. This project aimed to develop a proof-of-concept of a LoC platform to characterize and manipulate yeast cells. Such a LoC system's ultimate goal is to rapidly detect and identify infectious diseases, such as a virus (Influenza, Corona- COVID-19), and enrichment of specific cell types from other blood cells. Parts of this conclusion have been published in [58,122,125].

The targets for the prototype system were as follows:

1. Operating with biological cells
2. Handling low sample volumes
3. Offering fast operational response time
4. Maximizing the device sensitivity by monolithic integration of the device and microfluidic channel
5. Employing miniaturized silicon microfluidic channel rather than larger-scale polymeric channels
6. Adapting the same electrode structure already established at IHP for RF bio-sensing to a dielectrophoretic structure
7. Implementing scalable and affordable manufacturing processes
8. CMOS compatibility (in terms of fabrication process and operational range)
9. Offering flexibility to run different measurements (cell detection & separation)

A novel, silicon-based CMOS integrated microfluidic device was demonstrated similar to [126]. The project's scope expanded to include optimized interdigitated electrodes (IDEs), adapted from the previously established RF sensors at IHP for dielectrophoretic structure. By this point, the designed IDEs had been fabricated on the topmost metal layer of the CMOS stack in a way they placed at the bottom of the microfluidic channel.

The device has been used to selectively immobilize live and dead yeast cells via DEP. Furthermore, the device's capability to separate specific cells from a cell mixture, based on the selective DEP forces, pDEP and nDEP, was also explored.

IDEs with various spatial wavelengths (width and spacing) were studied. The impact of DEP force on cell trapping due to the variation of voltage, frequency, flow rate, and IDE geometry was investigated experimentally. Therefore, FEM was used to predict the cells' trajectories. Experimental and simulation results demonstrated that the microfluidic device could be used to immobilize and separate specific cells by varying the AC frequency based on cells' particular properties. It was found that the experimental results were in agreement with the simulation [58].

The end result was a low-cost device compatible with the CMOS production line, enabling its future commercially mass production. The device also offers more potential functionalities in terms of sensing, read-out the trapped cells, and as a result performing both sample preparation and analysis on a single platform. The simplicity of the designed microfluidic platform for detection applications, besides its functionality for separation applications without any additional or specialized electrode structure, along with its flexibility to be used for different types of cells, makes it a prominent system developed so far for commercialization purposes. This enables quick diagnosis by sensitive detection and fast analysis [125].

5.1 Components Modeling and Optimization

The feasibility of the CMOS integrated microfluidic LoC for dielectrophoretic immobilization of cells was first investigated by COMSOL finite element modeling (FEM). IDE's spatial wavelength (width and spacing) were characterized and optimized based on essential external parameters, such as the fluid's voltage, frequency, and velocity through the microfluidic channel [122]. Two main perceptions have been examined and demonstrated using simulation analysis: the viability of DEP for cell trapping and the influence of geometry ratio (spacing to width), frequency, voltage, and flow rate to generate the most efficient DEP force on medical samples [58].

Simulation results showed that by increasing the applied voltage trapping of smaller particles on electrodes is enhanced**.** The change of frequency does not directly influence the DEP force for improving the immobilization of cells but instead controls the crossover frequency between negative and positive DEP. Reducing the fluid flow velocity forces impacted particle immobilization. The impact of IDE geometry on the particles' tracing and immobilization was investigated by keeping the voltage constant. To this end, systematic simulations were performed.

Simulation analysis showed that the ratio between the electrodes' spacing and the width is impacted by the IDE's performance**.** According to these predictions, the IDE's finger's width has to be increased, whereas the spacing has to be reduced. This ensured the trapping of more particles, which would be beneficial for cell enrichment from the mixture. Furthermore, the simulation and design of planar IDEs were evaluated to maximize the immobilization probability of submicron-sized particles. Based on the results, six IDE designs with optimum geometrical parameters were proposed for fabrication and integration with a microfluidic channel.

Numerical simulations offered a beneficial and valuable tool to model and analyze the cells/particles' DEP behavior and optimize electrode geometry. Besides, it was replaced by time-consuming and costly iterative fabrication procedures.

5.2 Sample-preparation Development

After successfully designing and optimizing IDEs, the development of the sample preparation was addressed. The optimized IDEs were fabricated into a CMOS device, integrated with the silicon microfluidic channel, and packaged with a glass wafer. The whole process was done using the standard 250 nm high-performance SiGe CMOS/BiCMOS technology of IHP. This technology enabled the fabrication of a single chip with separate microfluidic and electrical interfaces. Furthermore, the transparent glass used as channel closing provided simultaneous electric and optical measurements.

An interconnection system was developed to interface the microfluidic channel with the microfluidic system via manifold technology. This was used in order to facilitate the handling of the cell suspension to the IDEs and control the fluid flow through the channel. This setup created a platform to test the device proof-of-concept.

In the next step, various cell sample solutions were prepared. Live and dead cell suspensions were applied separately for characterization and manipulation experiments and were mixed for separation experiments. Dead cells were achieved by

heat-killing the live cells at 100°C for 30 min. DIW, TW, KCL, PBS, and D-PBS were used as mediums for cell suspension. Various media with conductivities ranging from 10^{-4} to 1 were used for the experimental investigation [125]. The viability of the sample suspension was estimated before and after the DEP measurements.

5.3 Dielectrophoretic Characterization

The proof-of-concept for trapping and separation applications were validated and confirmed by experiments. To verify the functionality of the IDEs, a comparison between simulation and experimental results was performed. Yeast cells were selected as model organisms and DIW as a model liquid carrier. This choice was made to keep the primary model very simple and avoid complications to achieve a reliable comparison between experimental and simulation results. However, this design can also be utilized for the analysis of more advanced models (e.g., cell suspensions in more complex media). The cells' motion was investigated optically and compared with the simulation results [58,125].

IDEs have been shown suitable for the trapping and immobilization of yeast cells within a CMOS-based microfluidic device. The simulation and experimental results showed that the optimal IDE configuration belongs to the smallest IDE geometrical ratio (0.1); to maximize the electric field gradient within the capture region. This IDE configuration achieved the highest capture of cells on the entire IDE area among all the other IDE configurations at the constant condition. Furthermore, at suitable applied frequency and voltage, experimental results showed that the device has a very fast response time, and the cells are trapped at the IDEs shortly after flowing through the channel.

The study exhibited that during DEP trapping, the desired cells are pushed toward particular regions and increase the local concentration. Over time, more cells are trapped by passing more suspension solution over the IDEs, and the cell concertation is increased at the IDEs. Therefore, to maximize the trapping capacity at the IDEs, the electrode area must be large enough, which particularly suits the bigger electrode width and smaller finger gaps. Moreover, the lowest electrode aspect ratio (0.1) enabled the reduction of applied voltage by half compared to the required voltage by the highest electrode aspect ratio (1.3) (e.g., for live cells suspension in DIW, from 17 Vpp down to 8.5 Vpp).

The dead cell suspension in DIW, as well as live cell suspension in DIW, tap water, KCL, and diluted PBS showed positive DEP response in specific frequency ranges. However, negative DEP was observed for the rest of the viable and non-viable cell

suspensions. As the medium conductivity increased, the pDEP spectrum got smaller, and trapping occurred at higher frequencies. The cell trapping behavior for all materials under test was about similar. They exhibited a gradual increase in trapping yield by the transition of the real part from negative to positive. By increasing frequency, cell trapping obtained its highest yield. However, lower frequency ranges were needed for trapping smaller cells. To achieve an efficient DEP force for cell trapping and manipulation at lower frequencies, larger EFGs were essential. Thus, trapping efficiency can be tuned with increasing electric potential [125].

Our CMOS integrated microfluidic device offered the potential for isolation and separation of specific cell types using IDEs. Cell immobilization could also be used as a separation technique. By trapping cells of interest (either live or dead cells) from a cell mixture, the remaining cells could be washed away with fluid flow to leave a purified cell population. Wider IDE fingers aided in the generation of greater EF strength. The higher aspect ratio of the electrode structure was beneficial for analyzing the higher cell-concentration samples, which resulted in better isolation efficiencies in separation applications.

Analyses estimations showed that almost 53% of the cells were trapped at the electrodes upon the DEP immobilization. By comparison, approximately 47% did not overcome drag force and were washed from the channel. This can be related to the fact that these cells either did not experience the DEP force or were impacted very slightly. The use of 75 μm channel height could be problematic for trapping because the DEP force will decrease quickly as the distance from the planar electrodes increases. However, the cells reaching the channel can be settled for a longer period. This can increase the trapping efficiency to around 100% [125]. The current results showed promise towards using this CMOS integrated DEP-based silicon microfluidic device as a tool to enable detection and separation of bioparticles.

5.4 Outlook

The proof-of-concept microfluidic integrated LoC device with interdigitated electrodes ensured the cells' characterization and manipulation for detection and separation applications. Monolithic integration of the device and its potentiality for both sample preparation and analysis on a single platform, as well as operational simplicity, offers excellent benefits from a cost and commercialization perspective.

Looking forward, there is a significant potential for this LoC platform and exciting possibilities for future development, e.g., the evolution of multi-purpose LoC for disease diagnostics under the frame of the near-patient portable testing systems or

point of care (PoC) to be used even out of clinical and hospital environments. This device's rapid analysis capability could ensure the fast identification and enumeration of an infection's causative pathogens in blood and other fluidic-based samples. This could reduce the risk of the disease spreading (especially for fast-spreading infectious diseases such as Influenza and COVID-19), analysis turn-around time, treatment costs, patient's suffering, and last but not least, could save lives.

However, the realization of such a system requires further validations and modifications. This work could be developed in different aspects, and the first step would be to test the device using clinical samples. The next step would be to test the chemical interaction of the silicon with biological samples. From the fabrication point of view, the circuitry for sensing and read-out would also need incorporation to fulfill all the LoC requirements. Channel optimization is required to better control the cell tracing and assess if it influences the cells' elution even at optimal conditions.

Moreover, the more important directions would be to change the orientation of the IDEs within the channel, use different electrode materials, and even use different electrode geometries to understand the potential and limitations of the current method and improve the resolution and precision of the device. Thus, these aspects could be reconsidered for the following research levels. Finite element simulations of cells' DEP behavior in the microfluidic channel considering those other influencing parameters (such as Brownian, buoyancy and gravitational forces, etc.) might help develop a broader theoretical understanding of the system's complexity.

As it is clear nowadays that we are dealing with the world's biggest pandemic (Coronavirus) during the last decades, the standard and conventional laboratory-based approaches couldn't provide the rapid turn-around for mass screening. Therefore, it is hoped that very soon, research such as this will bring significant change, not only by making diagnostics very fast and spontaneous even in non-laboratory conditions but also by making the equipment more affordable and widely available for all. It is hoped that in the coming decades, with the advent of such research technology, viral infectious diseases were not likely a big threat in our lifetimes.

6 Bibliography

1. Wang, X.B.; Huang, Y.; Gascoyne, P.R.C.; Becker, F.F. Dielectrophoretic manipulation of particles. *IEEE Trans. Ind. Appl.* **1997**, *33*, 660–669.

2. Altomare, L.; Leonardi, A.; Medoro, G.; Guerrieri, R.; Tartagni, M.; Manaresi, N. A lab-on-a-chip for cell detection and manipulation. *IEEE Sens. J.* **2003**, *3*, 317–325.

3. Henslee, E.A.; Sano, M.B.; Rojas, A.D.; Schmelz, E.M.; Davalos, R. V. Selective concentration of human cancer cells using contactless dielectrophoresis. *Electrophoresis* **2011**, *32*, 2523–2529.

4. Jen, C.-P.; Chen, T.-W. Selective trapping of live and dead mammalian cells using insulator-based dielectrophoresis within open-top microstructures. *Biomed. Microdevices* **2009**, *11*, 597–607.

5. Adekanmbi, E.O.; Srivastava, S.K. Dielectrophoretic applications for disease diagnostics using lab-on-a-chip platforms. *Lab Chip* **2016**, *16*, 2148–2167.

6. Li, H.; Zheng, Y.; Akin, D.; Bashir, R. Characterization and modeling of a microfluidic dielectrophoresis filter for biological species. *J. Microelectromechanical Syst.* **2005**, *14*, 103–112.

7. West, J.; Becker, M.; Tombrink, S.; Manz, A. Micro Total Analysis Systems: Latest Achievements. *Anal. Chem.* **2008**, *80*, 4403–4419.

8. Zhang, H.; Chang, H.; Neuzil, P. DEP-on-a-chip: Dielectrophoresis applied to microfluidic platforms. *Micromachines* **2019**, *10*, 1–22.

9. Pesch, G.R.; Lorenz, M.; Sachdev, S.; Salameh, S.; Du, F.; Baune, M.; Boukany, P.E.; Thöming, J. Bridging the scales in high-throughput dielectrophoretic (bio-)particle separation in porous media. *Sci. Rep.* **2018**, *8*, 10480.

10. Suehiro, J.; Zhou, G.; Imamura, M.; Hara, M. Dielectrophoretic filter for separation and recovery of biological cells in water. *IEEE Trans. Ind. Appl.* **2003**, *39*, 1514–1521.

11. Jones, I.L.; Livi, P.; Lewandowska, M.K.; Fiscella, M.; Roscic, B.; Hierlemann, A. The potential of microelectrode arrays and microelectronics for biomedical research and diagnostics. *Anal. Bioanal. Chem.* **2011**, *399*, 2313–2329.

12. Khan, S.M.; Gumus, A.; Nassar, J.M.; Hussain, M.M. CMOS Enabled Microfluidic Systems for Healthcare Based Applications. *Adv. Mater.* **2018**, *30*, 1–26.

13. Jesús-Pérez, N.M.; Lapizco-Encinas, B.H. Dielectrophoretic monitoring of microorganisms in environmental applications. *Electrophoresis* **2011**, *32*, 2331–2357.

14. Liu, Z.; Han, X.; Qin, L. Recent Progress of Microfluidics in Translational Applications. *Adv. Healthc. Mater.* **2016**, *5*, 871–888.

15. Bayraktar, T.; Pidugu, S.B. Characterization of liquid flows in microfluidic systems. *Int. J. Heat Mass Transf.* **2006**, *49*, 815–824.

16. MALSCH, D.; KIELPINSKI, M.; MERTHAN, R.; ALBERT, J.; MAYER, G.; KOHLER, J.; SUSE, H.; STAHL, M.; HENKEL, T. μPIV-Analysis of Taylor flow in micro channels. *Chem. Eng. J.* **2008**, *135*, S166–S172.

17. Verpoorte, E.; De Rooij, N.F. Microfluidics meets MEMS. *Proc. IEEE* **2003**, *91*, 930–953.

18. Whitesides, G.M. The origins and the future of microfluidics. *Nature* **2006**, *442*, 368–73.

19. Heon Lee, K.; Soo Lee, K.; Ho Jung, J.; Bong Chang, C.; Jin Sung, H. Optical mobility of blood cells for label-free cell separation applications. *Appl. Phys. Lett.* **2013**, *102*, 141911.

20. Landenberger, B.; Höfemann, H.; Wadle, S.; Rohrbach, A. Microfluidic sorting of arbitrary cells with dynamic optical tweezers. *Lab Chip* **2012**, *12*, 3177.

21. Werner, M.; Merenda, F.; Piguet, J.; Salathé, R.-P.; Vogel, H. Microfluidic array cytometer based on refractive optical tweezers for parallel trapping, imaging

and sorting of individual cells. *Lab Chip* **2011**, *11*, 2432.

22. Zhu, S.; Jiang, F.; Han, Y.; Xiang, N.; Ni, Z. Microfluidics for label-free sorting of rare circulating tumor cells. *Analyst* **2020**.

23. Zhang, X.; Ma, L.; Zhang, Y. High-resolution optical tweezers for single-molecule manipulation. *Yale J. Biol. Med.* **2013**, *86*, 367–83.

24. Zhang, Q.; Yin, T.; Xu, R.; Gao, W.; Zhao, H.; Shapter, J.G.; Wang, K.; Shen, Y.; Huang, P.; Gao, G.; et al. Large-scale immuno-magnetic cell sorting of T cells based on a self-designed high-throughput system for potential clinical application. *Nanoscale* **2017**, *9*, 13592–13599.

25. Fernandes Patrício, T.M.; Panseri, S.; Sandri, M.; Tampieri, A.; Sprio, S. New bioactive bone-like microspheres with intrinsic magnetic properties obtained by bio-inspired mineralisation process. *Mater. Sci. Eng. C* **2017**, *77*, 613–623.

26. Schmitz, B.; Radbruch, A.; Kümmel, T.; Wickenhauser, C.; Korb, H.; Hansmann, M.L.; Thiele, J.; Fischer, R. Magnetic activated cell sorting (MACS) - a new immunomagnetic method for megakaryocytic cell isolation: Comparison of different separation techniques. *Eur. J. Haematol.* **2009**, *52*, 267–275.

27. David, R.; Groebner, M.; Franz, W.-M. Magnetic Cell Sorting Purification of Differentiated Embryonic Stem Cells Stably Expressing Truncated Human CD4 as Surface Marker. *Stem Cells* **2005**, *23*, 477–482.

28. Said, T.M.; Grunewald, S.; Paasch, U.; Glander, H.-J.; Baumann, T.; Kriegel, C.; Li, L.; Agarwal, A. Advantage of combining magnetic cell separation with sperm preparation techniques. *Reprod. Biomed. Online* **2005**, *10*, 740–746.

29. Xiang, N.; Shi, Z.; Tang, W.; Huang, D.; Zhang, X.; Ni, Z. Improved understanding of particle migration modes in spiral inertial microfluidic devices. *RSC Adv.* **2015**, *5*, 77264–77273.

30. Xiang, N.; Zhang, X.; Dai, Q.; Cheng, J.; Chen, K.; Ni, Z. Fundamentals of elasto-inertial particle focusing in curved microfluidic channels. *Lab Chip* **2016**, *16*, 2626–2635.

31. Tang, J.C.Y.; Szikra, T.; Kozorovitskiy, Y.; Teixiera, M.; Sabatini, B.L.; Roska, B.; Cepko, C.L. A Nanobody-Based System Using Fluorescent Proteins as Scaffolds for Cell-Specific Gene Manipulation. *Cell* **2013**, *154*, 928–939.

32. Bhagat, A.A.S.; Hou, H.W.; Li, L.D.; Lim, C.T.; Han, J. Pinched flow coupled shear-modulated inertial microfluidics for high-throughput rare blood cell separation. *Lab Chip* **2011**, *11*, 1870.

33. Hou, H.W.; Bhattacharyya, R.P.; Hung, D.T.; Han, J. Direct detection and drug-resistance profiling of bacteremias using inertial microfluidics. *Lab Chip* **2015**,

15, 2297–2307.

34. Deng, Y.; Davis, S.P.; Yang, F.; Paulsen, K.S.; Kumar, M.; Sinnott DeVaux, R.; Wang, X.; Conklin, D.S.; Oberai, A.; Herschkowitz, J.I.; et al. Inertial Microfluidic Cell Stretcher (iMCS): Fully Automated, High-Throughput, and Near Real-Time Cell Mechanotyping. *Small* **2017**, *13*, 1700705.

35. Gascoyne, P.; Shim, S. Isolation of Circulating Tumor Cells by Dielectrophoresis. *Cancers (Basel).* **2014**, *6*, 545–579.

36. Gagnon, Z.R. Cellular dielectrophoresis: Applications to the characterization, manipulation, separation and patterning of cells. *Electrophoresis* **2011**, *32*, 2466–2487.

37. Laux, E.-M.; Knigge, X.; Bier, F.F.; Wenger, C.; Hölzel, R. Aligned Immobilization of Proteins Using AC Electric Fields. *Small* **2016**, *12*, 1514–1520.

38. Mark, D.; Haeberle, S.; Roth, G.; von Stetten, F.; Zengerle, R.; Garcia, E.W.; Lebruska, L.L.; Laurent, M.; Shen, R.; Barker, D.; et al. Microfluidic lab-on-a-chip platforms: requirements, characteristics and applications. *Chem. Soc. Rev.* **2010**, *39*, 1153.

39. Manczak, R.; Baristiran Kaynak, C.; Kaynak, M.; Palego, C.; Lalloue, F.; Pothier, A.; Saada, S.; Provent, T.; Dalmay, C.; Bessette, B.; et al. UHF-Dielectrophoresis Crossover Frequency as a New Marker for Discrimination of Glioblastoma Undifferentiated Cells. *IEEE J. Electromagn. RF Microwaves Med. Biol.* **2019**, *3*, 191–198.

40. Pesch, G.R.; Du, F. A review of dielectrophoretic separation and classification of non-biological particles. *Electrophoresis* **2021**, *42*, 134–152.

41. Martinez-Duarte, R. Microfabrication technologies in dielectrophoresis applications-A review. *Electrophoresis* **2012**, *33*, 3110–3132.

42. Ramos, A.; Morgan, H.; Green, N.G.; Castellanos, A. Ac electrokinetics: a review of forces in microelectrode structures Dielectrophoretic investigations of sub-micrometre latex spheres N G Green and H Morgan - Ac electrokinetics: a survey of sub- micrometre particle dynamics. *J. Phys. D. Appl. Phys.* **1998**, *31*, 2338–2353.

43. Rashed, M.Z.; Williams, S.J. Advances and applications of isomotive dielectrophoresis for cell analysis. *Anal. Bioanal. Chem.* **2020**, *412*, 3813–3833.

44. Modarres, P.; Tabrizian, M. Alternating current dielectrophoresis of biomacromolecules: The interplay of electrokinetic effects. *Sensors Actuators, B Chem.* 2017, *252*.

45. Shafiee, H.; Sano, M.B.; Henslee, E.A.; Caldwell, J.L.; Davalos, R. V. Selective

isolation of live/dead cells using contactless dielectrophoresis (cDEP). *Lab Chip* **2010**, *10*, 438.

46. Hagedorn, R.; Fuhr, G.; Müller, T.; Gimsa, J. Traveling-wave dielectrophoresis of microparticles. *Electrophoresis* **1992**, *13*, 49–54.

47. Çetin, B.; Li, D. Dielectrophoresis in microfluidics technology. *Electrophoresis* **2011**, *32*, 2410–2427.

48. Regtmeier, J.; Eichhorn, R.; Viefhues, M.; Bogunovic, L.; Anselmetti, D. Electrodeless dielectrophoresis for bioanalysis: Theory, devices and applications. *Electrophoresis* **2011**, *32*, 2253–2273.

49. Duchamp, M.; Lee, K.; Dwir, B.; Seo, J.W.; Kapon, E.; Forró, L.; Magrez, A. Controlled Positioning of Carbon Nanotubes by Dielectrophoresis: Insights into the Solvent and Substrate Role. *ACS Nano* **2010**, *4*, 279–284.

50. Lapizco-Encinas, B.H. On the recent developments of insulator-based dielectrophoresis: A review. *Electrophoresis* **2019**, *40*, 358–375.

51. Lee, S.; Roh, S.M.; Lee, E.; Park, Y.; Lee, B.C.; Kwon, Y.; Kim, H.J.; Kim, J. Applications of converged various forces for detection of biomolecules and novelty of dielectrophoretic force in the applications. *Sensors (Switzerland)* **2020**, *20*, 1–18.

52. Srivastava, S.K.; Gencoglu, A.; Minerick, A.R. DC insulator dielectrophoretic applications in microdevice technology: A review. *Anal. Bioanal. Chem.* **2011**, *399*, 301–321.

53. Keeble, L.; Moser, N.; Rodriguez-Manzano, J.; Georgiou, P. ISFET-Based Sensing and Electric Field Actuation of DNA for On-Chip Detection: A Review. *IEEE Sens. J.* **2020**, *20*, 11044–11065.

54. Pohl, H.A. The Motion and Precipitation of Suspensoids in Divergent Electric Fields. *J. Appl. Phys.* **1951**, *22*, 869–871.

55. Tuukkanen, S.; Toppari, J.J.; Kuzyk, A.; Hirviniemi, L.; Hytönen, V.P.; Ihalainen, T.; Törmä, P. Carbon Nanotubes as Electrodes for Dielectrophoresis of DNA. *Nano Lett.* **2006**, *6*, 1339–1343.

56. Abd Rahman, N.; Ibrahim, F.; Yafouz, B. Dielectrophoresis for Biomedical Sciences Applications: A Review. *Sensors* **2017**, *17*, 1–27.

57. Yang, J.; Huang, Y.; Wang, X.; Wang, X.-B.; Becker, F.F.; Gascoyne, P.R.C. Dielectric Properties of Human Leukocyte Subpopulations Determined by Electrorotation as a Cell Separation Criterion. *Biophys. J.* **1999**, *76*, 3307–3314.

58. Matbaechi Ettehad, H.; Soltani Zarrin, P.; Hölzel, R.; Wenger, C.

Dielectrophoretic Immobilization of Yeast Cells Using CMOS Integrated Microfluidics. *Micromachines* **2020**, *11*, 501.

59. Lei, J.; Wan, J.T.K.; Yu, K.W.; Sun, H. First-principle approach to dielectric behavior of nonspherical cell suspensions. *Phys. Rev. E* **2001**, *64*, 012903.

60. Thomas B. Jones *Electromechanics of particles*; Cambridge University Press in Cambridge: New York, 1995; ISBN 0521431964.

61. Kyoungchul Park; Kabiri, S.; Sonkusale, S. CMOS dielectrophoretic Lab-on-Chip platform for manipulation and monitoring of cells. In Proceedings of the 2015 37th Annual International Conference of the IEEE Engineering in Medicine and Biology Society (EMBC); IEEE: Milan, Italy, 2015; Vol. 2015, pp. 7530–7533.

62. Huan, Z.; Chu, H.K.; Yang, J.; Sun, D. Characterization of a honeycomb-like scaffold with dielectrophoresis-based patterning for tissue engineering. *IEEE Trans. Biomed. Eng.* **2017**, *64*, 755–764.

63. Patel, S.; Showers, D.; Vedantam, P.; Tzeng, T.-R.; Qian, S.; Xuan, X. Microfluidic separation of live and dead yeast cells using reservoir-based dielectrophoresis. *Biomicrofluidics* **2012**, *6*, 034102.

64. Piacentini, N.; Mernier, G.; Tornay, R.; Renaud, P. Separation of platelets from other blood cells in continuous-flow by dielectrophoresis field-flow-fractionation. *Biomicrofluidics* **2011**, *5*, 1–8.

65. Cheng, I.-F.; Chang, H.-C.; Hou, D.; Chang, H.-C. An integrated dielectrophoretic chip for continuous bioparticle filtering, focusing, sorting, trapping, and detecting. *Biomicrofluidics* **2007**, *1*, 021503.

66. Demircan, Y.; Yilmaz, G.; Külah, H. Electrophoresis and Dielectrophoresis for Lab-on-a-Chip (LOC) Analyses. In *Microfluidic Technologies for Human Health*; WORLD SCIENTIFIC, 2013; pp. 341–375.

67. Polevaya, Y.; Ermolina, I.; Schlesinger, M.; Ginzburg, B.-Z.; Feldman, Y. Time domain dielectric spectroscopy study of human cells. *Biochim. Biophys. Acta - Biomembr.* **1999**, *1419*, 257–271.

68. Yao, J.; Zhu, G.; Zhao, T.; Takei, M. Microfluidic device embedding electrodes for dielectrophoretic manipulation of cells-A review. *Electrophoresis* **2019**, *40*, 1166–1177.

69. Zeinali, S.; Cetin, B.; Oliaei, S.N.B.; Karpat, Y. Fabrication of continuous flow microfluidics device with 3D electrode structures for high throughput DEP applications using mechanical machining. *Electrophoresis* **2015**, *36*, 1432–1442.

70. García-Sánchez, P.; Ramos, A.; Green, N.G.; Morgan, H. Experiments on AC electrokinetic pumping of liquids using arrays of microelectrodes. *IEEE Trans.*

Dielectr. Electr. Insul. **2006**, *13*, 670–677.

71. Yildizhan, Y.; Erdem, N.; Islam, M.; Martinez-Duarte, R.; Elitas, M. Dielectrophoretic separation of live and dead monocytes using 3D carbon-electrodes. *Sensors (Switzerland)* **2017**, *17*, 1–13.

72. Yafouz, B.; Kadri, N.; Ibrahim, F. Microarray Dot Electrodes Utilizing Dielectrophoresis for Cell Characterization. *Sensors* **2013**, *13*, 9029–9046.

73. Yafouz, B.; Kadri, N.; Ibrahim, F. Dielectrophoretic Manipulation and Separation of Microparticles Using Microarray Dot Electrodes. *Sensors* **2014**, *14*, 6356–6369.

74. Li, M.; Li, W.H.; Zhang, J.; Alici, G.; Wen, W. A review of microfabrication techniques and dielectrophoretic microdevices for particle manipulation and separation. *J. Phys. D. Appl. Phys.* **2014**, *47*.

75. Becker, F.F.; Wang, X.B.; Huang, Y.; Pethig, R.; Vykoukal, J.; Gascoyne, P.R. Separation of human breast cancer cells from blood by differential dielectric affinity. *Proc. Natl. Acad. Sci.* **1995**, *92*, 860–864.

76. Jang, L.-S.; Huang, P.-H.; Lan, K.-C. Single-cell trapping utilizing negative dielectrophoretic quadrupole and microwell electrodes. *Biosens. Bioelectron.* **2009**, *24*, 3637–3644.

77. Khoshmanesh, K.; Zhang, C.; Tovar-Lopez, F.J.; Nahavandi, S.; Baratchi, S.; Kalantar-zadeh, K.; Mitchell, A. Dielectrophoretic manipulation and separation of microparticles using curved microelectrodes. *Electrophoresis* **2009**, *30*, 3707–3717.

78. Pommer, M.S.; Zhang, Y.; Keerthi, N.; Chen, D.; Thomson, J.A.; Meinhart, C.D.; Soh, H.T. Dielectrophoretic separation of platelets from diluted whole blood in microfluidic channels. *Electrophoresis* **2008**, *29*, 1213–1218.

79. Fatoyinbo, H.O.; Hoettges, K.F.; Hughes, M.P. Rapid-on-chip determination of dielectric properties of biological cells using imaging techniques in a dielectrophoresis dot microsystem. *Electrophoresis* **2008**, *29*, 3–10.

80. Otto, S.; Kaletta, U.; Bier, F.F.; Wenger, C.; Hölzel, R. Dielectrophoretic immobilisation of antibodies on microelectrode arrays. *Lab Chip* **2014**, *14*, 998–1004.

81. Guha, S.; Jamal, F.I.; Schmalz, K.; Wenger, C.; Meliani, C. CMOS lab on a chip device for dielectric characterization of cell suspensions based on a 6 GHz Oscillator. In Proceedings of the Proceedings of the 43rd European Microwave Conference; 2013; pp. 471–474.

82. Buyong, M.; Kayani, A.; Hamzah, A.; Yeop Majlis, B. Dielectrophoresis

Manipulation: Versatile Lateral and Vertical Mechanisms. *Biosensors* **2019**, *9*, 30.

83. Yang, L. A Review of Multifunctions of Dielectrophoresis in Biosensors and Biochips for Bacteria Detection. *Anal. Lett.* **2012**, *45*, 187–201.

84. Yang, L.; Guiseppi-Elie, A. Impedimetric Biosensors for Nano- and Microfluidics. In *Encyclopedia of Microfluidics and Nanofluidics*; Springer New York: New York, NY, 2015; pp. 1364–1380.

85. Yang, L.; Banada, P.P.; Chatni, M.R.; Seop Lim, K.; Bhunia, A.K.; Ladisch, M.; Bashir, R. A multifunctional micro-fluidic system for dielectrophoretic concentration coupled with immuno-capture of low numbers of Listeria monocytogenes. *Lab Chip* **2006**, *6*, 896.

86. Yang, L. Dielectrophoresis assisted immuno-capture and detection of foodborne pathogenic bacteria in biochips. *Talanta* **2009**, *80*, 551–558.

87. Miltenyi, S.; Müller, W.; Weichel, W.; Radbruch, A. High gradient magnetic cell separation with MACS. *Cytometry* **1990**, *11*, 231–238.

88. Gascoyne, P.R.C.; Xiao-Bo Wang; Ying Huang; Becker, F.F. Dielectrophoretic separation of cancer cells from blood. *IEEE Trans. Ind. Appl.* **1997**, *33*, 670–678.

89. Zhu, K.; Kaprelyants, A.S.; Salina, E.G.; Markx, G.H. Separation by dielectrophoresis of dormant and nondormant bacterial cells of Mycobacterium smegmatis. *Biomicrofluidics* **2010**, *4*, 022809.

90. Choi, W.; Kim, J.-S.; Lee, D.-H.; Lee, K.-K.; Koo, D.-B.; Park, J.-K. Dielectrophoretic oocyte selection chip for in vitro fertilization. *Biomed. Microdevices* **2008**, *10*, 337–345.

91. Sabuncu, A.C.; Liu, J.A.; Beebe, S.J.; Beskok, A. Dielectrophoretic separation of mouse melanoma clones. *Biomicrofluidics* **2010**, *4*, 021101.

92. Pethig, R.; Huang, Y.; Wang, X.; Burt, J.P.H. Positive and negative dielectrophoretic collection of colloidal particles using interdigitated castellated microelectrodes. *J. Phys. D. Appl. Phys.* **1992**, *25*, 881–888.

93. Demierre, N.; Braschler, T.; Linderholm, P.; Seger, U.; van Lintel, H.; Renaud, P. Characterization and optimization of liquid electrodes for lateral dielectrophoresis. *Lab Chip* **2007**, *7*, 355–365.

94. Tai, C.-H.; Hsiung, S.-K.; Chen, C.-Y.; Tsai, M.-L.; Lee, G.-B. Automatic microfluidic platform for cell separation and nucleus collection. *Biomed. Microdevices* **2007**, *9*, 533–543.

95. Rajaraman, S.; Noh, H. (Moses); Hesketh, P.J.; Gottfried, D.S. Rapid, low cost microfabrication technologies toward realization of devices for

dielectrophoretic manipulation of particles and nanowires. *Sensors Actuators B Chem.* **2006**, *114*, 392–401.

96. Zhang, C.; Khoshmanesh, K.; Tovar-Lopez, F.J.; Mitchell, A.; Wlodarski, W.; Klantar-zadeh, K. Dielectrophoretic separation of carbon nanotubes and polystyrene microparticles. *Microfluid. Nanofluidics* **2009**, *7*, 633–645.

97. Li, H.; Bashir, R. Dielectrophoretic separation and manipulation of live and heat-treated cells of Listeria on microfabricated devices with interdigitated electrodes. *Sensors Actuators, B Chem.* **2002**, *86*, 215–221.

98. Auerswald, J.; Knapp, H.F. Quantitative assessment of dielectrophoresis as a micro fluidic retention and separation technique for beads and human blood erythrocytes. *Microelectron. Eng.* **2003**, *67–68*, 879–886.

99. Suehiro, J. Fabrication and characterization of nanomaterial-based sensors using dielectrophoresis. *Biomicrofluidics* **2010**, *4*, 022804.

100. Li, Y.; Dalton, C.; Crabtree, H.J.; Nilsson, G.; Kaler, K.V.I.S. Continuous dielectrophoretic cell separation microfluidic device. *Lab Chip* **2007**, *7*, 239–248.

101. Asbury, C.L.; Diercks, A.H.; van den Engh, G. Trapping of DNA by dielectrophoresis. *Electrophoresis* **2002**, *23*, 2658–2666.

102. Gadish, N.; Voldman, J. High-Throughput Positive-Dielectrophoretic Bioparticle Microconcentrator. *Anal. Chem.* **2006**, *78*, 7870–7876.

103. Flanagan, L.A.; Lu, J.; Wang, L.; Marchenko, S.A.; Jeon, N.L.; Lee, A.P.; Monuki, E.S. Unique Dielectric Properties Distinguish Stem Cells and Their Differentiated Progeny. *Stem Cells* **2008**, *26*, 656–665.

104. Park, K.; Kabiri, S.; Sonkusale, S. Dielectrophoretic lab-on-CMOS platform for trapping and manipulation of cells. *Biomed. Microdevices* **2016**, *18*, 1–11.

105. Ning, Y.; Ma, X.; Multari, C.R.; Luo, X.; Gholizadeh, V.; Palego, C.; Cheng, X.; Hwang, J.C.M. Improved broadband electrical detection of individual biological cells. In Proceedings of the 2015 IEEE MTT-S International Microwave Symposium; IEEE, 2015; pp. 1–3.

106. Miled, M.A.; Sawan, M. Dielectrophoresis-Based Integrated Lab-on-Chip for Nano and Micro-Particles Manipulation and Capacitive Detection. *IEEE Trans. Biomed. Circuits Syst.* **2012**, *6*, 120–132.

107. Uddin, A.; Milaninia, K.; Chen, C.-H.; Theogarajan, L. Wafer Scale Integration of CMOS Chips for Biomedical Applications via Self-Aligned Masking. *IEEE Trans. Components, Packag. Manuf. Technol.* **2011**, *1*, 1996–2004.

108. Manaresi, N.; Romani, A.; Medoro, G.; Altomare, L.; Leonardi, A.; Tartagni, M.;

Guerrieri, R. A CMOS Chip for Individual Cell Manipulation and Detection. *IEEE J. Solid-State Circuits* **2003**, *38*, 2297–2305.

109. Ameri, A.; Zhang, L.; Gharia, A.; Anwar, M.; Niknejad, A.M. Dielectrophoretic-Assisted Biosensor for Single-Cell Characterization at Mmwave Frequencies in CMOS 28nm Technology. In Proceedings of the 2019 20th International Conference on Solid-State Sensors, Actuators and Microsystems & Eurosensors XXXIII (TRANSDUCERS & EUROSENSORS XXXIII); IEEE, 2019; pp. 174–177.

110. Guha, S.; Schumann, U.; Jamal, F.I.; Wagner, D.; Meliani, C.; Schmidt, B.; Wenger, C.; Wessel, J.; Detert, M. Integrated high-frequency sensors in catheters for minimally invasive plaque characterization. In Proceedings of the 20th European Microelectronics and Packaging Conference and Exhibition: Enabling Technologies for a Better Life and Future, EMPC 2015; 2016; pp. 1–6.

111. Guha. S, Schmalz. K, Meliani. Ch, Wenger. C, K.W. CMOS MEMS based Microfluidic System for Cytometry at 5GHz. In Proceedings of the In Proceedings of the MFHS, Microfluidic handling System; Entschede, The netherlands, 10–12 October 2012.

112. Guha, S.; Wenger, C. Radio Frequency CMOS Chem-bio Viscosity Sensors based on Dielectric Spectroscopy. In Proceedings of the In Proceedings of the 10th International Joint Conference on Biomedical Engineering Systems and Technologies; SCITEPRESS - Science and Technology Publications: Porto, Portugal; pp. 142–148.

113. Guha, S.; Schmalz, K.; Wenger, C.; Herzel, F. Self-calibrating highly sensitive dynamic capacitance sensor: towards rapid sensing and counting of particles in laminar flow systems. *Analyst* **2015**, *140*, 3262–3272.

114. Becker, H. Mind the gap! *Lab Chip* **2010**, *10*, 271–273.

115. Iliescu, C.; Taylor, H.; Avram, M.; Miao, J.; Franssila, S. A practical guide for the fabrication of microfluidic devices using glass and silicon. *Biomicrofluidics* **2012**, *6*, 16505–1650516.

116. Tiggelaar, R.M.; Male, P. van; Berenschot, J.W.; Gardeniers, J.G.E.; Oosterbroek, R.E.; Croon, M.H.J.M. de; Schouten, J.C.; Berg, A. van den; Elwenspoek, M.C. Fabrication of a high-temperature microreactor with integrated heater and sensor patterns on an ultrathin silicon membrane. *Sensors Actuators A Phys.* **2005**, *119*, 196–205.

117. Pipper, J.; Inoue, M.; Ng, L.F.-P.; Neuzil, P.; Zhang, Y.; Novak, L. Catching bird flu in a droplet. *Nat. Med.* **2007**, *13*, 1259–1263.

118. Huang, Y.; Mason, A.J. Lab-on-CMOS integration of microfluidics and electrochemical sensors. *Lab Chip* **2013**, *13*, 3929.

119. Guha, S.; Lisker, M.; Trusch, A.; Wolf, A.; Meliani, C.; Wenger, C. 12 GHz CMOS MEMS Lab-on-chip System for Detection of Concentration of Suspended Particles in Bio-suspensions. In Proceedings of the In Proceedings of the Biodevice; SCITEPRESS - Science and and Technology Publications: Lisbon, Portugal; pp. 49–57.

120. Guha, S.; Warsinke, A.; Tientcheu, C.M.; Schmalz, K.; Meliani, C.; Wenger, C. Label free sensing of creatinine using a 6 GHz CMOS near-field dielectric immunosensor. *Analyst* **2015**, *140*, 3019–3027.

121. Matbaechi Ettehad, H.; Guha, S.; Wenger, C. Simulation of CMOS compatible sensor structures for dielectrophoretic biomolecule immobilization. In Proceedings of the COMSOL- Bioscience and Bioengineering; COMSOL: Rotterdam, The Netherlands, 2017; p. 6.

122. Matbaechi Ettehad, H.; Yadav, R.K.; Guha, S.; Wenger, C. Towards CMOS Integrated Microfluidics Using Dielectrophoretic Immobilization. *Biosensors* **2019**, *9*, 77.

123. Wenger, C.; Lisker, M.; Wolf, A.; Meliani, C.; Guha, S.; Trusch, A. 12 GHz CMOS MEMS Lab-on-chip System for Detection of Concentration of Suspended Particles in Bio-suspensions. **2015**, 49–57.

124. Kurgan, E.; Gas, P. An influence of electrode geometry on particle forces in AC dielectrophoresis. *Prz. Elektrotechniczny* **2010**, *86*, 103–105.

125. Matbaechi Ettehad, H.; Wenger, C. Characterization and Separation of Live and Dead Yeast Cells Using CMOS-Based DEP Microfluidics. *Micromachines* **2021**, *12*, 270.

126. Inac, M.; Wietstruck, M.; Goritz, A.; Cetindogan, B.; Baristiran-Kaynak, C.; Marschmeyer, S.; Fraschke, M.; Voss, T.; Mai, A.; Palego, C.; et al. BiCMOS Integrated Microfluidic Packaging by Wafer Bonding for Lab-on-Chip Applications. In Proceedings of the Proceedings - Electronic Components and Technology Conference; IEEE, 2017; pp. 786–791.

127. Inac, M.; Wietstruck, M.; Goritz, A.; Cetindogan, B.; Baristiran-Kaynak, C.; Lisker, M.; Kruger, A.; Saarow, U.; Heinrich, P.; Voss, T.; et al. The Effect of Surface Optimization on Post-grinding Yield of 200 mm Wafer Level Packaging Applications. In Proceedings of the 2018 7th Electronic System-Integration Technology Conference (ESTC); IEEE: Dresden, Germany; pp. 1–4.

128. Talary, M.S.; Burt, J.P.H.; Tame, J.A.; Pethig, R. Electromanipulation and separation of cells using travelling electric fields. *J. Phys. D. Appl. Phys.* **1996**, *29*, 2198–2203.

129. Piper, P.W. The heat shock and ethanol stress responses of yeast exhibit extensive similarity and functional overlap. *FEMS Microbiol. Lett.* **1995**, *134*, 121–

127.

130. Hallsworth, J.E. Ethanol-induced water stress in yeast. *J. Ferment. Bioeng.* **1998**, *85*, 125–137.

131. Munoz, A.J.; Wanichthanarak, K.; Meza, E.; Petranovic, D. Systems biology of yeast cell death. *FEMS Yeast Res.* **2012**, *12*, 249–265.

132. Cottet, J.; Fabregue, O.; Berger, C.; Buret, F.; Renaud, P.; Frénéa-Robin, M. MyDEP: A New Computational Tool for Dielectric Modeling of Particles and Cells. *Biophys. J.* **2019**, *116*, 12–18.

133. Huang, Y.; Holzel, R.; Pethig, R.; Wang, X. Differences in the AC electrodynamics of viable and non-viable yeast cells determined through combined dielectrophoresis and electrorotation studies. *Phys. Med. Biol.* **1992**, *37*, 1499–1517.

134. Haapalainen, M. Dielectrophoretic mobility of a spherical particle in 2D hyperbolic quadrupole electrode geometry, 2013.

135. Schwan, H.P. Electrical Properties of Tissue and Cell Suspensions. In *Advances in biological and medical physics*; Elsevier, 1957; Vol. 5, pp. 147–209.

7 List of Figures

8 List of Tables